# ANALYSIS OF INTERFEROMETRIC SAR FOR TOPOGRAPHIC MAPPING

MAJID MIRBAGHERI

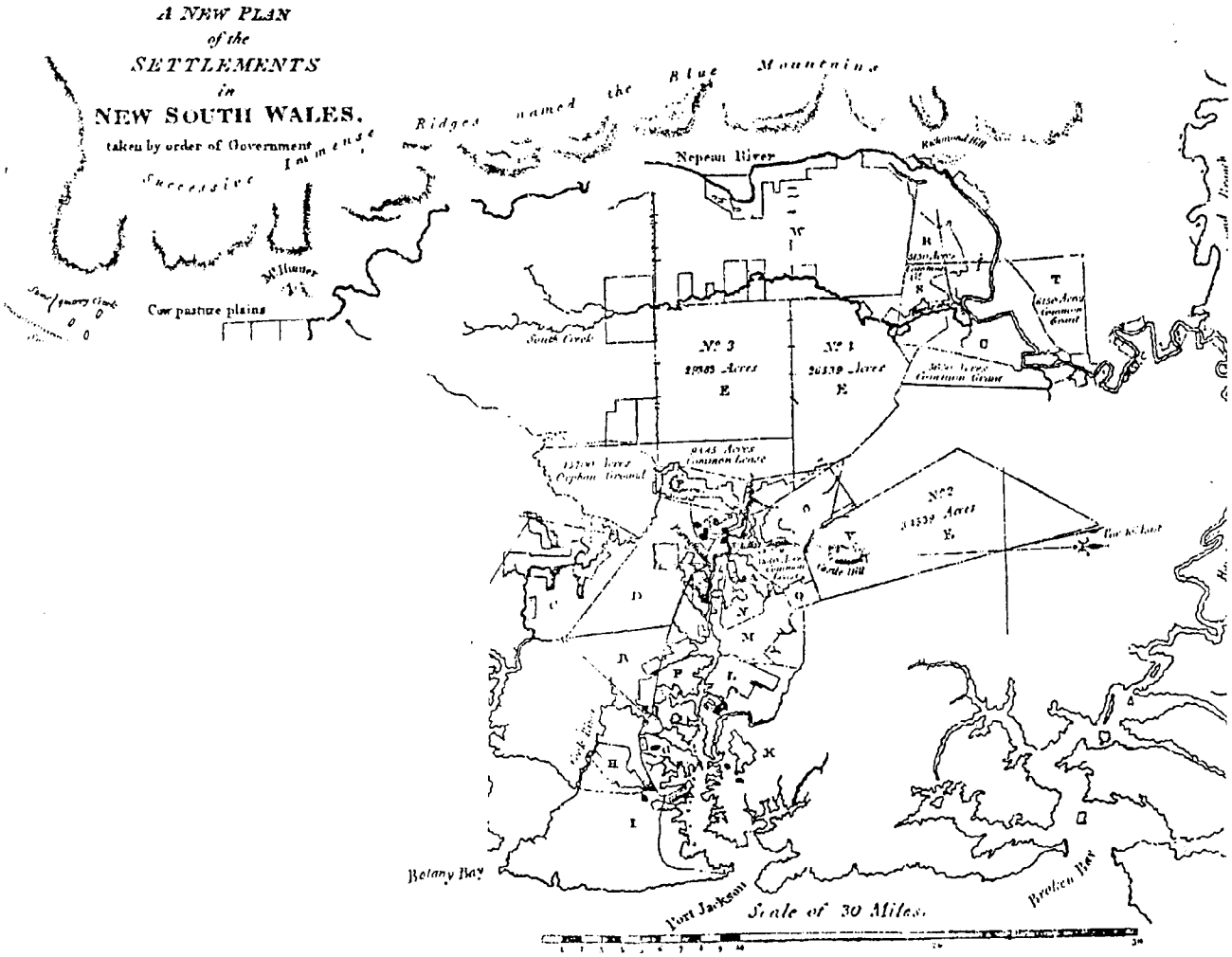


UNISURV S-66, 2001

Reports from

SCHOOL OF SURVEYING
AND SPATIAL INFORMATION SYSTEMS

THE UNIVERSITY OF NEW SOUTH WALES UNSW SYDNEY NSW 2052 AUSTRALIA

UNISURV REPORT S-66, 2001

# ANALYSIS OF INTERFEROMETRIC SAR FOR TOPOGRAPHIC MAPPING

**MAJID MIRBAGHERI**

Received: September 2001
Accepted: October 2001

SCHOOL OF SURVEYING AND SPATIAL INFORMATION SYSTEMS
(formerly GEOMATIC ENGINEERING)
UNIVERSITY OF NEW SOUTH WALES
UNSW SYDNEY NSW 2052
AUSTRALIA

UNISURV REPORTS

Series Editor: Dr. J. M. Rüeger



National Library of Australia

Card No. and ISBN 0 - 7334 - 1856 - 2

# *FOREWORD*

The School of Geomatic Engineering and the Centre for Remote Sensing and GIS at UNSW have undertaken research on synthetic aperture radar (SAR) data since the early 1980s. Recently a research capability has been developed in interferometric SAR (InSAR) for determining elevations. This research has been supported by an ARC Small Grant in 1999 and in 2000-2001 a Strategic Partnerships with Industry – Research and Training (SPIRT) grant was obtained to study the applications of ERS1/2 Tandem data for improving the national DEM. InSAR uses the difference of phase measurements of the received radar signals at two antennas separated slightly in the cross-track direction, to determine the elevations more accurately than stereo SAR mapping, which uses SAR intensity images. It has significant potentials for determining accurate elevations over continental regions. When used in differential mode, precise differences in elevations (to accuracies of several cms) can be determined by studying the differences in phases between two imaging epochs.

This thesis by Dr Majid Mirbagheri, which was undertaken from 1995-1998, studies the estimation of terrain elevations using InSAR. It describes the principles of InSAR and its application; the stages in the processing to determine height information using InSAR; and the development of a model to calculate absolute terrain elevations incorporating ground control data, based on stereo radargrammetric mapping of overlapping SAR images, incorporating expressions for elevations based on the fringe information in InSAR.

The algorithm has been tested with a pair of ERS-1 and ERS-2 images in tandem mode over Sydney. It shows good performance in determining elevations with accuracies between 5 m and 10 m, compared with contours on an orthophoto map. Moreover, the model simultaneously determined planimetry positions of the points. The errors are highly affected by quality of the phase correlation of the points, since it was observed that there is high correlation between the position and height accuracy and the level of the phase coherency in the radar signals.

Emeritus Professor John C. Trinder
March 2001

# *ACKNOWLEDGMENTS*

I wish to express my best gratitude to my supervisor, Prof. John C. Trinder for his close and kind supervision, and valuable comments during my study in the School of Geomatic Engineering. His support, invaluable suggestions, and advice on the various aspects of the work are gratefully acknowledged.

My gratitude is also expressed to Prof. Bruce Forster, my co-advisor, for offering helpful comments regarding this thesis, Mr Brian Donnelly for his technical help, and all the staff members in the School of Geomatic Engineering for their assistance. In particular, I wish to thank Associate Professor Bill Kearsley, Ms. Helve Frangoulis, Mr Leon Daras and Ms. Maria Ponce for their kind help during this study.

My thanks also go to all the staff members in the Australian Centre for Remote Sensing for providing the required image data, and software facilities. In particular, I wish to thank Mr. Peter Radonie, Mrs Rosalie Booth and Mr. Craig Smith.

My sincere gratitude also to the Ministry of Culture and Higher Education of my country for providing me with a scholarship.

Finally, I wish to express my deep gratitude to my wife and my daughter for their love and support through my life. I am also indebted to my parents who have always encouraged me to study.

# *Abstract*

This thesis studies the estimation of terrain elevations using interferometry synthetic aperture radar (InSAR). The procedure uses the difference of phase measurements of the received radar signals at two antennas separated slightly in the cross-track direction, to determine the elevations more accurately than stereo SAR mapping, which uses SAR intensity images. The SAR phases are more sensitive to terrain elevation variations than SAR intensities. It is also possible to perform the same measurements with only one antenna by deriving two images of the scene on two separate passes (repeat-pass interferometry). An interferometric image (interferogram) is formed by multiplying pixels from the reference image with the complex conjugate magnitudes of pixels from the second registered image.

This thesis reviews the basic principles of SAR imaging. These are followed by a discussion of principles of InSAR and its application. The stages in the processing to determine height information using InSAR are also addressed. The parameters which affect the accuracy of elevations determined by InSAR are then discussed, including the correlation of pixels of corresponding areas on two images, and the effects of different parameters on the correlation. The mathematical expressions needed to calculate the height error budget are presented.

A model is developed to calculate absolute terrain elevations incorporating ground control data. The computation procedure is based on stereo radargrammetric mapping of overlapping SAR images, incorporating expressions for elevations based on the fringe information in InSAR. The model develops a simultaneous least squares adjustment of all the measurements by radargrammetry and interferometric SAR, together with ground control, using condition and observation equations. In this case the basic measurements include range, unwrapped phase, and the ground coordinates of control points. The purpose of the least squares adjustment is to determine the most probable solution for the ground coordinates of points identified in the image.

The algorithm has been tested with a pair of ERS-1 and ERS-2 images in tandem mode over Sydney. The algorithm shows good performance in achieving SAR elevation mapping, as compared with contours on an orthophoto map. Moreover, the model simultaneously, determined planimetry positions of the points. The errors are highly affected by quality of the phase correlation of the points, since it was observed that there is a very high correlation between the position and height accuracy and the level of the phase coherency.

# *Table of Contents*

## *Chapter one*

## *Introduction*



## *Chapter Two*

## *Principles of SAR Imaging, InSAR and Applications*

## *Chapter Three*

## *Height Estimation and Uncertainties Using InSAR*

## *Chapter Four*

## *Terrain Elevations From InSAR Incorporating Ground Data*



## *Chapter Five*

## *Experiments and Results*

# *List of Tables*

# *List of figures*

# *Chapter one*

# Introduction

## 1.1 Topographic mapping

The modelling of the interactions between land, oceans and atmosphere is essential for studying the effects of these elements on global change and other environmental problems. However, a global model needs reliable data sets that represent the land, oceans, and atmosphere. One essential data set for this, is an appropriate description of Earth's topography and surface cover. Topographic maps are major tools for research in Earth sciences with applications in oceanography, geology, geophysics, ecology, soil science, hydrology, botany, and glaciology.

Topographic maps are typically determined from stereo pairs of optical photographs (Slama et al., 1980), in which vertical relief causes the same terrain to appear in slightly different positions for different look angles. This shift in location is interpreted in terms of the height of the terrain. The accuracy of the elevations derived by this techniques is in order of 0.1 m. Although this accuracy is excellent for many research areas, it is not an economic method to map a vast area or for global mapping. There are also, many practical electro-optical remote sensing systems available for space cartography, such as the French SPOT series which enables the production of DEMs with an accuracy of 5 to 10 m, which is reasonable for some applications and Russian photography which its vertical resolution is very poor. Clouds and poor sunlight conditions have however, hindered the efficiency of data collection from these systems, since photographic and electro optical systems require cloud free coverage of the terrain. Because clouds, fog and precipitation have little effect on the effectiveness of microwaves, these systems can derive images in all kinds of weather. Moreover, since an active radar system

provides its own illumination, it is not dependent on light from the sun, hence it can operate at any time of the day or night.

For a real aperture radar satellite system to have a ground resolution of the same order as an electro-optical system, it would need an antenna of the order of kilometres in length. The solution to this problem is called Synthetic Aperture Radar (SAR). In this approach a comparatively small radar antenna is made to function as a very large one, by taking advantage of the antenna's motion. SAR systems such as the European Resources Satellites (ERS-1/ERS-2) or the Canadian Radarsat, provide possible solutions to the deficiencies of sensors operating in the visible wavelengths, caused primarily by weather conditions. The application of SAR images for elevation determination is the topic this thesis.

Stereoscopic SAR derived from two overlapping SAR images, has been used to produce topographic maps as demonstrated by (Leberl et al., 1986a, 1986b), (Dowman 1992), (Dowman et al., 1993) and (Chen et al., 1996). Stereoscopic radar requires two SAR images of the same area obtained from different orbital positions. One major problem with stereoscopic SAR mapping is that the illumination difference between the two images usually reduces the correlation between the images in a stereo pair, hence hindering the identification of corresponding points and reducing the elevation mapping accuracy.

A potential technique, which may avoid this problem is interferometric synthetic aperture radar, so-called InSAR or IfSAR. In this technique the observable terrain shift is of the order of the radar wavelength rather than the resolution cell size. Thus a major problem in both the optical and radar stereo techniques, that of identification of the corresponding areas in the two stereo images, is avoided. Moreover, InSAR uses the phase values of the received radar signal, while stereo SAR mapping uses SAR intensity images. Since the SAR phases are more sensitive to terrain variations than the SAR intensity, InSAR is potentially more accurate than stereo mapping in obtaining elevations.

In InSAR, two receiving antennas, separated slightly in the cross-track direction view the same scene, and altimetry information is inferred from the phase differences between the corresponding pixels in each image. It is also possible to perform the same measurements with only one antenna by deriving two images of the scene on two separate passes (repeat-pass interferometry). An interferometric image (interferogram) is formed by multiplying pixels from the reference image with the complex conjugate magnitudes of pixels from the second registered image. A standard interferometric SAR processing sequence consists of: registration of the complex SAR images, interferogram formation, phase unwrapping and conversion of the phase information to altitudes. This thesis will study the determination of elevations from InSAR.

## 1.2 Research objectives

The main objectives of this thesis include:

- To study parameters of the InSAR technique which impact on height accuracy. These are: physical parameters of the surface being imaged, and instrument parameters; such as look angle of SAR, and the distance between antennas viewing the scene. The quality of the correlation of corresponding pixels on the two images is fundamental to height determination by InSAR. This study will explore the effects of these parameters on the correlation, and investigate how these error sources affect the height accuracy derived by InSAR.

- To develop a general model for determining elevations from InSAR. The model is developed to calculate the absolute elevations and planimetry position of terrain points, based on stereo radargrammetric mapping of overlapping SAR images, expressions for elevation based on the phase information in InSAR, and incorporating ground control data.

- To test the model using ERS –1 and ERS –2 data in a tandem mode. ERS-1 is not ideally suited to the production of interferometric data sets, because of the its length

of repeat cycle, which, in many cases, causes insufficient level of coherence between successive SAR acquisition. The launch of ERS-2, has reduced the time between data acquisition of the passes to only one day, this ensuring adequate correlation between successive SAR images. Hence, a set of ERS data will be used to test of the model.

## 1.3 Overview of the thesis

This thesis includes six chapters. Following the introduction, chapter 2 reviews the basic principles of SAR imaging. These are followed by a discussion of principles of InSAR and its application. The stages in the processing to determine height information using InSAR are also addressed.

Chapter 3 describes the parameters which affect the accuracy of elevations determined by InSAR. It includes a discussion on the correlation of pixels of corresponding areas on two images, and the effects of different parameters on the correlation. This chapter also discusses the mathematical expressions needed to calculate the height error budget.

Chapter 4 develops a model to calculate absolute terrain elevations incorporating ground control data. The computation procedure is based on stereo radargrammetric mapping of overlapping SAR images, incorporating expressions for elevation based on the phase information in InSAR images. The model develops a simultaneous least squares adjustment of all the measurements by radargrammetry and interferometric SAR together with ground control, using of condition and observation equations.

Chapter 5 presents test results of applying the developed model in chapter 4 on ERS-1 and ERS-2 tandem data. It describes the experimental procedure and the results. Chapter 6 addresses the conclusions and some recommendations for the future research in Interferometric Synthetic Aperture Radar.

# *Chapter Two*

# Principles of SAR Imaging, InSAR and Applications

## 2.1 Introduction

The name Radar, which is a contraction of the words ***radio detection and ranging*** reflects the intention of early experiments on a device to detect the presence of a target and measure its range. Although a well-designed modern radar can usually extract more information from the target signal than merely range, the measurement of range is still one of the radar's most important functions. The basic principle of radar, real and synthetic aperture, is based on the properties of antenna arrays, pulsed waves and Doppler frequency (Halliday, 1997). In synthetic aperture radar the Doppler frequency and the time delay information are used to generate a high resolution image of the target being illuminated by the radar.

This chapter discusses a simple form of range equation as well as range and azimuth resolution of real aperture radar. Then, it gives a brief description of the operation of a Synthetic Aperture Radar (SAR) and the method by which the transmitted signal is converted into an image. A review of SAR will only be given, since the theory is well known from previous publications. The basic principles of SAR are outlined and types of SAR processors are briefly addressed. These are followed by a discussion on principles of Interferometric Synthetic Aperture Radar (InSAR) and applications. The stages in the processing to determine height information using InSAR are also explained.

## 2.2 The Radar range equation

The radar equation introduces the relationships between the range measured by the antenna to the characteristics of the transmitter, receiver, antenna, target, and environment. The radar equation serves both as a means of understanding radar operations and a basis for radar design. Here, the simple form of the radar equation is derived. Consider a so-called isotropic radiator, (one which radiates uniformly in all directions), of available power $P_t$ watts. The power density (watts per unit area) produced at a distance R from the radar is given by the available transmitter power spread over the surface area of an imaging sphere at that range (Skolnik, 1981).

$$P = \frac{P_t}{4\pi R^2} \quad wm^{-2} \tag{2.1}$$

Radars are not isotropic but instead employ directive antennas to channel the radiated power $P_t$ into some particular direction. Antenna gain G is a measure of how effectively the transmitting antenna can channel more energy in the direction R than in other directions. Thus the power density from a directive antenna with a transmitting gain G at a distance R in that direction is

$$P_G = \frac{P_t G}{4\pi R^2} \tag{2.2}$$

Suppose there is a target at position R, which intercepts a portion of the incident power and radiates it in various directions. The measure of the amount of incident power interpreted by the target and radiated back in the direction of the radar is denoted by the radar cross section $\sigma$ and is defined by the relation;

$$P_\sigma = \frac{P_t G}{4\pi R^2} \frac{\sigma}{4\pi R^2} \tag{2.3}$$

The radar cross section, with units of area (i.e. $m^2$) is a characteristic of the particular target and is a measure of its size as seen by the radar. The actual power received by an antenna placed at the position of the transmitter is the product of the scattered available power density by the effective area ($A_e$) of the receiving antenna.

$$P_r = \frac{P_t G}{4\pi R^2} \frac{\sigma}{4\pi R^2} A_e = \frac{P_t G A_e \sigma}{(4\pi)^2 R^4} \tag{2.4}$$

The distance beyond which the target cannot be detected, the maximum radar range $R_{max}$, occurs when the received echo signal power $P_r$ just equals the minimum detectable signal $S_{min}$. Therefore;

$$R_{max} = \left( \frac{P_t G A_e \sigma}{(4\pi)^2 S_{min}} \right)^{1/4} \tag{2.5}$$

This is the fundamental form of the radar equation (Skolnik, 1981). The important antenna parameters are the transmitting gain and receiving effective area. The aperture of an antenna can be related to its gain according to;

$$G = \frac{4\pi}{\lambda^2} A_e \tag{2.6}$$

And since in radars generally the same antenna is used for both transmitting and reception, the radar equation can be shown as:

$$R_{max} = \left( \frac{P_t G^2 \lambda^2 \sigma}{(4\pi)^3 S_{min}} \right)^{1/4} \quad \text{or} \quad R_{max} = \left( \frac{P_t A_e^2 \sigma}{4\pi \lambda^2 S_{min}} \right)^{1/4} \tag{2.7}$$

These simplified versions of the radar equations do not adequately explain the performance of practical radars. Many important factors that affect range are not implicitly included (Elachi, 1988). In practice, the observed maximum radar ranges are

usually much smaller than those predicted by the above equations. The reasons for the failure of the simple radar equations to correlate with actual performance can be summarised as follows (Skolnik, 1981);

- These equations do not include the various losses that can occur throughout the system or the loss in performance usually experienced when electronic equipment is operated in the field rather than under laboratory conditions.
- The minimum detectable signal $S_{min}$ and target cross section $\sigma$ are both statistical in nature and must be expressed in statistical terms.
- The equations do not consider the meteorological conditions along the propagation path which have an affect on the radar performance.

## 2.3 Resolution of conventional radar

### 2.3.1 Range Resolution

Range resolution of a real aperture radar (RAR) corresponds to the distance between two points on the terrain surface when they can just be resolved. The returns from terrain targets at different ranges will, naturally, arrive at the receiver with different time delays. If the received pulses from two points overlap, they cannot be resolved on the ground. Thus if the pulses of $\tau$ seconds wide are used, then the smallest reasonable distance $\Delta r$ in the slant range direction to the radar is (Elachi, 1988)

$$\Delta r = \frac{c\tau}{2} \qquad (2.8)$$

Where c is the velocity of light.

The direction of propagation of the radar from the antenna is referred to as the slant range direction. However, remote sensing application experts are interested in the specification of the target in the horizontal direction which is referred to as ground range, as shown in figure 2.1. The corresponding ground range resolution is

$$\frac{c\tau}{2\sin\theta} \qquad (2.9)$$

Where $\theta$ is the look angle.

Some major implications can be derived from this equation;

1. The ground resolution is independent of the height of the sensor position, but is defined by the transmitted pulse width $\tau$.
2. The ground range resolution is a function of incidence angle $\theta$. Therefore it changes across the swath position relative to nadir. It is smallest at the far edge and largest at the near edge of the swath.
3. Directly under the platform ($\theta = 0$) there is no resolution. Indeed the near edge of the swath needs to be at least $10^0$ from nadir to give any useable resolution with practical pulse widths.
4. If the antenna radiates to both sides of the platforms, there would be right-left ambiguity since targets either side of the track at equal distances would give the same delay times. Operation is usually restricted therefore to only one side of the platform.

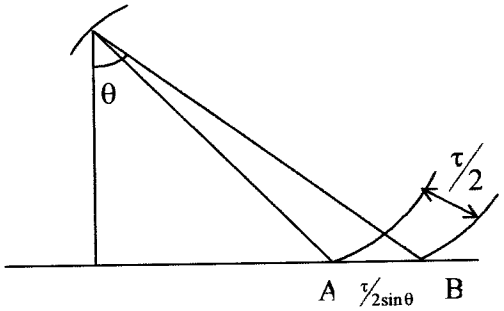


**Figure 2.1: Ground range resolution**

### 2.3.2 Along track resolution

In the along track (so called azimuth) direction, resolution is provided by the shape of the antenna beam, and specifically its footprint on the ground. In fact, the antenna is designed to give a fan shaped beam, which is broader in the range direction to allow a

reasonably wide swath to be obtained, but narrower in the azimuth direction to permit good along track resolution. Since reflections from all targets within the footprint will be received from a single transmitted pulse, it is only necessary to ensure that the next transmitted pulse occurs when the platform has advanced by the equivalent of one azimuth beamwidth of the antenna, in order to obtain contiguous image data. Thus, across track scanning is achieved by measurement of differential time delay, and along track scanning by the movement of the platform.

The angular bandwidth of an antenna in a plane can be expressed as $\beta = \lambda/L$ radians, where $\lambda$ is the operating wavelength and L is the length of the antenna, which implies that the corresponding azimuth resolution is:

$$r_a = \frac{\lambda}{L} R \qquad (2.10)$$

Where, R is the slant range to the target.

To keep $r_a$ small, as R increases, L must be increased and/or $\lambda$ decreased. Either of these options can be impossible to achieve beyond certain limits. Construction of a large antenna is costly as well as difficult, and there are weather limitations for very short wavelength due to atmospheric absorption. For example, for a radar with R=2000 m and $\lambda$=0.1 m, an azimuth resolution of say 30m requires an antenna 6.7 m long, which is large, but could conceivably be mounted on an aircraft. However, consider now the need to move to spacecraft altitudes in order to achieve the consequential benefits of the synoptic view offered; suppose R=200 km-i.e. a very low space Shuttle altitude, then $r_a$ = 30m will require an antenna of length 6.7 km which clearly is impracticable. As a result, the conventional radar image arrangement of Real Aperture Radars (RARs) is unsatisfactory for spaceborne microwave remote sensing. However, the synthetic aperture technique can improve azimuth resolution to the point where $r_a$ is comparable to $r_r$.

## 2.4 Synthetic aperture radar

It was shown in the previous section that to achieve an acceptable azimuth resolution from spacecraft altitudes would require an antenna of impractical dimensions in the along track direction (6.7 km for 30 m from 200 km altitude). Clearly an alternative approach is required.

The method adopted is to synthesize an effectively long antenna by making use of the motion of the space vehicle. As will be appreciated from the sketch in figure 2.3, the azimuth beamwidth of the actual antenna needs to be large in order to create an effective large synthetic aperture of width L. Indeed, the synthetic aperture is defined by the distance of spacecraft travel over which the target remains in the beam of the real antenna.

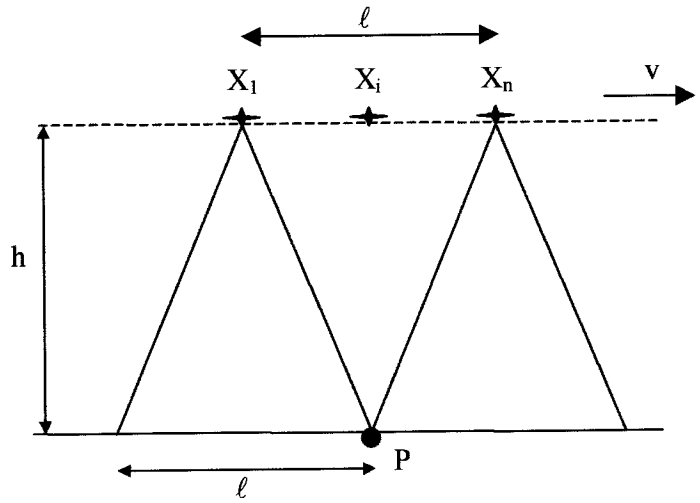


**Figure 2.2: Synthetic Aperture Radar (after Elachi, 1988)**

While this is an attractive concept, and is at present the only viable means for spaceborne radar remote sensing, it does create complexities in forming the image data. As can be appreciated from the figure not only do the received signals contain differential time delays, but also different Doppler shifts because of the motion of the vehicle relative to the target (Elachi, 1988). Indeed, computation of this Doppler shift and its variation with time is one way of describing the operation of a synthetic aperture

radar system and its accompanying signal processing demand. The alternative way to explain the concept of the synthetic aperture radar is a synthetic array approach (Elachi, 1988). The following sections consider these methods.

### 2.4.1 Synthetic array approach

An array of antennas can be considered as a single antenna moving along the array line, as long as the received signals are coherently recorded, and then adding them in the same way as the signals from the antenna array are combined in the waveguide network. Assuming a radar sensor is moving at a velocity v and has an antenna of length L, the length of the antenna main beam footprint on the surface in the azimuth direction is equal to (Elachi, 1988);

$$\ell = \frac{2\lambda h}{L} \tag{2.11}$$

As the sensor moves, successive echoes are recorded at point $X_1$, $X_2$, ..., $X_n$ along the flight line as shown in figure 2.3. The echoes, amplitude and phase are recorded coherently as a function of time. Then, the echoes are combined in a processor to synthesize a linear array. It will be appreciated from figure 2.3, the maximum array length that can be achieved is $\ell$.

The synthesized array will have a beam width of

$$\theta_s = \lambda/\ell = L/2h \tag{2.12}$$

Which gives an azimuth resolution at range R of

$$r_a = h\theta_s = L/2 \tag{2.13}$$

The formula shows that the azimuth resolution is independent both of height and operating $\lambda$. Since the range resolution is also height and $\lambda$ independent, a SAR can operate at any altitude with no variations in its resolution. As a result, spaceborne operation of SAR gives acceptable resolutions. In addition, the azimuth resolution is as high as L/2, which for practical antennas can be around 5m or so. Moreover, in contrast to real aperture radars, the resolution in azimuth improves with smaller antennas. This can be described in the following way:

The further the sensor is from the surface, the larger the footprint is on the surface, hence the larger the synthetic array. This causes a finer synthetic beam, which exactly counterbalances the increase in distance. The smaller the antenna is, the larger the footprint and the synthetic array. This causes a finer synthetic beam, thus a finer resolution.

### 2.4.2 Doppler Synthetic Approach

As the radar sensor flies over a target P, the returns from P first have a positive Doppler shift (when the target enters in the beam), which then decreases to zero, and becomes increasingly negative, while P remains in the beam, as shown in figure 2.3. The frequencies of the return from P cover the spectrum $f_0 \pm f_D$.

Where; $f_0$ is the radar signal frequency and:

$$f_D = \frac{2v}{\lambda}\sin\frac{\theta_a}{2} \approx v\theta_a/\lambda = v/L \qquad (2.14)$$

If a neighbouring target $P'$ is separated from P by a distance $X_a$ along the azimuth dimensions, the Doppler history from $P'$ will be identical to the one from P, but with a time displacement of $t = x_a / v$.

The shortest measurable time displacement after processing the signal with a spectral bandwidth $B_D = 2f_D$ is:

$$t_m = 1/B_D = 1/2f_D = L/2v \qquad (2.15)$$

Therefore the finest possible resolution is

$$X_a = vt_m = L/2 \qquad (2.16)$$

which is similar to that derived using the synthetic array approach.

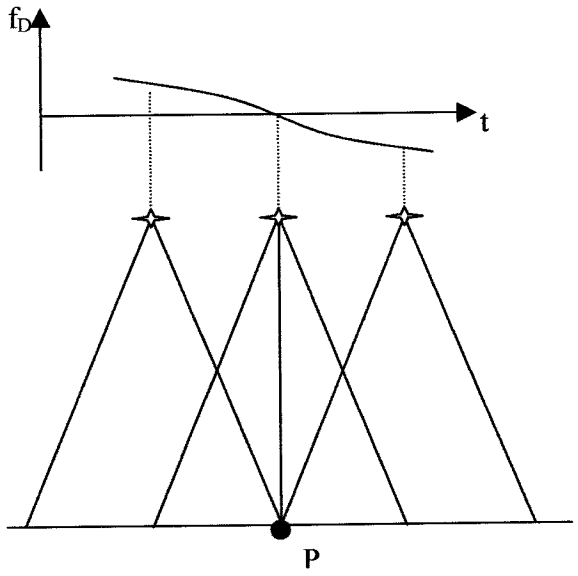


**Figure 2.3: Doppler shift history of the echo from point P as the sensor passes over it (after Elachi, 1988).**

## 2.5 Basic Principles of Radar

The common imaging geometry of radar is illustrated in figure 2.4. The radar antenna usually illuminates a surface strip to one side of the moving platform and perpendicular to its line of motion (nadir track). Radar transmits a short pulse of coherent

electromagnetic radiation towards the surface. Points equidistant from the radar are located on a series of concentric spheres centred at the radar location. They have their echoes received simultaneously. The intersections of the spheres with the plane being imaged give a series of concentric circles, centred at the nadir line, which defines the line of equidistance to the sensor as illustrated in figure 2.5. Points distributed on coaxial cones, with the flight line as the axis and the radar location as the apex, produce identical Doppler shifts. The intersection of these cones with the surface gives a family of hyperbolas. Objects on a certain hyperbola provide equi-Doppler echoes. Hence, each point on the ground can be uniquely identified by its certain time delay and certain Doppler shift. The only potential ambiguity is due to the symmetric equidistant points on the right and the left of the track. However, this is eliminated by illumination of only one side of the track as appreciated from figure 2.4.

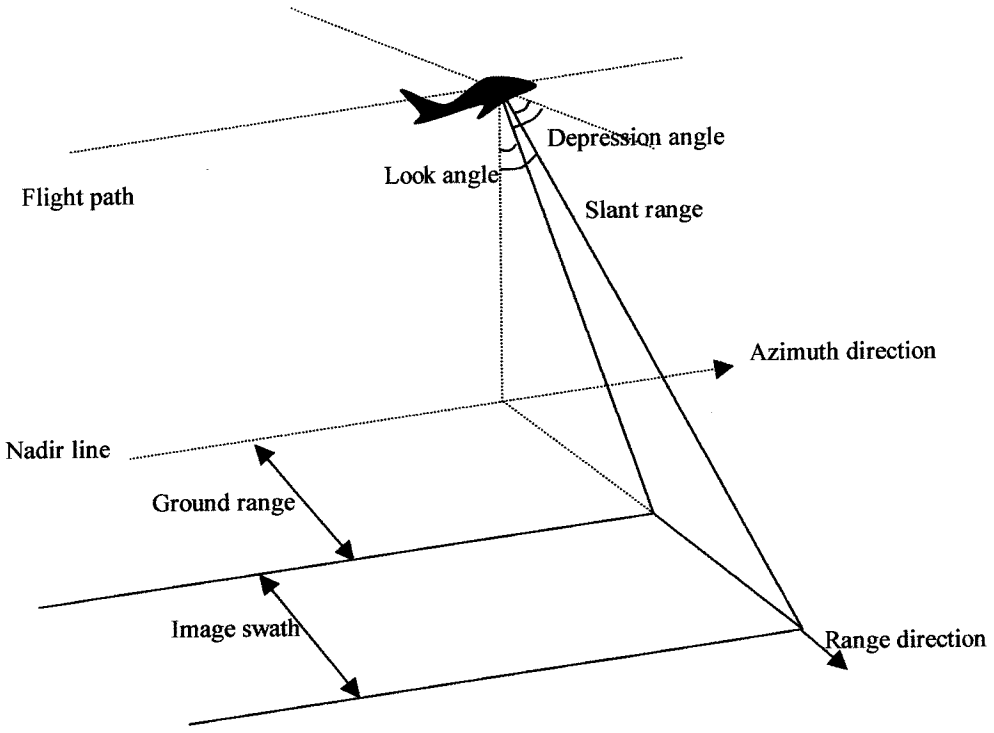


**Figure 2.4: Geometry of Radar (after Avery, 1992)**

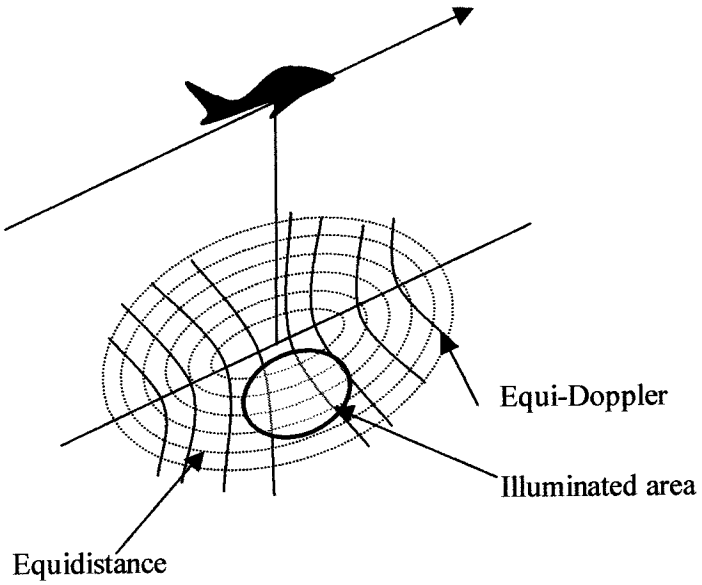


**Figure 2.5: Equi-Doppler echoes (after Elachi, 1988)**

## 2.6 SAR system block diagram

A SAR system consists of five major subsystems as is illustrated in figure 2.6. *The antenna* radiates the electromagnetic energy towards the target to be sensed, and it collects the reflected signals. The antenna dimensions are designed to limit range and Doppler ambiguities to acceptably low levels. The minimum along track length is limited by the requirement to keep azimuth sampling ambiguities to an acceptably low level (section 2.3.2), while the maximum along track length is determined by a desire to illuminate a sufficiently large patch of the terrain. The antenna cross track dimension is determined by the requirement to illuminate a specific swath on surface. This requirement is defined by the nominal look angle from nadir and satellite attitude.

*The Radio Frequency (RF)* electronics consist of the transmitter and receiver elements. The transmitter provides the antenna with a series of high-power coherent pulses of energy at a specific frequency and the receiver detects the returned echoes, amplifies the signal, and converts it into a form which can be handled by the data handling subsystem.

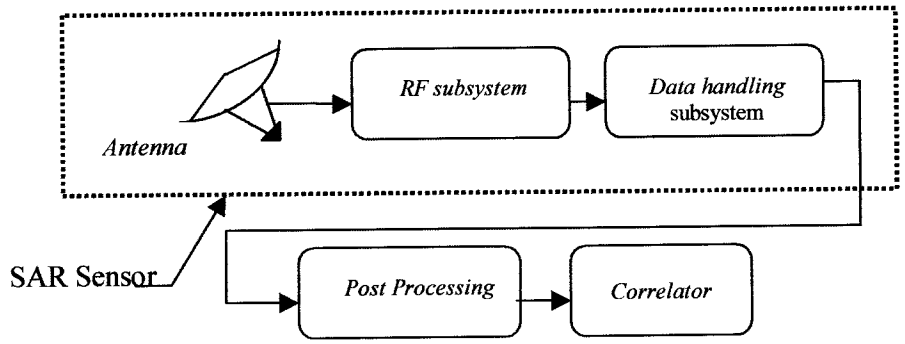


**Figure 2.6: SAR system block diagram**

*The data handling subsystem* reformats the data and also provides the phase and time references necessary for the processing function. The data is either recorded in analogue form on an optical film, or digitized and sent to the high density digital recorder (HDDR) for recording. In a SAR system in which the data are not recorded on board, the ground receiving station receives the signal from the data link subsystem, which transmits the radar echo to the ground for digitization, storage, and subsequent processing. The components of antenna, RF electronics and data handling elements are referred to as the SAR sensor.

*The data correlator element* converts the signal record to an image record, which is a two dimensional representation of the surface echoes.

*The image post correlation processor* processes the output image of the correlator for geometric and radiometric calibration, and for registration with other data sets acquired with similar or different imaging sensors.

## 2.7 Processing of spaceborne SAR data

### 2.7.1 Digital processing of spaceborne SAR data

In the SAR image processing, coherent phase information in an array of radar echoes is used to synthesize an effective antenna aperture, which is much longer than the physical size of the antenna. This enables high-spatial-resolution radar images to be achieved with a practical size antenna. Digital processing of SAR images involves sampling and quantisation of SAR return data. It represents a numerical evaluation of the synthetic aperture beam formation process. A large number of arithmetic computations are involved to accurately represent the radiometric reflectivity of the surface being imaged.

Digital processing of SAR data is an interactive process, which allows the operator to extract information, such as Doppler spectra and pixel phase variations, in intermediate stages of the correlation process. Digital SAR processing presents results that are more accurate and flexible compare with that obtained by optical processing. The mathematical procedure of the correlation algorithm manipulates the sampled return signal to accomplish the SAR correlation process. Design of this procedure consists of two major steps. The first is an accurate modelling of SAR response from a point target, as well as a distributed target scene. This modelling is essential to formulate an inversion process and to provide all the required functions for reconstructing the target scene from the received return signal. The model is also important for evaluating the accomplishment of a SAR system with respect to its attainable limits. The second step involves implementation of the processing functions of the SAR image reconstruction in a clearly efficient mathematical computation procedure. Basics of digital SAR processing have been discussed by Elachi (1988).

### 2.7.2 Optical processing of spaceborne SAR data

Similarity of the phase history produced by a point target to a Fresnel-Zone plate (Halliday, 1997) makes SAR data a natural candidate for optical processing. Developing of optical techniques for processing SAR data dates back to 1960's

(Goodman, 1968, Kozma et al. 1972). A description of optical correlator system and optical processing of SAR data has been given by Fitch (1988). Improvements of digital techniques with the inherent advantages of accuracy and flexibility eliminated the development of optical techniques. Another reason for the lack of further development is that optical technology used in conventional processors has not progressed significantly, and major improvements were not adaptable. Nevertheless, interest in the various applications of the spaceborne SAR has led to an improvement of optical systems in terms of reduction of size, weight, and power consumption for remote sites or onboard processing applications. Moreover, the revolution in acousto-optic and piezoelectric modulators (Kino, 1987), and very large format image collection planes make the possibility of design of the hybrid system (optical and digital) using the benefits of compact power efficient and fast optical computers in future (JPL WWW, 1996).

## 2.8 InSAR

### 2.8.1 Introduction

Interferometric Synthetic Aperture Radar (InSAR) is a technique that uses two or more SAR images over the same area for extracting high resolution digital terrain data. This technique relies on the measurement of the phase of the echo signal rather than the amplitude, as found in conventional imaging radar system. The extreme sensitivity of the technique to altitude changes, high spatial resolution and broad swath coverage makes it an extensive and accurate means to measure geophysical phenomena. The following section discusses the development of InSAR. Basic principles of SAR interferometry are then considered. Finally, some applications of InSAR are briefly outlined.

### 2.8.2 Development of InSAR

Interferometry Synthetic Aperture Radar (InSAR) was first used in observation of the surface of Venus and the Moon (Rogers et al., 1969). InSAR has been successfully

exploited as an effective technique to generate topographic maps (Graham 1974, Prati et al. 1992, Massonet et al. 1993, Madsen et al. 1993, Zebker et al. 1994). Its use as a topographic mapping technique dates back to 1974, when Graham (1974) explained the theory of interferometric radar and used a radar system over Puetro Rico. The system operated at a 3-cm wavelength and employed two 4 by 6 ft antennas separated about 4 ft vertically.

After Graham, no work was published until the Jet Propulsion Laboratory (JPL) began their work in 1985, which was reported by Zebker and Goldstein (1986). They derived a topographic map of a portion of the San Francisco Bay area using two SAR antennas mounted on NASA CV990 aircraft with a baseline of 11.1 m. The signals transmitted from one antenna were received simultaneously by both antennas. The images used were not corrected for the aircraft roll and had a resolution of about 10 m. They obtained 2-10 m rms height deviations over the ocean, but the deviations were larger over some land datum points. They believed that implementation of the method was mainly limited by accuracy of the knowledge of the aircraft attitude.

The technique was then adapted to satellite observation, with the data obtained by a single antenna on a satellite, either in a nearly exact repeating orbit (Prati et al. 1990, Li and Goldstein 1990, Prati et al 1992), or in a nonparallel orbit Gabriel and Goldstein (1988). Although the later method reduces the constraints of parallel orbit in interferometric radar techniques, and allows topographic data to be derived from a larger class of orbits and therefore increases topographic coverage, it is computationally intensive and requires accurate knowledge of the orbital parameters.

Repeat-pass interferometry using airborne SAR was reported by Gray and Farris-Manning (1993). However their results showed the method may never be a viable technique for experimental terrain elevation mapping, because of the difficulty of precise motion compensation and the possibility of coherence loss between passes.

Li and Goldstein (1990) used the InSAR data over Cottonball Basin of Death Valley, California, concentrating on studying the effects of phase measurement errors on the

height uncertainties. They showed some experimentally measured determinations of the spatial decorrelation (sensor geometry effects), based on five orbits of data with a range of different baseline separations. Therefore the interferograms could be used to study the pixel phase measurement accuracy vs. baseline separation. They found that although the height measurement sensitivity increases with baseline separation, the phase error increases with baseline separation as well. There appeared to be an optimal baseline, which balances these two opposing factors. More details are given in next chapter.

Cumming et al. (1990) described the technology of the InSAR and steps taken in making a map using interferometric radar. They explained the sources of errors in the estimation of terrain elevation and showed how these errors are a function of radar beam incident angle and local terrain slope. They used the values of CCRS C- band SAR in simulation, and predicted that errors would vary between 3 m rms at near range to 8 m rms at 5- 8 km ground range.

Differential interferometry, differencing the coherent combination of pairs of satellite repeat-pass images was demonstrated as a very sensitive technique for mapping small elevation changes (Gabriel et al. 1989, Prati et al. 1989). The degree of coherence between the images also has a potential application as a classification tool of different land surfaces (Prati et al. 1992, Askne and Hagberg 1993, Wegmuller and Werner 1995). Wegmueller and Werner (1995) studied the potential of InSAR for forest mapping. Using ERS-1 data over Alaska, France, Germany and Switzerland, they found that forest could be discriminated from other land categories. Moreover, they believed that a number of forest types were distinguishable. They studied the dependence of signatures on the interferometric baseline, the time difference between the data acquisition of the image pairs and seasonal differences. They introduced a method to visualise and interpret the interferometric correlation and the backscatter intensity simultaneously.

Hagberg et al (1995) studied the effects of different types of terrain on the radar measurements using ERS-1 data, to develop a model including both radar system and scene scattering properties to interpret measurements over a forested area. The results

indicated that the scene coherence over forested areas was not sufficient for repeat interferometry. However, they found that in the dense forest, the scattering centre at C-band is close to the top of the trees, although over more sparse groves, it relates to an area average of the tree height. It has also been proposed that using the terrain slope information derived from InSAR, the normalisation of the backscattering coefficient is possible (Wegmuller et al. 1993, Werner et al. 1993).

Zebker and Villasenor (1992) studied the decorrelation of interferometric radar echoes using SEASAT 24 cm -$\lambda$ (L-band) satellite image data for nearly exact repeat orbits over Oregan area, which included forest and unvegetated lava flows. They examined the application of this approach to topographic mapping of vegetated surfaces which may be expected to possess varying backscatter over time. As a result they found that although decorrelation increases with time, digital terrain model generation is feasible. They believed that over unvegetated lava flows and forested area, the height errors due to temporal decorrelation could be limited to 1.5 and 2.6 m, respectively provided there is suitable experiment design. They discussed both temporal and spatial decorrelation, and developed Fourier transform relation between radar impulse response and the baseline, and rotation induced decorrelation functions. They utilized the results in separating the effects of temporally and spatially induced decorrelation.

Zebker et al (1994) analysed ERS-1 data collected over Alaska and southwestern US. However, they indicated that generating maps with relative errors less than 5 m rms is possible in some regions. Because of orbit uncertainties, tie points are required to reduce absolute height errors to a similar magnitude. They found that about 6 tie points per 40 by 40 km scene with at least 5 m rms height accuracy are needed to reduce systematic map height errors of the order of 1 km to below 5 m rms. In investigating the credibility and usefulness of interferometric radar topographic data of the ERS-1 radar system, they found that the temporal decorrelation rates were often much higher than in the SEASAT case. However after the launch of ERS-2 in 1995, the use of ERS-1 and ERS-2 in the tandem mission has provided interferometric data acquired only one day apart.

### 2.8.3 Basic principles of interferometric SAR

In airborne or spaceborne synthetic aperture radar, signals illuminate the terrain and the echoes scattered from the surface are recorded by the antenna. An image of the scene is produced after processing the echoes, in which each picture element (pixel) consists of amplitude and phase information. The conventional SAR image is a display of the amplitude information only. InSAR exploits the phase information as well as amplitude. In this technique two images of the same scene are recorded by two separated antennas. After registrating the two images and resampling one image to overlay the other, the phases corresponding to each pixel are calculated and differenced, resulting in a phase difference image (interferogram). The antennas may be on the same platform (single-pass InSAR) or the same antenna may be flown twice over a scene (repeat-pass InSAR). If the antennas are separated in the direction parallel to the line of flight, in the azimuth direction, motions of surface such as ocean currents can be measured, while if the antennas are separated perpendicular to the line of flight, in the range direction, altitude information can be derived.

The distance between two antennas is referred to as the baseline. Consider two radar antennas $A_1$ and $A_2$, simultaneously viewing the same region with a baseline length B as shown in figure 2.7. The range distance between $A_1$ and an illuminated point on the ground is r, while $r + \delta r$ is the distance between $A_2$ and the same point. In this example, the radar wave is transmitted from antenna $A_1$ and after interaction with the terrain the backscattered return is recorded by both antennas $A_1$ and $A_2$. Then these signals are processed to complex SAR images of the same scene. Phases measured in each image are differenced on a pixel by pixel basis to obtain additional geometrical information about the scene. The phase difference is sensitive to both viewing geometry and the height of the illuminated point P with respect to reference surface.

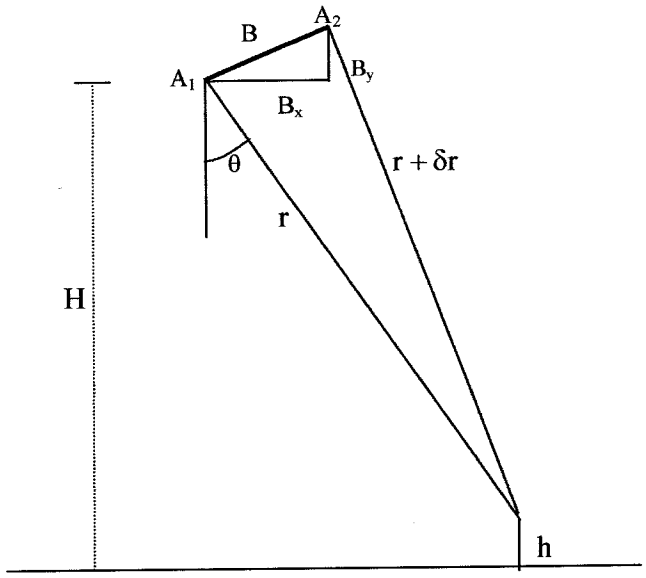


**Figure 2.7: A schematic diagram of InSAR**

From the imaging geometry shown in figure 2.7 the topography h is given by:

$$h = H - r\cos\theta \qquad (2.17)$$

The phase difference between the two returns signals can be modelled as the corresponding distance $\delta r$ in wavelengths, which expressed in radians, is:

$$\varphi = \frac{2\pi\delta r}{\lambda} \qquad (2.18)$$

However, in repeat pass interferometry SAR, since on each pass the antenna acts as both transmitter and receiver, the total path difference for each observation to an illuminated point on the ground is twice what would be expected in a single pass imaging geometry with two physical antennas. Therefore, equations for repeat pass geometry differ from those in single pass case by a factor of two:

$$\varphi = \frac{4\pi\delta r}{\lambda} \qquad (2.19)$$

The path difference $\delta r$ in related to baseline and look angle by:

$$\delta r = B_x \sin\theta - B_y \cos\theta \qquad (2.20)$$

Where, $B_x$ and $B_y$ are components of baseline as shown in figure 2.7.

The phase $\varphi$ in equation 2.18 is the fractional phase (value 0-$2\pi$ radians). This leads to an ambiguity in determining the range, which can be solved by phase unwrapping techniques (section 2.9.3). Hence the phase information can be converted to an image, displaying variations in height, provided the viewing geometry is known to sufficient accuracy. Details of inherent errors in computed elevations are given in Chapter 3.

## 2.9 InSAR processing sequence

A standard interferometric SAR processing sequence consists of:

- Registration of the complex SAR images: as the images are acquired from different viewing points, the images should be resampled so that the images can be projected onto one another.
- Interferogram formation; this is performed by multiplying one image by the complex conjugate of the another image. The interferogram retains both amplitude and phase information, and therefore the file size is larger than the more familiar intensity images. The interferogram demonstrates the variations of phase over the image.
- Phase unwrapping; the elevations of the topography are directly related to the derived phase of the interferogram, which are only measured modulo $2\pi$. Phase unwrapping determines the correct integer number of cycles of the phase of each phase measurement, in order to calculate the elevation at each point in the image. There are a number of phase unwrapping methods as describe below, including:
    - The Goldstein branch cut method (Goldstein, 1988)
    - The fringe method of Lin et al (1992a)

- Knowledge injection (Adragna, 1995)
- Cellular-automata (Ghiglia et al., 1987)

- Conversion of the phase information to desired surface motions or altitudes.

### 2.9.1 Coregistration

Image registration includes the geometrical alignment of the two SAR images of the same scene. Inaccurate alignment of the two images causes loss of coherency between the two interferometric signals, because the interference operation is not carried out on corresponding pixels on the two images. To obtain a high quality interference fringe pattern and in turn a high quality DEM, the images need to be registered to subpixel accuracy (Gabriel et al. 1988, Li et al., 1990, Zebker et al. 1992, Lin et al. 1992b, Just et al. 1994).

In cases where ground control points can be identified on corresponding images, they can be used in a wrapping process to register the images (Leberl et al. 1986a, Leberl et al. 1986b). However, in many cases such as in mountainous terrain, corresponding points are difficult to identify. Another approach to registration has been based on increasing the sensitively of the correlation function to the relative shift between the two images, by using edge enhancement preprocessing (Pratt 1974, Svedlow et al., 1978). However, such algorithms based on correlation do not consider the problem of differences in scales that might be present between the images.

Gabriel et al (1988) adopted a method based on the notion that the quality of the interference fringes between images is highest when the images are correctly aligned. They registered two images by evaluating the SNR of the phase difference image. The SNR was computed by dividing the maximum entry in the spectrum of the phase difference image by the sum of all other entries. First, the complex numbers (samples) associated with 8*8 adjoining pixels were extracted from approximately the same area on each image. Then the numbers associated with an image were conjugated and multiplied by their corresponding number in the other image, resulting in a small product image, which presumably exhibited interference fringes. A two-dimensional

Fast Fourier Transform (FFT) was performed on this product image, yielding a two-dimensional fringe spectrum. The maximum complex absolute value in this spectrum then represented the two spatial frequencies $f_x$ and $f_y$ at which the brightest fringes were seen. The relative quality of these fringes was assessed by computing the signal to noise ratio (SNR) of the spectrum. Gabriel et al (1988) reported that this method worked very well as a rough check on both grid size and the alignment accuracy, with high SNR resulting when the images were close to being aligned, and low SNR when images were far from an acceptable registration. The maximum value of the spectrum was stored as a measure of the quality of that particular registration. Then the whole procedure was repeated using the same pixel values from one image, but with a new 8*8 grid, displaced by one pixel in range or azimuth direction, taken from the second image.

Repeating this, the grid in the second image was scanned over $\pm 4$ pixels in both range and azimuth directions, and a 9*9 matrix of the maximum spectrum values for each displacement was generated. The optimum image offsets lay somewhere between the largest of these values and the offsets represented by the eight nearest neighbours to this value. Gabriel et al. used a two-dimensional quadratic interpolation to find the centre of mass of the 3*3 sub-grid centred on the largest correlation value. They claimed the algorithm yielded a very good registration with one-tenth pixel accuracy. However, because of repetition of computation for many points across the images, the algorithm is computationally intensive.

In a study by Li et al. (1990) images from two satellites passes were registered by computing a statistical correlation function between the two images to determine the range and azimuth pixel offsets. The technique computed the relative correlation coefficient between the two images at various image offsets in range and azimuth. The offset that produce maximum correlation was obtained by fitting the correlation coefficients over the discrete pixel offsets. For image pairs with large baseline separation, the range pixel offset was found to vary as a function of range. These variations are due to the continuous increase in the difference of the slant range for the two orbits as the range to the resolution elements increased.

Lin et al. (1992b) proposed another approach which interpolates the second image on a subpixel basis, evaluates the average fluctuation of the phase difference image, then adjusts the registration parameters according to the change in average fluctuation function, and interpolates the second image again. The process is repeated until the average fluctuation function reaches its minimum, which results in a clear interference fringe pattern.

Fornaro et al. (1995) presented a procedure that implemented the registration step directly at the SAR raw data processing stage. The technique used a common reference output system to process both images. The relevant system transfer functions are analytically evaluated for the two sets of raw image data, determining shift and scaling terms in both range and azimuth directions. These terms are compensated by means of shifting and scaling procedures at raw data level directly, based on the mathematical link between shift and linear stretch of the two image spectra.

### 2.9.2 Interferogram

Once two images are registered with an algorithm such as described in section 2.9.1, the interferogram is formed by taking the product of the first image and the complex conjugate of the second image. To reduce the speckle effect, the interferogram can be averaged by summing over several pixels. When a flat region with no elevation variation is imaged, the phase difference is constant in azimuth direction, and increases linearly in the range direction. When the phase difference reaches $2\pi$, it returns to zero, and the count of the phase difference recommences. Thus, the interference pattern consists of horizontal fringes in the azimuth direction. When the elevation on the terrain varies, the phase differences will deviate from these ideal values, and hence the fringe lines will no longer be straight.

### 2.9.3 Phase unwrapping

One of the major issues in the derivation of elevations using the InSAR technique is phase unwrapping. The problem is that if the slant ranges of two different terrain targets

multiply by two differ by an integer number of radar wavelengths, they will appear with the same phase on the interferogram. Thus, they will be apparently at the same level. Therefore, it is necessary to find the ambiguous number of $2\pi$ wavelengths in the recorded phases of the two targets. Resolving the $2\pi$ ambiguities associated with the phase signals is called phase unwrapping. There are four main phase unwrapping techniques: branch cutting, fringe detection, cellular- automata, and knowledge injection. The first two techniques are explained in more detail below. The Cellular-automata method (Ghiglia et al., 1987) is based on simple discrete mathematical systems, Cellular-automata. It could provide consistent unwrapped phase. However it is highly computational and it also requires a priori knowledge when phase discontinuities exist. Knowledge injection techniques use a rough DEM to reduce the density of fringes. Details of the technique were described by Adragna (1995).

#### *2.9.1.1 Branch cuts*

This method was developed by Goldstein et al. (1988). They discussed two possible types of errors in the unwrapped sequence. The phase estimation integrates phase differences from point to point, always adding the integer number of cycles that minimize the phase differences. The errors are local and global. In local errors, only a few points are corrupted by noise, however, the local errors may be propagated down the entire sequence resulting in global errors.

Assuming that the original scene is sampled often enough so that the true phase does not change by more than one-half cycle per sample point, Goldstein et al. showed a consistent phase unwrapping. Two different results were found when they applied two different rules for scanning a sample; the first scanning was across each sequence and then down to align the sequences; the second scanned down the sequence and then across. This inconsistency is an inherent property of the data and no change in the order of scanning or in the criteria of counting the integer cycles can eliminate it.

For solving the problem, they evaluated the sum of the phase differences clockwise around each set of four adjacent points. It was either zero, plus one cycle, or minus one

cycle. These net resultant cycles are referred as "residues" associated with the four points. It can be shown that any integration path that encloses a single residue, produces an inconsistency in the unwrapped phase and that the net phase difference integral around that path is nonzero. However, if a path encloses an equal number of plus and minus residues, no inconsistency results and the phases can be unwrapped in a consistent manner. This can be performed if the residues are identified, and suitable "branch cuts" are made between the residues to prevent any integration path from crossing these cuts. Residues are local errors in the measured phase caused by noise and or by actual discontinuities i.e. layover in the data. There are three major sources of noise in phase measurements of an interferogram; thermal noise, speckle, and antenna effect, which can be described by one dimensionless correlation coefficient (section 2.10.4).

#### *2.9.1.2 Fringe line detection*

Fringe line detection is another approach to unwrapping phase, developed by Lin et al (1992a). The method includes two steps. The first step uses edge detection techniques to find the location of the fringe lines in the phase difference image. The second step adds a multiple of $2\pi$ each time an integration path crosses a fringe line.

The edge detection techniques mostly include two stages of enhancement of edges by filtering and applying thresholding to the image. Fringe line detection differs from conventional edge detection in the following sense (Lin et al., 1992a):

- Each of the fringe lines is connected, and the end points can only be on the boundaries of the image.
- Only the change in the pixel value, or edge that is lying on a fringe line is desirable to be detected.
- The image has a low SNR.

The fringe line detection algorithm uses a process of edge segment linking, which includes four stages;

- The speckle noise is reduced by applying a median filter, which preserves edges while effectively reducing noise (Gallagher et al., 1974). The choice of size of filter depends on the density of the fringe lines; when the fringe density is larger, the window size needs to be reduced.
- To enhance the phase transition region, five edge masks with different orientation are applied.
- Edge segments are obtained by locating the local maximum points in the enhanced image.
- The edges are linked into fringe lines.

Lin et al used two levels of edge images: the lower level edge image is obtained when no median filter is applied on the phase difference image, and therefore contains more details; upper level edge images are obtained when a median filter is applied, before the edge enhancement process carried out. The upper level image is more reliable and many undesired edge segments have been eliminated.

Starting from a point on a given initial fringe line, the edge points on that fringe line are connected. The sequence of neighbourhood points is searched to locate the next link point on a fringe line. Layers of points around the centre pixel define a neighbourhood and the term of nth neighbourhood is referred to the points of n innermost layers. The search for the next link point starts with the upper level image, because the edge points there are more likely to be on the fringe line. The next link point is searched in the tenth neighbourhood, if it is found, the fringe line is extended to that point by linear interpolation, otherwise, a search is performed on the lower level image in the third neighbourhood. If again the next link is not found, the algorithm goes back to the upper level edge image and searches from the current pixels to find three possible links. Therefore, the fringe line splits into three, each following one link. A good fringe line will have large average pixel grey values, in the edge image, i.e. it passes only a few non-edge points.

The phase is then unwrapped by adding a multiple of $2\pi$ to each pixel, the multiple depends on how many fringe lines lie between the pixel and a reference pixel. The method is considered good when SNR is high in all wrapped phase images and the fringes are greatly separated. However, in areas with low SNR, where the fringe detection is very difficult, error propagation is unavoidable (Hartl et al., 1993a).

## 2.10 SAR Interferometry: Techniques and Applications

### 2.10.1 Digital Elevation Models (DEMs) and topographic mapping

As mentioned before, InSAR has been successfully exploited as an effective technique to generate topographic maps (Graham 1974, Prati et al. 1992, Massonet et al. 1993, Madsen et al. 1993, Zebker et al. 1994). Zebker et al. (1994) discussed the global mapping possibilities using ERS-1 data. They emphasized the need for a short repeat between passes to avoid temporal decorrelation, which causes phase errors over many types of terrain. ERS-1 and ERS-2 tandem mission with a temporal interval of only one day have partially solved the temporal decorrelation problem, although some environmental factors such as wind, rain and snow could still decorrelate radar returns in such short time. Zebker et al. (1994) also suggested a precision orbit determination of the order of 3 cm to obtain accurate absolute heights.

However, they believed that control points could be required to reduce height error to an acceptable level. A spacecraft with a nadir looking laser altimeter was suggested to obtain control points. The evaluation of the DEMs derived from InSAR techniques is not always a simple task, because the DEMs covering the same area as the interferometric data for a large portion of the Earth are not available. One method to evaluate the DEMs is to use contour maps for the comparison (Zebker et al., 1986).

Lin et al. (1994) compared an interferometric SEASAT SAR image with a 7.5 min digital terrain elevation data from the U.S. Geological Survey (USGS) by resampling the USGS digital elevation data, so it had the same orientation as the InSAR image and covered roughly the same area. The root mean square error between the computed

elevations and the USGS digital elevation model was found to be 110m across the whole image. This was 8% of the total terrain variation. After median filtering, it was reduced to 91m, or 6.7% of the total variation. In Chapter 4 a model is developed to calculate absolute terrain elevation incorporating ground control data.

### 2.10.2 Ocean Current measurement

The ability of InSAR to measure ocean surface currents was first demonstrated by Goldstein and Zebker (1987), to a velocity resolution of 4 cm/s with the L- band InSAR on the NASA CV 990 aircraft. For measurement of ocean surface currents, the antennas were separated parallel to the line of flight in azimuth direction. If the target being imaged is stationary the images recorded by the two antennas will be identical, except for a displacement along-track. However, surface currents introduce a phase shift ( $\Delta\varphi$ ) between corresponding pixels on the two images. This phase difference is proportion to the change in the size of the resolution element (d), that is, the time taken for the rear antenna to move to the equivalent position of the front antenna (Goldstein and Zebker 1987, Goldstein et al. 1989):

$$\Delta\varphi = \frac{2\pi d}{\lambda} \tag{2.21}$$

The time taken for the platform to move a distance B at velocity of v is:

$$t = \frac{B}{v} \tag{2.22}$$

At the same time the ocean currents with a radial velocity V moves a distance d (away or towards the antenna):

$$d = Vt = V\frac{B}{v} \tag{2.23}$$

Combination of the above equations results in:

$$\Delta\varphi = \frac{2\pi BV}{\lambda v} \qquad (2.24)$$

If B, v, and $\lambda$ are known and $\Delta\varphi$ is measured then V, the radial ocean currents, can be given by:

$$V = \frac{\Delta\varphi\lambda v}{2\pi B} \qquad (2.25)$$

This represents the velocity of the resolution element on the ocean surface. Therefore ocean surface current velocity image can be derived, from the phase information observed by radar antennas.

### 2.10.3 Differential Interferometry: Change detection

Surface change can be observed by differential radar interferometry. This technique is exploited to determine relative measurements to an accuracy of a few centimetres or even less (Gabriel et al. 1989, Zebker et al. 1994a). Differential radar interferometry is based on a multiple observation interferometry.

The geometry of three observations of a scene is illustrated in figure 2.8. The phase difference of a given resolution element from the first two observations is

$$\Delta\varphi_{12} = \frac{4\pi}{\lambda} a\cos(\theta) \qquad (2.26)$$

And that of the first and third observations is:

$$\Delta\varphi_{13} = \frac{4\pi}{\lambda} b\cos(\theta + \alpha) \qquad (2.27)$$

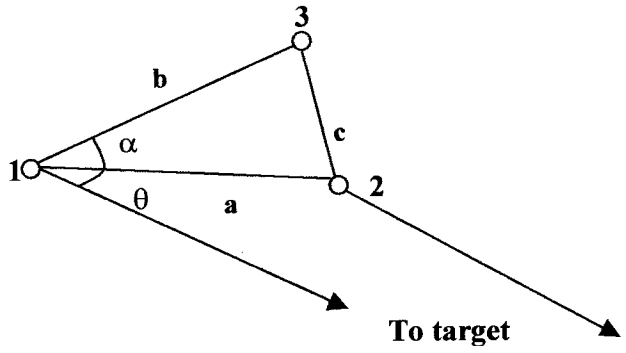


**Figure 2.8: Differential Interferometry, three observations of a scene from three locations separated by baselines a, b, and c.**

Then assuming the parallel ray approximation (Zebker and Goldstein, 1986), the ratio of the two phases is equal to the ratio of the components of the baselines parallel to the look direction:

$$\Delta\varphi_{12} = \frac{4\pi}{\lambda} a_{\parallel} \quad , \quad \Delta\varphi_{13} = \frac{4\pi}{\lambda} b_{\parallel} \tag{2.28}$$

$$\frac{\Delta\varphi_{12}}{\Delta\varphi_{13}} = \frac{a_{\parallel}}{b_{\parallel}} \tag{2.29}$$

Where $a_{\parallel}$, $b_{\parallel}$ are the parallel components of the baselines.

Consider that the ground has changed for the third observation. Hence, for the second interferogram, in addition to the phase shift dependence of topography, there is an additional phase change due to the radar line of sight component of displacement $\Delta r$. Thus:

$$\Delta\varphi_{13} = \frac{4\pi}{\lambda}(b_{\parallel} + \Delta r) \tag{2.30}$$

Removing the effect of topography by subtracting of two interferograms, the solution depends only on $\Delta r$ :

$$\Delta\varphi_{13} - \frac{b_{\parallel}}{a_{\parallel}}\Delta\varphi_{12} = \frac{4\pi}{\lambda}\Delta r \qquad (2.31)$$

The accuracy of this technique depends largely on existing thermal noise and decorrelation of the scene due to baseline separation. Decreasing baseline leads to a higher accuracy of the detected height differences.

### 2.10.4 Classification

The coherence maps acquired from InSAR data have the potential application as a classification tool for different land surfaces (Prati et al. 1992, Askne and Hagberg 1993, Wegmuller and Werner 1995). The degree of coherence (Born and Wolf, 1980) of the two coregistered complex images values $S_1$ and $S_2$ determines the visibility of the interferometric fringes. The coherence is given by

$$\gamma = \frac{< S_1 S_2^* >}{\sqrt{< S_1 S_1^* >< S_2 S_2^* >}} \qquad (2.32)$$

Where < > represents the ensemble averaging over a window in the image.

The interferometric correlation depends on the following parameters (Wegmuller and Werner, 1995):

- Instrument parameters; wavelength, SNR, range resolution, and number of independent looks
- Geometric parameters; baseline and incidence angle.
- Volume scattering and temporal changes; movement of surface, wind effects, growth and loss of foliage, and variation in the dielectric constant (freezing and drying).

Askne and Hagberg (1993) concluded that for long baselines the coherences are consistently lower for forests than for the open fields, and for short baselines the

coherences normally increase. Then in the latter case, coherence is rather sensitive to temporal changes and less sensitive for classification than longer baselines.

Wegmuller and Werner (1995) demonstrated that interferometric correlation allowed the recognition of forested areas as well as distinguishing coniferous, deciduous and mixed forest stands. They also found that orchards, regrowth and clear cut areas showed interferometric correlations higher than closed forest canopies and could therefore be distinguished from those categories.

## 2.11 Summary

One of the most recent techniques using SAR images, is interferometric SAR. InSAR allows the derivation of high resolution digital terrain data by the information contained within two or more SAR images over the same area. Depending on direction of the receiving antennas, different information can be obtained. If the antennas are separated parallel to the line of flight, in the azimuth direction, motions on the surface such as ocean currents can be measured, while if the antennas are separated perpendicular to the line of flight, in the range direction, terrain elevation mapping is possible. The most important of these techniques includes producing DEMs, land classification, terrain change detection, and ocean surface monitoring. In this chapter the basic principles of SAR were outlined and types of SAR processors were briefly addressed. These have been followed by a discussion on principles of Interferometric Synthetic Aperture Radar (InSAR) and applications, as well as, the stages in the processing to determine height information using InSAR.

# *Chapter 3*

# Height Estimation and Uncertainties Using InSAR

## 3.1 Introduction

The theory, design considerations and accuracy of conventional SARs are well known (Elachi, 1988), and they have been briefly discussed in previous chapters. However, an optimum SAR design to measure the radar backscattering cross-section may be far from optimal for an InSAR for measuring topography. The production of digital elevation models by radar interferometric techniques can now be considered as operational. As well a number of new interferometric radar systems are in the planning and implementation stages, while software packages are being marketed by software companies. Therefore, it is essential to understand the accuracy, potential and limitations of this technique. Error analyses of InSAR have been made by Li et al. (1990), Rodriguez et al. (1992) and Zebker et al. (1994).

This chapter presents a discussion of parameters which affect the accuracy of elevations determined by InSAR. As mentioned in previous chapters, the correlation between two coregistered complex images determines the quality of the interferometric fringes. Firstly, the effects of various instrument parameters, volume scattering and temporal changes on the correlation will be discussed, followed by the mathematical expressions needed to calculate the height error budget. These expressions are used to characterize the different error sources, for determining criteria for the selection of optimal InSAR system parameters.

## 3.2 Correlation

Correlation of radar echoes with measurable phase and amplitude received in two images, will be achieved, if each represents almost the same interaction with a scatterer or set of scatterers. Altering the observation geometry, which results in changing the relative positions of the scatterers may lead to signal decorrelation. This is referred as spatial or baseline decorrelation. In addition, actual changes of the target characteristics caused by physical changes in the surface over the time period between observations, in a multi radar imaging experiments may result in temporal decorrelation. Hence, it is important to understand the effects of the physical changes and properties of different surface types and environment conditions, such as surface roughness, surface and volume scattering and wind conditions, on the degree of coherence between images in repeat-pass interferometry. These items will be discussed below. They will be followed by details of spatial decorrelation and decorrelation caused by the rotation of the target with respect to the radar look direction. The latter is only important when interferometric techniques are applied to satellites in crossing orbits (Gabriel and Goldstein, 1988).

### 3.2.1 Temporal decorrelation

Temporal decorrelation is caused by a physical change in the terrain surface between repeat-pass observations. Although temporal decorrelation is an error source in the repeat pass interferometry techniques and is unwanted, it does provide a means to remotely sense a wide variety of surficial processes on time scales of the orbit repeat time and magnitudes of the order of the radar wavelength. This approach may be employed in studying processes, such as;), Change detection (Werner et al. 1992, Massonet et al. 1994), classification (Wegmuller et al., 1995), and geological science (Colteli et al., 1996).

Since this effect is highly dependent on detailed changes of a given surface cover, its quantification requires some assumptions. Assuming that the changes in position of a scatterer are unrelated to its initial position and are characterized by a Gaussian

probability distribution, then spatial decorrelation can be given as follows (Zebker and Villasenor, 1992):

$$\rho_{temporal} = \exp\{-\frac{1}{2}(\frac{4\pi}{\lambda})^2(\sigma_y^2 \sin^2\theta + \sigma_z^2 \cos^2\theta)\} \qquad (3.1)$$

where $\sigma_y$ and $\sigma_z$ are the rms motions in the across and vertical directions, respectively.

Equation 3.1 shows that shorter wavelength data are more sensitive to small surface changes. Thus ERS-1 data (C- band) are more sensitive than SEASAT or JERS-1 (L-band) to distinguish surface cover changes. Zebker et al. (1992) using SEASAT data over Death Valley, CA, and Oregon forested regions over a 20-day time period reported that the correlation decreases with time on the scale of days. The assumption made in these studies was that each scattering centre moves independently of all others. If the scatterers move together in one direction then instead of decorrelation, a systematic phase shift would occur. This fact has been applied to the observation of small surface changes in elevations (Gabriel et al., 1989). The geophysical properties of surfaces, which cause temporal decorrelation will be discussed in the next sections.

#### *3.2.1.1 Surface roughness and wind conditions*

Radar signals have a complex electromagnetic interaction with the target. One of the considerations in studying the radar return is the interrelationship between the roughness of the target's surface, wavelength and look angle. The average vertical dimension of micro-relief of a surface material is a statistical approximation of its roughness. According to the Rayleigh criterion, two major categories of surfaces can be considered; radar smooth and rough surfaces (Ulaby, Moore and Fung, 1982). For example, the backscatter intensity of water in calm weather conditions is very low because the surface is smooth (Fig. 3.1a). For windy conditions, the water surface is rough and the backscatter intensity is higher (Fig. 3.1b). Therefore as water surfaces are sensitive to wind speed and direction, a high temporal decorrelation over water (lakes and rivers) is expected.

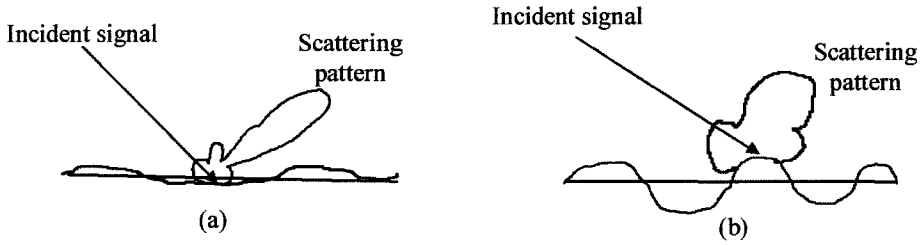


**Figure 3.1: Examples of surface scattering patterns; smooth surface (a), rough surface (b).**

### *3.2.1.2 Surface and volume scattering*

When transmitted electromagnetic radiation of wavelengths in the visible or infrared range is incident on a region of the earth's surface, the energy scattered back to the transmitter is due to the generally diffuse nature of the surface. The "surface" is defined as the actual surface "seen" by the transmitter, including the surfaces of vegetation canopies (Richards et al., 1987). However, for microwave radiation, there is potential for penetration of the surface to allow subsurface (volume) scattering.

When a medium is being imaged by microwave radiation, some reflection of the incident energy will occur from its surface, while some of the incident radiation will be transmitted into the medium. If there is no variation in the properties of the medium (homogeneous medium) the transmitted wave will travel forward, gradually being dissipated. However, if the medium contains dielectric inhomogeneities, such as leaves within a vegetation canopy, besides the possibility of surface scattering, the wavefront of the radiation will be scattered by the inhomogeneities within the volume of the material, that is, volume scattering. Changes in volume scattering over time decreases the coherence of the backscattered radiation. Forest cover will lead to low correlation of interferometric signals because of the effect of volume scattering. Hagberg et al. (1995) measured the coherence over two regions, forest and open fields, with different baselines. They reported a lower coherence over forested areas when compared to that over open fields.

### *3.2.1.3 Soil moisture*

The influence of local soil moisture on the derived DEM has been seen as an unrealistic terrain variation (Hartl et al., 1993b). Depth of penetration of microwave radiation into the surface becomes smaller with increasing level of water in the soil. This phenomena is due to the fact that dielectric constants of typical soils (sand, salt, clay) at different frequencies are much smaller than that of water. The reflected radiation power relative to incident radiation power is described by the reflection coefficient $R = |r|^2$, where r is the Fresnel reflection coefficient of the air-surface interface and for the case of normal incidence radiation is equal to;

$$r_{normal} = \frac{1-\sqrt{\varepsilon_r}}{1+\sqrt{\varepsilon_r}} \qquad (3.2)$$

where $\varepsilon_r$ is the dielectric constant of the surface.

Table 3.1 shows the real part of the dielectric constant of soil and water at different frequencies (Hoekstra and Delaney, 1974).

| Wavelength (cm) | Soil dielectric | Water dielectric |
|---|---|---|
| 60 | ~3.5 | ~79 |
| 7.5 | ~3.2 | ~77 |
| 3 | ~2.3 | ~50 |
| 1.2 | ~2.3 | ~25 |

**Table 3.1: Dielectric constant (real part) of soil and water at different wavelength (Hoekstra and Delaney, 1974)**

Table 3.1 shows a large difference between soil and water dielectric constants. Hence, even a low moisture content in a soil will significantly affect its dielectric constant and therefore its reflective power. The higher the moisture content of the soil, the higher the

level at which the microwave radiation is reflected. Figure 3.2 shows penetration depth of soil ($\delta_\rho$) as a function of volumetric moisture content ($m_v$) (Ulaby et al., 1982). It should be appreciated that if $m_v$ is high, then $\delta_\rho$ is less than 1 cm at a frequency of 10 GHz ($\lambda = 3$ cm) and less than 10 cm at the lowest frequency, 1.3 GHz ($\lambda = 23$ cm). The 4- and 10- GHz ($\lambda = 7.5$- and 3- cm) curves in the figure show that for values of $m_v$ as low as 0.05 gm cm$^{-3}$, $\delta_\rho$ is about 5 cm. Therefore, different amounts of soil moisture over the time period of observations of InSAR will be a source of decorrelation, since the nature of reflection will be different. The figure shows that for a smaller $\lambda$, the effect of the moisture content on the backscattering is less than that for a larger $\lambda$. Therefore, higher temporal correlation is expected for smaller wavelengths.

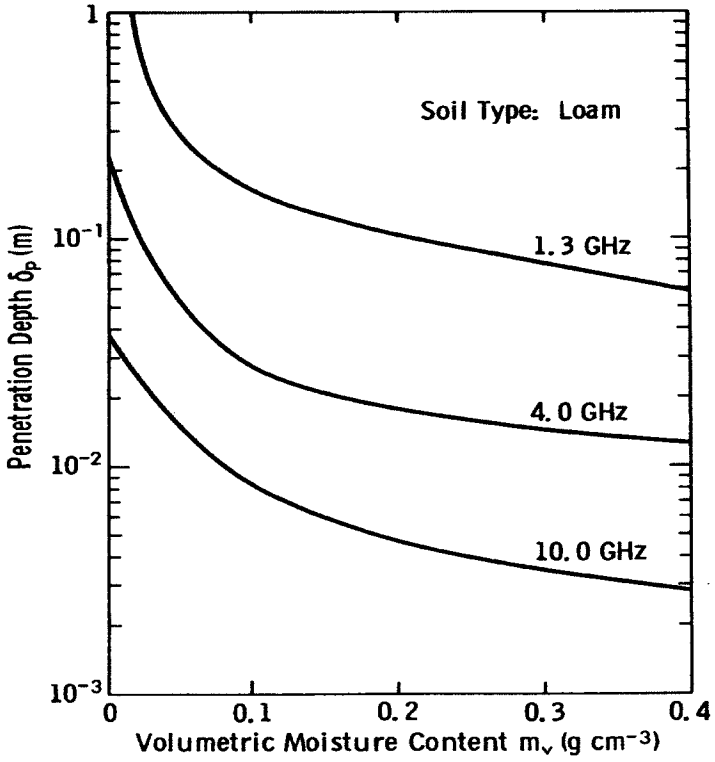


**Figure 3.2: Penetration depth of loamy soil as a function of moisture content (Ulaby et al., Vol. 2, 1982).**

### 3.2.2 Spatial decorrelation

Each resolution element of each scattering surface includes many distributed scattering targets, which reflect with various amplitudes and phases. The total scattered field is then the coherent sum of the individual fields from each scattering centre, the sum of which is a random variable. In the InSAR system even when the pixel derived from each antenna covers the same area, the apparent relative positions of the scatterers change as the two antennas are not in exactly the same position. Therefore different reflections will be measured by the two antennas. This may lead to a loss of coherency between the data derived from the antennas. Thus, there are constraints on the distance between the two antennas (baseline), repeat incidence and aspect angles for acquisition of sufficient correlation.

If the distance between two antennas is too large, it will be impossible to correlate the returns from the two antennas, because of the large disparity between the images received. Thus, although the baseline must be large enough to give sufficient phase sensitivity for height measurement and to increase the height measurement accuracy, it must be small enough to ensure good correlation (Zebker et al. 1986, Goldstein et al. 1988, Li et al. 1990, Zebker et al. 1992). Therefore, there is an optimal baseline for minimum height accuracy for a given system configuration. Zebker et al. (1992) determined the correlation as a function of the baseline as follows:

$$\rho_{spatial} = 1 - \frac{2BR_y \cos^2 \theta}{\lambda r} \qquad (3.3)$$

Where $R_y$, $\lambda$, $\theta$, and r are range resolution, wavelength, look angle, and range, respectively. The critical baseline $B_c$, in which the backscatter from each pixel is completely decorrelated is therefore:

$$B_c = \frac{\lambda r}{2R_y \cos^2 \theta} \qquad (3.4)$$

### 3.2.3 Decorrelation due to rotation

Decorrelation due to rotation of the target with respect to the radar look direction, is a geometric sensor effect. It is important when interferometric techniques are applied for data from satellites with crossing orbits (Gabriel et al., 1988), when the same path on the surface is illuminated from two different aspect angles. As the target is rotated slightly with respect to the sensor, the range and hence phase of each scattering centre changes and their coherent sum will vary. Assuming the scattering centre is rotated $d\varphi$, and $R_x$ is the azimuth resolution, the induced rotation decorrelation can be given as follows (Zebker et al., 1992):

$$\rho_{rotation} = 1 - \frac{2\sin\theta|d\varphi|R_x}{\lambda} \tag{3.5}$$

This equation shows that the larger the wavelength, the smaller the decorrelation due to this effect. Simulated results indicate that the signal is decorrelated with increasing rotation angle, and is nearly completely decorrelated when the rotation reaches about $2.8^0$, at L-band, and after about $0.7^0$, at C-band (Zebker et al., 1992). Parallel orbits do not suffer from this type of decorrelation.

## 3.3 Types of surface cover and correlation

Various types of surface cover show different levels of correlation, since correlation of InSAR signals depends on the interaction of the signals with the surface. To adequately describe the back scattering of radar signals from various surface covers, a surface cover model is needed. There are many vegetation models which describe scattering from vegetation. A three-layer discrete scattering model was developed by Durden et al (1989). The forest floor is modelled as a rough dielectric surface above which are a layer of trunks and a layer of branches. Both trunks and branch layers are modelled by randomly oriented dielectric cylinders. The leaves are modelled as dielectric disks for deciduous forests and dielectric needles for coniferous forests. In Durdan's model there

are seven types of scattering resulting from trees, which are: scattering from leaves, scattering from branches, scattering from trunks, scattering from ground, double bounce scattering from leaves and ground, double bounce scattering from branches and ground, and double bounce scattering from trunks and ground. This model has been further developed to include a tilted ground surface (Van Zyl, 1993), since typical forest floors are not flat and horizontal over a large area.

The radar signal is already propagated through the forest canopy before striking the ground, and thus it is attenuated by amounts proportional to the amount of canopy through which it passes. Van Zyl (1993) found that for P- band the trunk ground interaction term dominates the scattering for HH and VV polarisation. The scattering from the branches always dominates the measured HV polarisation. For L band, the ground/trunk interaction only dominates for HH polarization and only for angles very close to zero for ground surface tilt, whereas for both VV and HV polarisation, the scattering is dominated by returns from the branches.

The ground interaction is more dominant for HH polarisation than for either VV or for HV. This is because the trunk and ground scattering is specular and according to Van Zyl's model is larger for HH polarisation than for VV. Secondly, the attenuation in the canopy is larger for V polarisation than for H polarization. Images acquired at L band HH and C band HH show no evidence of the effect of the topography (Van Zyl, 1993). The dominant scattering of the content of L band is diffuse, caused by direct scattering from the branches. At C band the scattering is from the branches, needles and leaves, and the radiation does not penetrate significantly into the forest. Temporal effects, such as wind conditions may disturb the dominating C band scatterers; that is, the small branches in the top of the trees (Hagberg et al., 1995). Therefore, P- band, HH polarization images for which trunk/ground scattering is dominant, should show more temporal correlation.

Sparsely vegetated fields and grassland, in winter, show high interferometric correlation, except where temporal changes occur due to mechanical cultivation, which causes high

decorrelation. However in summer, nonforest vegetation grows higher and changes faster than in winter. Therefore they should show higher temporal decorrelation in summer (Wegmuller and Werner, 1995).

Over urban and industrial areas intermediate to high correlation has been reported. The correlation decreases with increasing baseline; for example a correlation factor of 0.6 for a baseline of 131m, between 0.45 and 0.5 for a baseline of 507 m, and 0.3 to 0.4 for a baseline of 927 m (Wegmuller and Werner, 1995). They state that, "because of the urban geometry, the individual scatterers contributing to a specific pixel are spread over a relatively large area. The mutual coherence function of such an extended scatterer is narrow, explaining the strong decrease of the interferometric correlation with increasing baseline". That is, the greater the baseline, the less similar is the "view" of the urban areas.

## 3.4 InSAR height error budget

The relationship between the pixel height and the phase difference in an interferogram is given by equations 2.17-20. A simple expression of height uncertainty can be derived by differentiating these equations with respect to each individual parameter (Li et al. 1990, Rodriguez et al. 1992, Zebker et al. 1992). The following section discusses these sources of uncertainties.

### 3.4.1 Range and Satellite Elevation Inaccuracies

Differentiation of equations 2.17-20 with respect to range (r) and satellite elevation ($H_0$) results in the following equations for range and satellite elevation uncertainties (Li et al., 1990):

$$\sigma_{h_r} = \sigma_r \cos\theta \qquad (3.7)$$

$$\sigma_{h_H} = \sigma_H \qquad (3.8)$$

Uncertainty in range (r) is not related to the range resolution of SAR, but it is caused by system clock timing inaccuracies, even though a highly accurate clock may be used in a SAR system; and atmospheric and ionospheric propagation delay which affects the velocity of electromagnetic radiation. Figures 3.3 and 3.4 show the inaccuracy in height estimation due to uncertainty in range ($\sigma_r$). In Figure 3.3, in which it is assumed that uncertainty in range is constant, inaccuracy in height decreases when look angle ($\theta$) increases. The maximum inaccuracy in height estimation is equal to the uncertainty in range ($\sigma_r$), when the look angle approaches zero (but this is not feasible). Figure 3.4 shows the situation when the look angle is a constant $24^0$. It can be observed that in this case there is a linear relation between uncertainty in range ($\sigma_r$) and inaccuracy in height estimation ($\sigma_{h_r}$).

Uncertainty in the distance of the InSAR from the surface results in an absolute height error of the same magnitude as derived from equation 3.3, and illustrated in Figure 3.5.

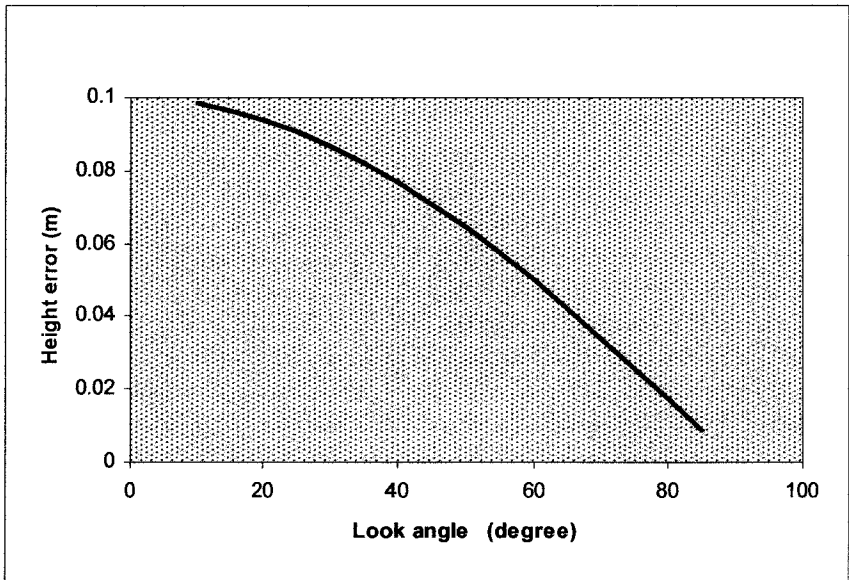


**Figure 3.3: Inaccuracy in height estimation due to uncertainty in range as a function of $\theta$, assuming $\sigma_r$=0.1 m.**

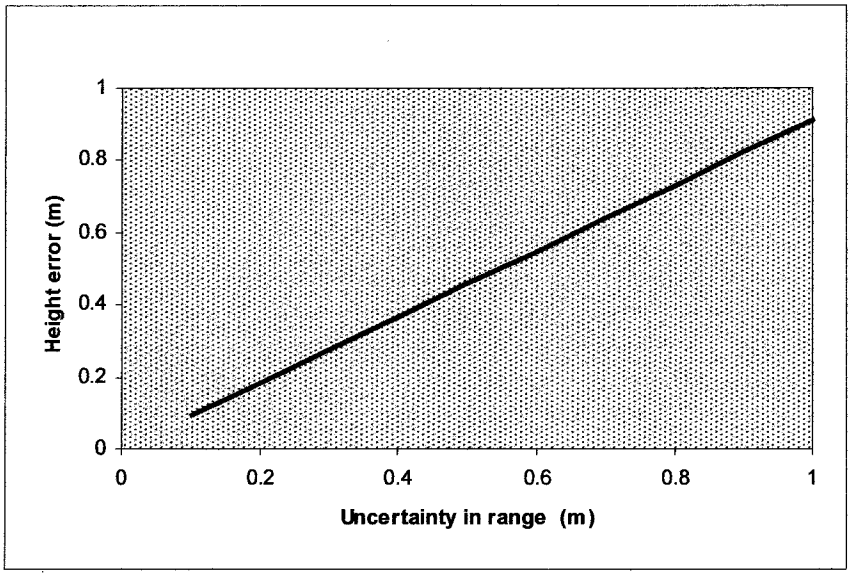


**Figure 3.4: Inaccuracy in height estimation due to uncertainty in range when $\theta = 24^0$**

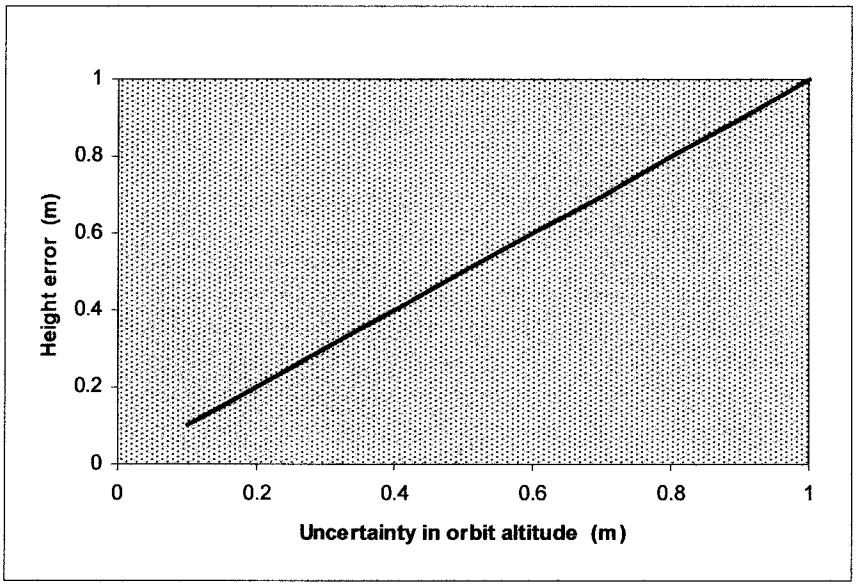


**Figure 3.5: Absolute Inaccuracy in height estimation due to uncertainty in the level of orbit determination.**

This type of error does not depend on any other factors except the uncertainty in the distance of the InSAR from the surface and can be removed by using control points. However, the error is not critical if only relative height measurements are required.

### 3.4.2 Baseline Inaccuracies

Height uncertainties due to inaccuracies in the measurement of system attitude and baseline separation are given by the following equations (Li et al., 1990):

$$\sigma_{h_{Bx}} = \frac{r(\sin\theta)^2}{B_x \cos\theta + B_y \sin\theta}\sigma_{Bx} \tag{3.9}$$

$$\sigma_{h_{By}} = \frac{r \sin\theta \cos\theta}{B_x \cos\theta + B_y \sin\theta}\sigma_{By} \tag{3.10}$$

Figures 3.6-11 show the height errors due to uncertainty in the baseline components. Assuming for simplicity $B_y = 0$, for constant uncertainty in baseline components, height errors due to uncertainty in the baseline component increase as the look angle increases (Figures 3.6-7). However, the error due to uncertainty in the x baseline component ($\sigma_{B_x}$) is greater than that due to uncertainty in the y baseline component $\sigma_{B_y}$, particularly for large $\theta$. Comparing figures 3.6 and 3.7 with figure 3.3, it can be seen that although the height errors due to uncertainty in the baseline component increase when $\theta$ increases, the height error due to uncertainty in range decreases when $\theta$ increases.

However, several other constraints must also be considered. The swath must be as large as large possible to obtain an efficient ground coverage. The look angle must be as large as possible to avoid the effects of layover (Avery, 1992), which causes loss of height information in these regions. The look angle must not be so large as to produce unmanageable data rates, significant shadowing or an unacceptable loss in SNR due to angular variation of the target's radar cross-section (Rodriguez et al., 1992).

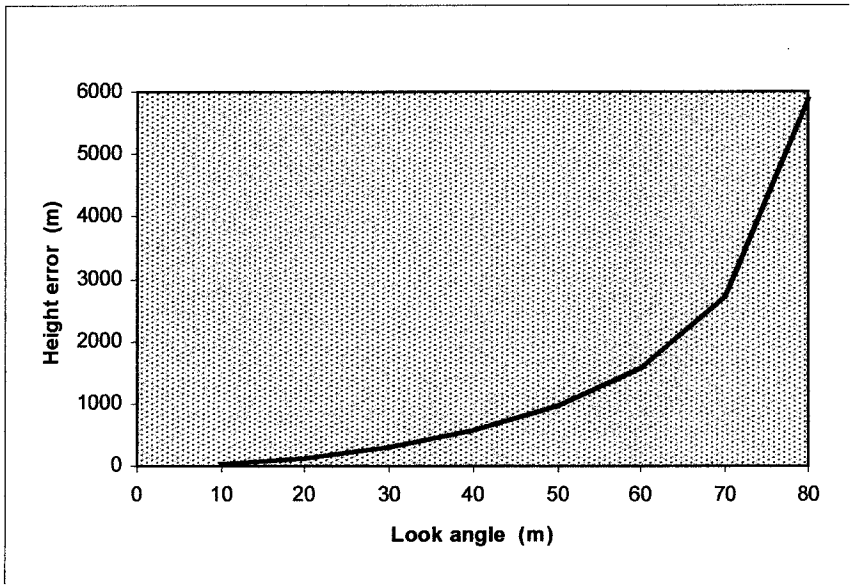


**Figure 3.6: Inaccuracy in height estimation due to uncertainty in $B_x$ as a function of $\theta$ when $B_x$=150 m, $B_y$=0, and $\sigma_{B_x}$ =0.2 m.**

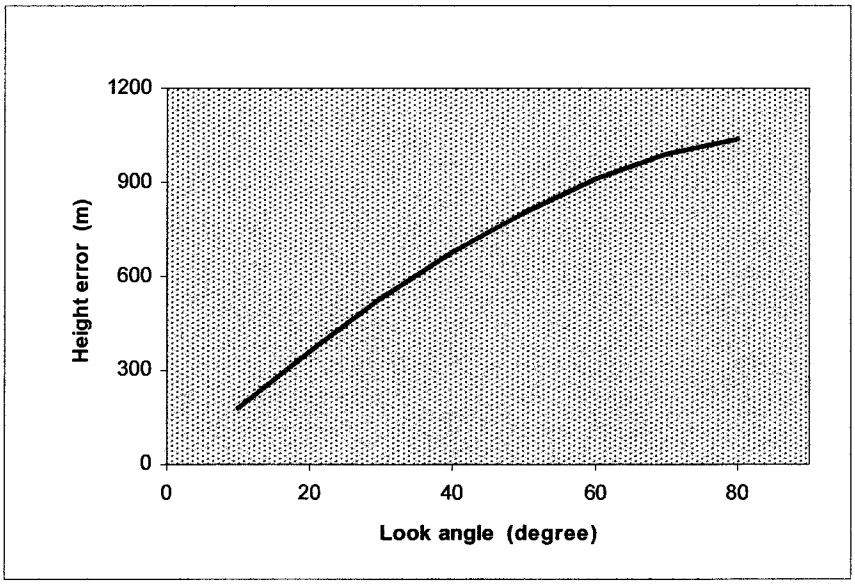


**Figure 3.7: Inaccuracy in height estimation due to uncertainty in $B_y$ as a function of $\theta$, when $B_x$=150 m, $B_y$=0, and $\sigma_{By}$ =0.2 m.**

Figures 3.8-9 show that height error due to uncertainty in the baseline component decreases rapidly when the baseline increases. This trend is very significant for $B_x$ less than 500 m, for the given parameters on the diagram. Then, the decrease continues very slowly, as the baseline increases further. However, as discussed previously (section 3.2.2), if the baseline is too large, it will be impossible to correlate the interferometric signals. Figure 3.10-11 show, for a given look angle and baseline, that the height error increases linearly with increasing uncertainty in the baseline components, and there is a high level of height error (of the order of hundred metres) for an uncertainty of the order of a few centimeters in orbit estimation. This can be reduced by incorporating precise orbit determination techniques (Kimura, 1995) to obtain better estimations of baseline parameters. However, there is a constant systematic error at every point in the image which can be removed using known heights of a few control points in a given image scene (Li et al., 1990). They used the heights of several control points over the Cottonball Basin, to determine the actual baseline and attitude. Zebker et al. (1994) suggested that future spacecraft could be equipped with nadir looking laser altimeters to obtain such tie points.

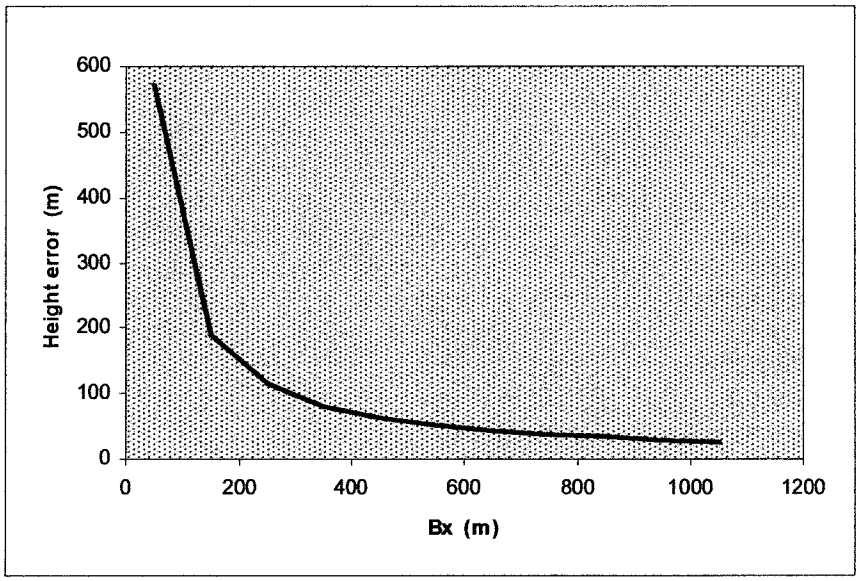


**Figure 3.8: Inaccuracy in height estimation due to uncertainty in $B_x$ as a function of $B_x$, when $\theta$ =0, $B_y$=0, and $\sigma_{Bx}$ =0.2 m.**

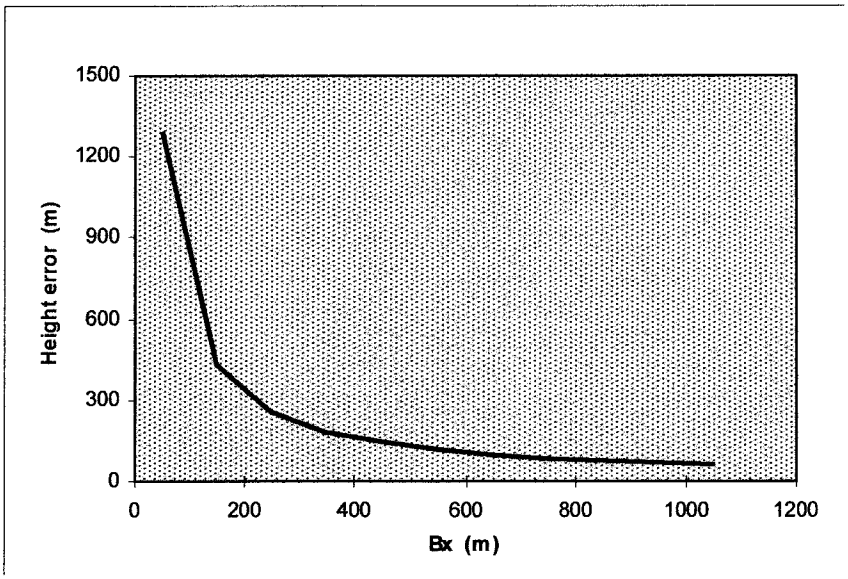


**Figure 3.9: Inaccuracy in height estimation due to uncertainty in $B_y$ as a function of $B_x$, when $\theta = 24^0$, $B_y = 0$, and $\sigma_{By} = 0.2$ m.**

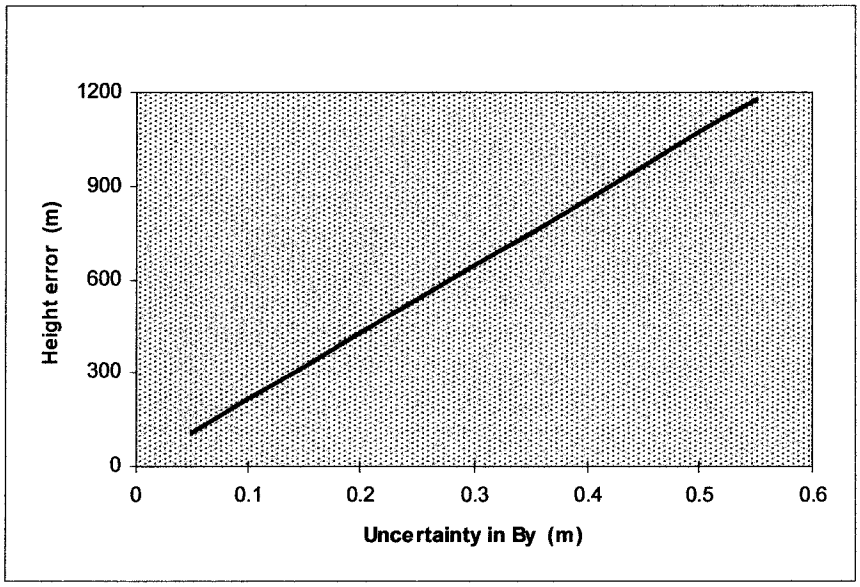


**Figure 3.10: Inaccuracy in height estimation due to uncertainty in $B_y$, when $\theta = 24^0$, $B_x = 150$ m, and $B_y = 0$.**

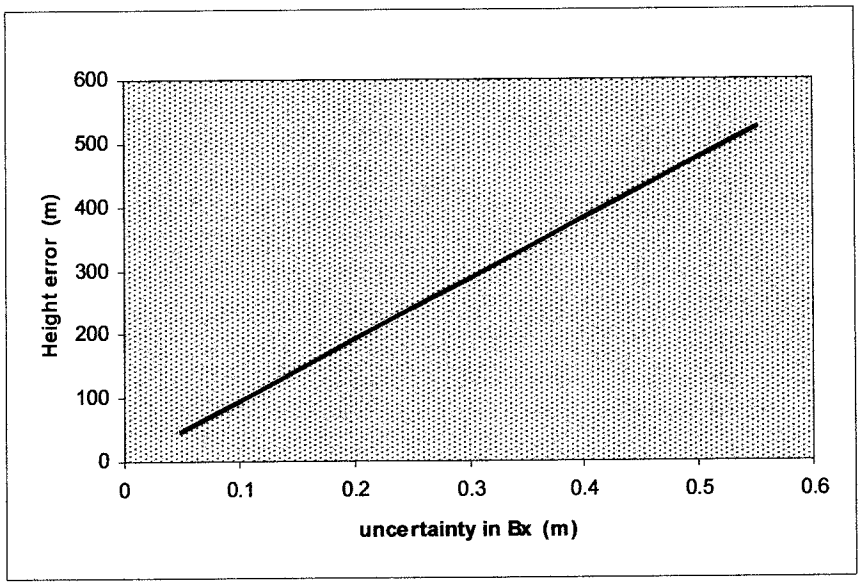


**Figure 3.11: Inaccuracy in height estimation due to uncertainty in $B_x$, when $\theta = 24^0$, $B_x = 150$ m, and $B_y = 0$.**

### 3.4.3 Phase Inaccuracy

The height uncertainty caused by inaccuracy of phase can be obtained by differentiating 2.17- 20 with respect to $\varphi$:

$$\sigma_{h_\varphi} = \frac{r \sin\theta}{2k\pi(B_x \cos\theta + B_y \sin\theta)} \sigma_\varphi \qquad (3.11)$$

There are three major contributors to phase measurement uncertainties; thermal noise, sampling and processing artefacts, and the decorrelation of interferometric radar echoes (Zebker et al., 1994).

### *3.4.1.1 Thermal noise*

Thermal noise, arising from random movements of electrons in the system, corrupts the interference patterns, and causes measurement uncertainty. It can be shown by an equivalent signal-to-noise ratio SNR or correlation ρ (Zebker et al., 1992); that

$$\rho_{thermal} = \frac{1}{1 + SNR^{-1}} \qquad (3.12)$$

### *3.4.1.2 Processing artefacts*

Processing artefacts introduce random errors which reduce the SNR used in the thermal noise correlation coefficient in equation 3.10. However, this type of error is minimised in systems steered to zero Doppler geometry, although some error will still exist (Zebker et al., 1994). Increasing the number of looks, which is the number of resolution elements averaged spatially in an interferogram, reduces the statistical variations (Figure 3.12). However, this technique leads to a loss of resolution.

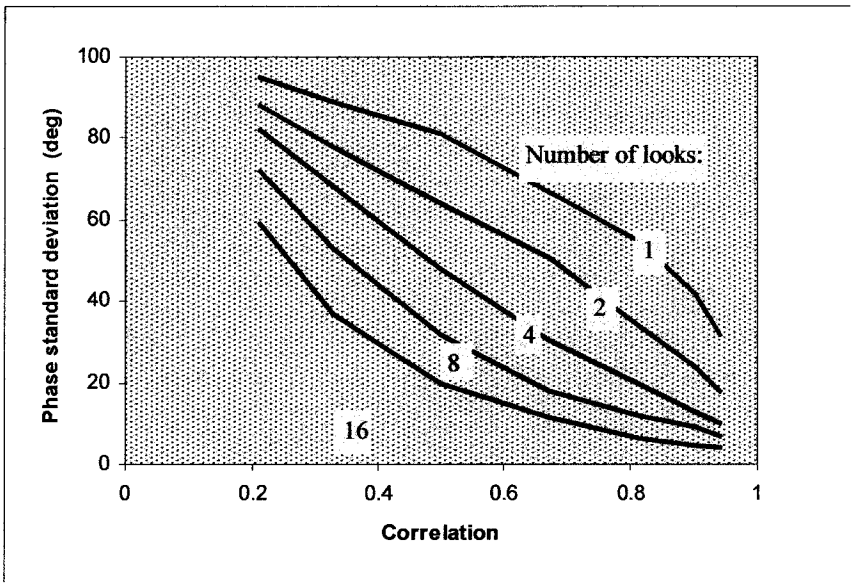


**Figure: 3.12: Phase standard deviation as a function of correlation and number of looks (After Zebker et al., 1994).**

#### *3.4.1.3 Decorrelation*

The correlation of pixels on the two images which correspond to the same area as the terrain are fundamental to DEM determination by InSAR. The most important sources of decorrelation noise for InSAR in general, and for repeat-pass implementation in particular, are temporal and spatial decorrelation, which have been described in sections 3.2.1 and 3.2.2. Temporal decorrelation caused by physical changes of the target surface between repeat-pass observations, whereas Spatial baseline decorrelation is because of sensor geometry effects and caused by viewing the surface with two antennas at slightly different aspect angles.

## 3.5 Summary

The effects of different parameters on interferometric correlation, have been discussed. The decorrelation due to actual changes of the target (temporal decorrelation) was distinguished from instrumental decorrelation. Geophysical properties of surfaces which affect the amount of decorrelation observed in repeat-pass implementation has been explained. Smaller wavelengths are more sensitive to temporal change and cause more decorrelation. There is a constraint on the length of baseline. If it is too large, the interferometric signals decorrelated. However, it must be sufficiently large to give enough phase sensitivity for height measurements.

Types of cover surface and their effects on correlation has also been discussed. Water usually shows low correlation, because it is very sensitive to wind conditions. Interactions of radar signals with vegetation is very complicated. There is volume scattering in the propagation of signals through forest canopy. Over this area, the dominant C-band scatterers; i.e. small branches in the top of the trees, may be affected by temporal affects, such as wind conditions. Therefore over forest areas, C-band interferometry shows low correlation. However for P-band, a HH polarised image may show more correlation due to dominant trunk/ground scattering which is less sensitive to temporal conditions.

Sparse vegetated fields and grass land in winter, show high correlation, whereas in summer higher temporal decorrelation can be seen due to fast growing nonforest vegetation in these areas. Urban and industrial areas show intermediate to high correlation. Correlation over these regions becomes smaller with increasing baseline, because the larger the baseline, the less similar is the view of the urban areas in the different passes.

Height determination accuracy also, depends on how accurate is the range, height of InSAR system, baseline and phase. Uncertainty in range is caused by system clock timing and atmospheric and ionospheric propagation delay inaccuracy. Inaccuracy in height decreases when the look angle increases, but it must be as large as possible to avoid loss of information due to layover. Inaccuracies due to uncertainty in the determination of the length of the baseline imposes severe constraints on the interferometric baseline knowledge. This type of error can be removed using known heights of a few control points. In the next chapter, a model is developed which incorporates ground control data for height estimation.

# *Chapter Four*

# Terrain Elevations From InSAR Incorporating Ground Data

## 4.1. Introduction

Inaccuracies in elevations derived from InSAR have been discussed in the previous chapter. It has been showed that uncertainties in orbit determination cause an absolute error in elevations of the order of several hundred metres. It has been mentioned that they are systematic errors which affect every point in the image, and can be removed using heights of a few control points. A model is developed to calculate absolute terrain elevations incorporating ground control data. The computation procedure is based on stereo radargrammetric mapping of overlapping SAR images, incorporating expressions for elevations based on the fringe information in InSAR. The model develops a simultaneous least squares adjustment of all the measurements by radargrammetry and interferometric SAR together with ground control, using condition and observation equations. In this case the basic measurements include range, unwrapped phase, and the ground coordinates of control points. The purpose of the least squares adjustment is to determine the most probable solution for the ground coordinates of points identified in the image.

In the following sections the necessary observation equations are developed, the mathematical model for the solution of all equations is formulated and finally an efficient computation algorithm is presented.

## 4.2. Development of observation equations

A general formulation for radar stereo computations is given by Dowman (1992). They used two fundamental relationships: the SAR Doppler and range equations. The

Doppler equation gives the Doppler frequency which is determined in the SAR processing. The SAR range equation defines the distance from the sensor to the target. The equations for a one point in the image are:

$$f_D = \frac{2}{\lambda r}(\dot{\mathbf{S}} - \dot{\mathbf{P}}) \cdot (\mathbf{S} - \mathbf{P}) \tag{4.1}$$

$$r = |\mathbf{S} - \mathbf{P}| \tag{4.2}$$

where $f_D$, $\lambda$, r are the Doppler frequency associated with the return signal, the radar wavelength, and the sensor to target slant range, respectively. **S** and **P** are position vectors of the sensor and target, $\dot{\mathbf{S}}$ and $\dot{\mathbf{P}}$ are the velocity vector of the sensor and target, respectively. A pair of images result in four equations. If sufficient orbit and Doppler information are available, the above equations can be used to determine the coordinates of a point that appears in both images.

However, as was described previously in section 2.8, SAR is able to record also the phase values of the received radar signals, which can provide valuable information about the elevation of the target. For a repeat-pass InSAR system, it can be written as:

$$r_1 - r_2 = \lambda\varphi / 4\pi$$

or

$$|\mathbf{S}_1 - \mathbf{P}| - |\mathbf{S}_2 - \mathbf{P}| = \lambda\varphi / 4\pi \tag{4.3}$$

Where $\mathbf{S_1}$ ($S_{1x}$, $S_{1y}$, $S_{1z}$) $\mathbf{S_2}$ ($S_{2x}$, $S_{2y}$, $S_{2z}$) are position vectors of satellites 1 and 2, $\mathbf{r_1}$ and $\mathbf{r_2}$ are the ranges to the target from satellites 1 and 2, and **P** is the position vector of target as are shown in figure 4.1.

It was intended to treat the range and Doppler equations as well as InSAR equation as observation equations to determine the coordinates of the interest points. However,

values relating to the Doppler frequency in the header data files provided by the Vexcel software were unusable, because they were of insufficient accuracy. Therefore it was decided that the work continues without using Doppler equations. Hence two range equations (radargrammetry) and the phase equation (InSAR) are used in the study.

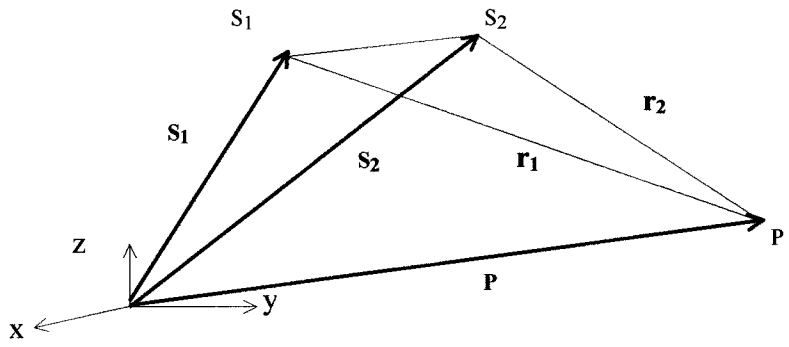


**Figure 4.1 Radar stereo intersection.**

Therefore, for two images equation 4.2 and 4.3 can be rewritten by following equations.

$$F_1 = r_1 - |\mathbf{S_1} - \mathbf{P}| = 0$$

$$F_2 = r_2 - |\mathbf{S_1} - \mathbf{P}| = =0 \qquad (4.4)$$

$$F_3 = |\mathbf{S_1} - \mathbf{P}| - |\mathbf{S_2} - \mathbf{P}| - {}^{\lambda\varphi}/_{4\pi} = 0$$

The above equations are non-linear and therefore they must be linearised before the unknowns can be solved.

To determine the position of the sensors, we firstly need to calculate the time each pixel was recorded and secondly to propagate the nearest statevector of the satellite for that time. Time ($T_p$) of acquisition of pixel can be derived by using the following equation:

$$T_p=T_0+T_{off}+i/PRF \qquad (4.5)$$

Where $T_0$ is the parameter of raw-data-start-time, $T_{off}$ is the parameter azimuth-offset, i is the azimuth line number containing the target of interest and PRF is the pulse repetition frequency. These parameters are provided in the header data file in each image. Propagation of statevectors (also provided by the header data file) can be carried out by interpolation using a low order polynomials. The calculations have shown that in this case, second order polynomials for orbit are the most suitable interpolators (see sections 5.7-8). Therefore:

$$\begin{aligned}
S_{1x}&=a_{1x}t_{1p}^2+b_{1x}t_{1p}+c_{1x}\\
S_{1y}&=a_{1y}t_{1p}^2+b_{1y}t_{1p}+c_{1y}\\
S_{1z}&=a_{1z}t_{1p}^2+b_{1z}t_{1p}+c_{1z} \qquad (4.6)\\
S_{2x}&=a_{2x}t_{2p}^2+b_{2x}t_{2p}+c_{2x}\\
S_{2y}&=a_{2y}t_{2p}^2+b_{2y}t_{2p}+c_{2y}\\
S_{2z}&=a_{2z}t_{2p}^2+b_{2z}t_{2p}+c_{2z}
\end{aligned}$$

Where $a_{1x}$, $b_{1x}$, $c_{1x}$, …. , $c_{2z}$ are polynomials coefficients. The subscripts 1 and 2 refer to satellites 1 and 2, while subscripts x, y, and z refer to satellites' components of x, y, z directions in satellites' coordinates system.

The ancillary data (section 5.7.1) provided with the images is used to compute the coefficients of the polynomials. The range values for each pixel and the unwrapped phase measurements at each point will be treated as observations in the model. From this non-linear system of equations we need to solve the unknown coordinates of P by a least-squares algorithm.

Linearisation of equations 4.4 is carried out by Taylor's series. The observations are written in terms of measured quantities, true quantities and the corrections needed to account for the random error in the measured quantities; i.e. residuals, as follows:

$$
\begin{aligned}
r_{1i} &= \overset{\circ}{r}_{1i} + vr_{1i} \\
r_{2i} &= \overset{\circ}{r}_{2i} + vr_{2i} \\
\varphi_i &= \overset{\circ}{\varphi}_i + v\varphi_i
\end{aligned}
\qquad (4.7)
$$

Similarly, the unknown parameters of P are expressed in terms of an approximate value and corresponding correction:

$$
\begin{aligned}
X_i &= \overset{\circ}{X}_i + \Delta X_i \\
Y_i &= \overset{\circ}{Y}_i + \Delta Y_i \\
Z_i &= \overset{\circ}{Z}_i + \Delta Z_i
\end{aligned}
$$

Similarly, polynomials parameters are expressed as:

$$
\begin{aligned}
a_{1x} &= \overset{\circ}{a}_{1x} + \Delta a_{1x} \\
b_{1x} &= \overset{\circ}{b}_{1x} + \Delta b_{1x} \\
c_{1x} &= \overset{\circ}{c}_{1x} + \Delta c_{1x} \\
&\cdots\cdots\cdots\cdots\cdots \\
&\cdots\cdots\cdots\cdots\cdots \\
c_{2z} &= \overset{\circ}{c}_{2z} + \Delta c_{2z}
\end{aligned}
\qquad (4.8)
$$

Therefore, the linearised form of equation 4.4, based on Taylor's series, and neglecting terms of order higher than one, become:

$$\begin{aligned}
&\frac{\partial F_{1i}}{\partial r_{1i}} Vr_{1i} + \frac{\partial F_{1i}}{\partial r_{2i}} Vr_{2i} + \frac{\partial F_{1i}}{\partial \varphi_i} V_{\varphi i} + \frac{\partial F_{1i}}{\partial a_{1x}} \Delta a_{1x} + \frac{\partial F_{1i}}{\partial b_{1x}} \Delta b_{1x} + \frac{\partial F_{1i}}{\partial c_{1x}} \Delta c_{1x} + \cdots + \frac{\partial F_{1i}}{\partial c_{2z}} \Delta c_{2z} = F_{1i}^{\circ} \\
&\frac{\partial F_{2i}}{\partial r_{1i}} Vr_{1i} + \frac{\partial F_{2i}}{\partial r_{2i}} Vr_{2i} + \frac{\partial F_{2i}}{\partial \varphi_i} V_{\varphi i} + \frac{\partial F_{2i}}{\partial a_{1x}} \Delta a_{1x} + \frac{\partial F_{2i}}{\partial b_{1x}} \Delta b_{1x} + \frac{\partial F_{2i}}{\partial c_{1x}} \Delta c_{1x} + \cdots + \frac{\partial F_{2i}}{\partial c_{2z}} \Delta c_{2z} = F_{2i}^{\circ} \\
&\frac{\partial F_{3i}}{\partial r_{1i}} Vr_{1i} + \frac{\partial F_{3i}}{\partial r_{2i}} Vr_{2i} + \frac{\partial F_{3i}}{\partial \varphi_i} V_{\varphi i} + \frac{\partial F_{3i}}{\partial a_{1x}} \Delta a_{1x} + \frac{\partial F_{3i}}{\partial b_{1x}} \Delta b_{1x} + \frac{\partial F_{3i}}{\partial c_{1x}} \Delta c_{1x} + \cdots + \frac{\partial F_{3i}}{\partial c_{2z}} \Delta c_{2z} = F_{3i}^{\circ}
\end{aligned} \tag{4.9}$$

Where $\overset{\circ}{F}_{1i}$, $\overset{\circ}{F}_{2i}$, and $\overset{\circ}{F}_{3i}$ are the functions $F_{1i}$, $F_{2i}$, $F_{3i}$ evaluated with the approximate values $\overset{\circ}{X}_i, \overset{\circ}{Y}_i, \overset{\circ}{Z}_i, \overset{\circ}{a}_{1x}, \overset{\circ}{b}_{1x}, \ldots, \overset{\circ}{c}_{2z}$. Similarly, the partial derivatives are also computed using these approximations. The solution is iterative and hence the computed values of $\overset{\circ}{X}_i, \overset{\circ}{Y}_i, \overset{\circ}{Z}_i, \overset{\circ}{a}_{1x}, \overset{\circ}{b}_{1x}, \ldots, \overset{\circ}{c}_{2z}$ will converge to their estimated true values. The computed corrections ($\Delta X_i, \Delta Y_i, \Delta Z_i, \Delta a_{1x}, \Delta b_{1x}, \Delta c_{1x}, \ldots, \Delta c_{2z}$) from each iteration are applied to their corresponding approximate values. The corrected parameters are then used as approximate values in the next iteration, and the iteration process is repeated until the corrections ($\Delta X_i, \Delta Y_i, \Delta Z_i, \Delta a_{1x}, \Delta b_{1x}, \Delta c_{1x}, \ldots, \Delta c_{2z}$) become negligibly small.

The linearised form of equations 4.9 can be written as:

$$\begin{aligned}
&a_{11} V_{r1i} + a_{12} Vr_{2i} + a_{13} V_{\varphi i} + b_{11} \Delta x_i + b_{12} \Delta y_i + b_{13} \Delta z_i + c_{11} \Delta a_{1x} + c_{12} \Delta b_{1x} + \cdots + c_{1,18} \Delta c_{2z} = F_{1i}^{\circ} \\
&a_{21} V_{r1i} + a_{22} Vr_{2i} + a_{23} V_{\varphi i} + b_{21} \Delta x_i + b_{22} \Delta y_i + b_{23} \Delta z_i + c_{21} \Delta a_{1x} + c_{22} \Delta b_{1x} + \cdots + c_{2,18} \Delta c_{2z} = F_{2i}^{\circ} \\
&a_{31} V_{r1i} + a_{32} Vr_{2i} + a_{33} V_{\varphi i} + b_{31} \Delta x_i + b_{32} \Delta y_i + b_{33} \Delta z_i + c_{31} \Delta a_{1x} + c_{32} \Delta b_{1x} + \cdots + c_{3,18} \Delta c_{2z} = F_{3i}^{\circ}
\end{aligned} \tag{4.10}$$

where $a_{ij}$ (i,j = 1-3) are the partial derivatives of equation 4.4 in terms of range and phase measurements, $b_{ij}$ (i,j = 1-3) are the partial derivatives of equation 4.4 in terms of components of point P (X, Y, Z), and $c_{ij}$ (i,j = 1-3, j = 1-18) are the partial derivatives of equation 4.4 in terms of satellite positions polynomials.

Expressing equation 4.10 in matrix notation:

$$A_{1i}V + \overset{\bullet}{B}_i \overset{\bullet}{\Delta}_i + \overset{\bullet\bullet}{B}_i \overset{\bullet\bullet}{\Delta} = C_{1i} \qquad (4.11)$$

Where

V is the vector of residuals to the observations.

$\overset{\bullet}{\Delta}$ is the vector of correction to the approximate solution of point P.

A is the coefficient matrix of partial derivatives in terms of the observations.

$\overset{\bullet}{B}$ is the coefficient matrix of partial derivatives in terms of the unknown ground coordinates of point P.

$\overset{\bullet\bullet}{B}$ is the coefficient matrix of the partial derivatives in terms of satellite position polynomials.

$\overset{\bullet\bullet}{\Delta}$ is the vector of correction to the approximate solution of satellite's position polynomials.

The superscript '$\bullet$' is used to denote corrections to the ground coordinates parameters, and '$\bullet\bullet$' is used to denote corrections to the coefficient parameters.

Therefore the elements of equation 4.11 are as follows:

$$\overset{\bullet}{B}_i = \begin{bmatrix} b_{11} & b_{12} & b_{13} \\ b_{21} & b_{22} & b_{23} \\ b_{31} & b_{32} & b_{33} \end{bmatrix} \quad A_{1i} = \begin{bmatrix} a_{11} & a_{12} & a_{13} \\ a_{21} & a_{22} & a_{23} \\ a_{31} & a_{32} & a_{33} \end{bmatrix} = \begin{bmatrix} 1 & 0 & 0 \\ 0 & 1 & 0 \\ 0 & 0 & -\lambda/4\pi \end{bmatrix} \quad \overset{\bullet}{\Delta}_i = \begin{bmatrix} \Delta x_i \\ \Delta y_i \\ \Delta z_i \end{bmatrix}$$

$$\overset{\bullet\bullet}{B}_i = \begin{bmatrix} c_{11} & c_{12} & c_{13} & . & . & c_{1n} \\ c_{21} & c_{22} & c_{23} & . & . & c_{2n} \\ c_{31} & c_{32} & c_{33} & . & . & c_{3n} \end{bmatrix} \quad \overset{\bullet\bullet}{\Delta} = \begin{bmatrix} \Delta a_{1x} \\ \Delta b_{1x} \\ \Delta c_{1z} \\ . \\ . \\ \Delta c_{2z} \end{bmatrix} \quad C_{1i} = \begin{bmatrix} F_{1i} \\ F_{2i} \\ F_{3i} \end{bmatrix} \quad V_{1i} = \begin{bmatrix} Vr_{1i} \\ Vr_{2i} \\ V\varphi i \end{bmatrix}$$

(4.12)

Where the elements of $\overset{\bullet}{B}_i$, partial derivatives in terms of the unknown ground coordinates of point i, are:

$$
\begin{aligned}
b_{11} &= -\frac{X_i - S_{1xi}}{N_i} \\
b_{12} &= -\frac{Y_i - S_{1yi}}{N_i} \\
b_{13} &= -\frac{Z_i - S_{1zi}}{N_i} \\
b_{21} &= -\frac{X_i - S_{2xi}}{R_i} \\
b_{22} &= -\frac{Y_i - S_{2yi}}{R_i} \\
b_{23} &= -\frac{Z_i - S_{2zi}}{R_i} \\
b_{31} &= -b_{11} + b_{21} \\
b_{32} &= -b_{12} + b_{22} \\
b_{33} &= -b_{13} + b_{23}
\end{aligned}
\tag{4.13}
$$

Where N and R are as follow:

$$
\begin{aligned}
N &= \sqrt{(S_{1x} - X)^2 + (S_{1y} - Y)^2 + (S_{1z} - Z)^2} \\
R &= \sqrt{(S_{2x} - X)^2 + (S_{2y} - Y)^2 + (S_{2z} - Z)^2}
\end{aligned}
\tag{4.14}
$$

Similarly $\ddot{B}$ consists of following elements, which are the partial derivatives in terms of satellite position polynomials.

$$
\begin{aligned}
c_{1,1} &= \frac{\partial F_1}{\partial a_{1x}} = \frac{\partial F_1}{\partial S_{1x}} \frac{\partial S_{1x}}{\partial a_{1x}} = \frac{X - S_{1x}}{N} t_{1p}^2 \\
c_{1,2} &= \frac{\partial F_1}{\partial b_{1x}} = \frac{\partial F_1}{\partial S_{1x}} \frac{\partial S_{1x}}{\partial b_{1x}} = \frac{X - S_{1x}}{N} t_{1p} \\
c_{1,3} &= \frac{\partial F_1}{\partial c_{1x}} = \frac{\partial F_1}{\partial S_{1x}} \frac{\partial S_{1x}}{\partial c_{1x}} = \frac{X - S_{1x}}{N} \\
c_{1,4} &= \frac{\partial F_1}{\partial a_{1y}} = \frac{\partial F_1}{\partial S_{1y}} \frac{\partial S_{1y}}{\partial a_{1y}} = \frac{Y - S_{1y}}{N} t_{1p}^2 \\
c_{1,5} &= \frac{\partial F_1}{\partial b_{1y}} = \frac{\partial F_1}{\partial S_{1y}} \frac{\partial S_{1y}}{\partial b_{1y}} = \frac{Y - S_{1y}}{N} t_{1p} \\
c_{1,6} &= \frac{\partial F_1}{\partial c_{1y}} = \frac{\partial F_1}{\partial S_{1y}} \frac{\partial S_{1y}}{\partial c_{1y}} = \frac{Y - S_{1y}}{N}
\end{aligned}
$$

$$c_{1,7} = \frac{\partial F_1}{\partial a_{1z}} = \frac{\partial F_1}{\partial S_{1z}} \frac{\partial S_{1z}}{\partial a_{1z}} = \frac{Z - S_{1z}}{N} t_{1p}^2$$

$$c_{1,8} = \frac{\partial F_1}{\partial b_{1z}} = \frac{\partial F_1}{\partial S_{1z}} \frac{\partial S_{1z}}{\partial b_{1z}} = \frac{Z - S_{1z}}{N} t_{1p}$$

$$c_{1,9} = \frac{\partial F_1}{\partial c_{1z}} = \frac{\partial F_1}{\partial S_{1z}} \frac{\partial S_{1z}}{\partial c_{1z}} = \frac{Z - S_{1z}}{N}$$

$$\frac{\partial F_1}{\partial a_{2x}} = \frac{\partial F_1}{\partial b_{2x}} = \frac{\partial F_1}{\partial c_{2x}} = \cdots = \frac{\partial F_1}{\partial c_{2z}} = 0 \qquad \text{Hence} \qquad c_{1,10} = c_{1,11} = \ldots = c_{1,18} = 0$$

$$\frac{\partial F_2}{\partial a_{1x}} = \frac{\partial F_2}{\partial b_{1x}} = \frac{\partial F_2}{\partial c_{1x}} = \cdots = \frac{\partial F_2}{\partial c_{1z}} = 0 \qquad \text{Hence} \qquad c_{2,1} = c_{2,2} = \ldots\ldots\ldots = c_{2,9} = 0$$

$$c_{2,10} = \frac{\partial F_2}{\partial a_{2x}} = \frac{\partial F_2}{\partial S_{2x}} \frac{\partial S_{2x}}{\partial a_{2x}} = \frac{X - S_{2x}}{R} t_{1p}^2$$

$$c_{2,11} = \frac{\partial F_2}{\partial b_{2x}} = \frac{\partial F_2}{\partial S_{2x}} \frac{\partial S_{2x}}{\partial b_{2x}} = \frac{X - S_{2x}}{R} t_{1p}$$

$$c_{2,12} = \frac{\partial F_2}{\partial c_{2x}} = \frac{\partial F_2}{\partial S_{2x}} \frac{\partial S_{2x}}{\partial c_{2x}} = \frac{X - S_{2x}}{R}$$

$$c_{2,13} = \frac{\partial F_2}{\partial a_{2y}} = \frac{\partial F_2}{\partial S_{2y}} \frac{\partial S_{2y}}{\partial a_{2y}} = \frac{Y - S_{2y}}{R} t_{2p}^2$$

$$c_{2,14} = \frac{\partial F_2}{\partial b_{2y}} = \frac{\partial F_2}{\partial S_{2y}} \frac{\partial S_{2y}}{\partial b_{2y}} = \frac{Y - S_{2y}}{R} t_{2p}$$

$$c_{2,15} = \frac{\partial F_2}{\partial c_{2y}} = \frac{\partial F_2}{\partial S_{2y}} \frac{\partial S_{2y}}{\partial c_{2y}} = \frac{Y - S_{2y}}{R}$$

$$c_{2,16} = \frac{\partial F_2}{\partial a_{2z}} = \frac{\partial F_2}{\partial S_{2z}} \frac{\partial S_{2z}}{\partial a_{2z}} = \frac{Z - S_{2z}}{R} t_{2p}^2$$

$$c_{2,17} = \frac{\partial F_2}{\partial b_{2z}} = \frac{\partial F_2}{\partial S_{2z}} \frac{\partial S_{2z}}{\partial b_{2z}} = \frac{Z - S_{2z}}{R} t_{2p}$$

$$c_{2,18} = \frac{\partial F_2}{\partial c_{2z}} = \frac{\partial F_2}{\partial S_{2z}} \frac{\partial S_{2z}}{\partial c_{2z}} = \frac{Z - S_{2z}}{R}$$

$c_{3,1} = -c_{1,1}$ $\quad c_{3,2} = -c_{1,2} \ldots c_{3,9} = -c_{1,9}$

$c_{3,10} = c_{2,10}$ $\quad c_{3,11} = c_{2,11} \ldots c_{3,18} = c_{2,18}$ (4.15)

### 4.2.1 Extending to n points

For n points observed in an image, the complete collection of observation equations for the collinearity equations will be:

$$A_{11}V_{11} + \dot{B}_1\dot{\Delta}_1 + \ddot{B}_1\ddot{\Delta} = C_{11}$$

$$A_{12}V_{12} + \dot{B}_2\dot{\Delta}_2 + \ddot{B}_2\ddot{\Delta} = C_{12}$$

$$\ldots\ldots\ldots\ldots\ldots\ldots \qquad (4.16)$$

$$\ldots\ldots\ldots\ldots\ldots\ldots$$

$$A_{1n}V_{1n} + \dot{B}_n\dot{\Delta}_n + \ddot{B}_n\ddot{\Delta} = C_{1n}$$

or

$$A_1V_1 + \dot{B}\dot{\Delta} + \ddot{B}\ddot{\Delta} = C_1 \qquad (4.17)$$

Where:

$$A_1 = \begin{bmatrix} A_{11} & & & \\ & A_{12} & & \\ & & . & \\ & & & A_{1n} \end{bmatrix}_{3n,3n} \qquad \dot{B} = \begin{bmatrix} \dot{B}_1 & & & \\ & \dot{B}_2 & & \\ & & . & \\ & & & \dot{B}_n \end{bmatrix}_{3n,3n}$$

$$\dot{\Delta} = \begin{bmatrix} \dot{\Delta}_1 \\ \dot{\Delta}_2 \\ . \\ . \\ \dot{\Delta}_n \end{bmatrix}_{3n,1} \qquad C_1 = \begin{bmatrix} C_{11} \\ C_{12} \\ . \\ . \\ C_{1n} \end{bmatrix}_{3n,1} \qquad V_1 = \begin{bmatrix} V_{11} \\ V_{12} \\ . \\ . \\ V_{1n} \end{bmatrix}_{3n,1} \qquad \ddot{B} = \begin{bmatrix} \ddot{B}_1 \\ \ddot{B}_2 \\ . \\ . \\ \ddot{B}_n \end{bmatrix}_{3n,18}$$

## 4.3. Observation equations for ground control

Observations on ground controls are point coordinates. The true parameters and observed values of the control points $\overset{\circ\circ}{X}, \overset{\circ\circ}{Y}, \overset{\circ\circ}{Z}$ and their residuals $V_x$, $V_y$, $V_z$ are related by:

$$X_i = \overset{\circ\circ}{X}_i + V_{Xi}$$

$$\begin{aligned} Y_i &= \overset{oo}{Y}_i + V_{Yi} \\ Z_i &= \overset{oo}{Z}_i + V_{Zi} \end{aligned} \qquad (4.18)$$

Furthermore, equation 4.6 relates estimates of parameters to approximate values and corrections to the approximate values as follows:

$$\begin{aligned} X_i &= \overset{o}{X}_i + \Delta X_i \\ Y_i &= \overset{o}{Y}_i + \Delta Y_i \\ Z_i &= \overset{o}{Z}_i + \Delta Z_i \end{aligned} \qquad (4.19)$$

Therefore:

$$\begin{aligned} \overset{oo}{X}_i + V_{Xi} &= \overset{o}{X}_i + \Delta X_i \\ \overset{oo}{Y}_i + V_{Yi} &= \overset{o}{Y}_i + \Delta Y_i \\ \overset{oo}{Z}_i + V_{Zi} &= \overset{o}{Z}_i + \Delta Z_i \end{aligned} \qquad (4.20)$$

Rearranging terms and putting the equations into matrix notations yields:

$$\begin{bmatrix} V_{Xi} \\ V_{Yi} \\ V_{Zi} \end{bmatrix} - \begin{bmatrix} \Delta X_i \\ \Delta Y_i \\ \Delta Z_i \end{bmatrix} = \begin{bmatrix} \overset{o}{X}_i - \overset{oo}{X}_i \\ \overset{o}{Y}_i - \overset{oo}{Y}_i \\ \overset{o}{Z}_i - \overset{oo}{Z}_i \end{bmatrix}$$

Or:

$$V_{2i} - \overset{\bullet}{\Delta}_i = C_{2i} \qquad (4.21)$$

There are therefore the observation equations for known ground coordinates of point i. the observation equation for n control observations can be expressed as:

$$V_{21} - \overset{\bullet}{\Delta}_1 = C_{21}$$

$$V_{22} - \dot{\Delta}_2 = C_{22}$$

.....

.....

$$V_{2i} - \dot{\Delta}_i = C_{2i}$$

or

$$\underset{3n,1}{V_2} - \underset{3n,1}{\dot{\Delta}} = \underset{3n,1}{C_2} \qquad (4.22)$$

## 4.4. Observation equations for satellite position

Observations of the geographic location of satellite can be formed into observation equations. The true and observed values of the polynomial coefficients ($\overset{oo}{a}_{1x}, \overset{oo}{b}_{1x}, \overset{oo}{c}_{1x}, \overset{oo}{a}_{1y}, \ldots, \overset{oo}{c}_{2z}$), and their residuals ($Va_{1x}$, $V_{b1x}$, $Vc_{1x}$, ..., $Vc_{2z}$) are related by:

$$\begin{aligned} a_{1x} &= \overset{oo}{a}_{1x} + Va_{1x} \\ b_{1x} &= \overset{oo}{b}_{1x} + Vb_{1x} \\ &\ldots\ldots \\ &\ldots\ldots \\ c_{2z} &= \overset{oo}{c}_{2z} + Vc_{2z} \end{aligned} \qquad (4.23)$$

Equations 4.6 relate estimates of the parameters to approximations, and corrections to approximation in the following form:

$$\begin{aligned} a_{1x} &= \overset{o}{a}_{1x} + \Delta a_{1x} \\ b_{1x} &= \overset{o}{b}_{1x} + \Delta b_{1x} \\ &\ldots\ldots \\ &\ldots\ldots \end{aligned} \qquad (4.24)$$

$$c_{2z} = \overset{\circ}{c}_{2z} + \Delta c_{2z}$$

Therefore:

$$\begin{aligned}
&\overset{\circ\circ}{a}_{1x} + Va_{1x} = \overset{\circ}{a}_{1x} + \Delta a_{1x} \\
&\overset{\circ\circ}{b}_{1x} + Vb_{1x} = \overset{\circ}{b}_{1x} + \Delta b_{1x} \\
&\ldots\ldots\ldots\ldots\ldots\ldots\ldots\ldots \\
&\ldots\ldots\ldots\ldots\ldots\ldots\ldots\ldots \\
&\overset{\circ\circ}{c}_{2z} + Vc_{2z} = \overset{\circ}{c}_{2z} + \Delta c_{2z}
\end{aligned} \qquad (4.25)$$

Rearranging term and putting the equations into the matrix form yields:

$$\begin{bmatrix} Va_{1x} \\ Vb_{1x} \\ . \\ . \\ Vc_{2z} \end{bmatrix} - \begin{bmatrix} \Delta a_{1x} \\ \Delta b_{1x} \\ . \\ . \\ \Delta c_{2z} \end{bmatrix} = \begin{bmatrix} \overset{\circ}{a}_{1x} - \overset{\circ\circ}{a}_{1x} \\ \overset{\circ}{b}_{1x} - \overset{\circ\circ}{b}_{1x} \\ . \\ . \\ \overset{\circ}{c}_{2z} - \overset{\circ\circ}{c}_{2z} \end{bmatrix}$$

or

$$\underset{18,1}{V_3} - \underset{18,1}{\overset{\bullet\bullet}{\Delta}} = \underset{18,1}{C_3} \qquad (4.26)$$

## 4.5. Combined formulation of the mathematical model

Combining equations of 4.17, 4.22, and 4.26 gives a complete mathematical model of the problem:

$$\begin{aligned}
&A_1 V_1 + B\overset{\bullet}{\Delta} + B\overset{\bullet\bullet}{\Delta} = C_1 \\
&V_2 - \overset{\bullet}{\Delta} = C_2 \\
&V_3 - B\overset{\bullet\bullet}{\Delta} = C_3
\end{aligned} \qquad (4.27)$$

Expressing this equation as a single matrix, the following equation can be formed.

$$\begin{bmatrix} A_1 & & \\ & I & \\ & & I \end{bmatrix}\begin{bmatrix} V_1 \\ V_2 \\ V_3 \end{bmatrix}+\begin{bmatrix} \dot{B} & \ddot{B} \\ -I & 0 \\ 0 & -I \end{bmatrix}\begin{bmatrix} \dot{\Delta} \\ \ddot{\Delta} \end{bmatrix}=\begin{bmatrix} C_1 \\ C_2 \\ C_3 \end{bmatrix}$$

or

$$\underset{(6n+18,6n+18)}{A}\ \underset{(6n+18,1)}{V}+\underset{(6n+18,3n+1)}{B}\ \underset{(3n+18,1)}{\Delta}=\underset{(6n+18,1)}{C} \qquad (4.28)$$

## 4.6. The weight matrix

In least squares adjustments, the weight of an observation is inversely proportional to the population variance of the measurement (Mikhail, 1976). i.e.:

$$W_i \propto 1/\sigma_i^2$$

Where $W_i$ denotes the weight of measurement of i and $\sigma_i^2$ is variance of the measurement.

The variance-covariance matrix for satellite range and phase difference measurements for point i is of the form;

$$Q_i=\begin{bmatrix} \sigma_{r_{1i}}^2 & & \\ & \sigma_{r_{2i}}^2 & \\ & & \sigma_{\varphi_i}^2 \end{bmatrix} \qquad (4.29)$$

assuming no correlation between observations.

Where $\sigma_{r_{1i}}^2, \sigma_{r_{2i}}^2$, and $\sigma_{\varphi_i}^2$ are the variances of the measurements $r_{1i}$, $r_{2i}$, and $\varphi_i$ respectively. The corresponding weight matrix is then defined as:

$$W_{1i} = (A_{1i}Q_iA_{1i}^T)^{-1} = \begin{bmatrix} Wr_{1i} & & \\ & Wr_{2i} & \\ & & W\varphi_i \end{bmatrix} \quad (4.30)$$

The weight matrix for all n observed points is:

$$W_1 = \begin{bmatrix} W_{11} & & & \\ & W_{12} & & \\ & & . & \\ & & & W_{1n} \end{bmatrix}_{3n,3n} \quad (4.31)$$

Where each element in equation 4.31 is of the form of equation 4.30 and assuming no correlation between observations of each point. $W_1$ is therefore a diagonal matrix of dimension 3n*3n.

The weight matrix of the control coordinates of point i is expressed by:

$$W_{2i} = \begin{bmatrix} \sigma_{X_i}^2 & & \\ & \sigma_{Y_i}^2 & \\ & & \sigma_{Z_i}^2 \end{bmatrix}^{-1} = \begin{bmatrix} W_{X_i} & & \\ & W_{Y_i} & \\ & & W_{Z_i} \end{bmatrix} \quad (4.32)$$

Where no correlation is assumed.

Extending this weight matrix to represent the weight matrix for n control points gives:

$$W_2 = \begin{bmatrix} W_{21} & & & \\ & W_{22} & & \\ & & . & \\ & & & W_{2n} \end{bmatrix}_{3n,3n} \quad (4.33)$$

Similarly, the weight matrix of coefficients of polynomials, the two satellite paths, assuming no correlation, is given by;

$$W_3 = \begin{bmatrix} \sigma^2_{a1x} & & & & \\ & \sigma^2_{b1x} & & & \\ & & \sigma^2_{c1x} & & \\ & & & \ddots & \\ & & & & \sigma^2_{c2z} \end{bmatrix}^{-1}_{18,18} \qquad (4.34)$$

## 4.7. Structure of the normal equations.

The total least squares solution (Mikhail, 1976) to the model in equation (4.28) results in the following normal equation;

$$(B^T W\ B)\Delta = B^T W\ C \qquad (4.35)$$

Where W is the complete weight matrix composed of the three described submatrices given by:

$$W = \begin{bmatrix} W_1 & & \\ & W_2 & \\ & & W_3 \end{bmatrix}_{6n+18,6n+18} \qquad (4.36)$$

Developing equation 4.35 into the individual elements shown in equation 4.28 result in the following normal equation;

$$\begin{bmatrix} \dot{B}^T & & \\ -I & 0 & \\ \ddot{B}^T & 0 & -I \end{bmatrix} \begin{bmatrix} W_1 & & \\ & W_2 & \\ & & W_3 \end{bmatrix} \begin{bmatrix} \dot{B} & \ddot{B} \\ -I & 0 \\ 0 & -I \end{bmatrix} \begin{bmatrix} \dot{\Delta} \\ \ddot{\Delta} \end{bmatrix} = \begin{bmatrix} \dot{B}^T & & \\ -I & 0 & \\ \ddot{B}^T & 0 & -I \end{bmatrix} \begin{bmatrix} W_1 & & \\ & W_2 & \\ & & W_3 \end{bmatrix} \begin{bmatrix} C_1 \\ C_2 \\ C_3 \end{bmatrix} \qquad (4.37)$$

$$\begin{bmatrix} \dot{B}^T W_1 \dot{B} + W_2 & \dot{B}^T W_1 \ddot{B} \\ \ddot{B}^T W_1 \dot{B} & \ddot{B}^T W_1 \ddot{B} + W_3 \end{bmatrix} \begin{bmatrix} \dot{\Delta} \\ \ddot{\Delta} \end{bmatrix} = \begin{bmatrix} \dot{B}^T W_1 C_1 - W_2 C_2 \\ \ddot{B}^T W_1 C_1 - W_3 C_3 \end{bmatrix} \tag{4.38}$$

or

$$\begin{bmatrix} \ddot{B}^T W_1 \ddot{B} + W_3 & \ddot{B}^T W_1 \dot{B} \\ \dot{B}^T W_1 \ddot{B} & \dot{B}^T W_1 \dot{B} + W_2 \end{bmatrix} \begin{bmatrix} \ddot{\Delta} \\ \dot{\Delta} \end{bmatrix} = \begin{bmatrix} \ddot{B}^T W_1 C_1 - W_3 C_3 \\ \dot{B}^T W_1 C_1 - W_2 C_2 \end{bmatrix} \tag{4.39}$$

Equation 4.35 may be simply expressed as

$$N\Delta = T \tag{4.40}$$

Where N, $\Delta$, and T are expressed in equation 4.39.

## 4.8. Computing algorithm for the normal equations

The direct solution of the set of equation 4.40 will involve solving 6n+18 simultaneous equations. For a large of number of points, the size of the normal equation can be so large as to make its solution impractical. Therefore, an efficient algorithm is needed to solve the problem for large n. In the following a computing algorithm is described, which is based on a method described by Wong (1980) for simultaneous solving of photogrammetric block.

Substituting of the equations that have already been developed in equation 4.39, it can be shown that;

$$N = \begin{bmatrix} \overset{oo}{N} & \bar{N}_1^t & \bar{N}_2^t & . & . & \bar{N}_n^t \\ \bar{N}_1 & \overset{o}{N}_1 + W_{21} & & & & \\ \bar{N}_2 & & \overset{o}{N}_2 + W_{22} & & & \\ . & & & . & & \\ . & & & & . & \\ \bar{N}_n & & & & & \overset{o}{N}_n + W_{2n} \end{bmatrix}$$

$$\Delta = \begin{bmatrix} \overset{\bullet\bullet}{\Delta} \\ \overset{\bullet}{\Delta}_1 \\ \overset{\bullet}{\Delta}_2 \\ . \\ . \\ \overset{\bullet}{\Delta}_n \end{bmatrix} \qquad T = \begin{bmatrix} \overset{oo}{T} \\ \overset{o}{T}_1 \\ \overset{o}{T}_2 \\ . \\ . \\ \overset{o}{T}_n \end{bmatrix} \tag{4.41}$$

Where:

$$\overset{oo}{N} = \sum_{i=1}^{n} \overset{oo}{N}_i + W_3 = \sum_{i=1}^{n} \overset{\bullet\bullet t}{B_i} W_{1i} \overset{\bullet\bullet}{B_i} + W_3$$

$$\bar{N}_i = \overset{\bullet t}{B_i} W_{1i} \overset{\bullet\bullet}{B_i}$$

$$\bar{N}_i^t = \overset{\bullet\bullet t}{B_i} W_{1i} \overset{\bullet}{B_i}$$

$$\overset{oo}{T}_i = \overset{\bullet\bullet t}{B_i} W_{1i} C_{1i} \qquad \overset{oo}{T} = \sum \overset{oo}{T}_i - W_3 C_3 \tag{4.42}$$

$$\overset{o}{T}_i = \overset{\bullet t}{B_i} W_{1i} C_{1i} - W_{2i} C_{2i}$$

$$\overset{o}{N}_i = \overset{\bullet t}{B_i} W_{1i} \overset{\bullet}{B_i}$$

The following facts can be observed from equation 4.41:

- The normal equation matrix (N) is symmetrical about the principal diagonal.

- The upper left hand corner the N matrix consists of an 18*18 submatrix corresponding to coefficients of satellite position's polynomial.
- The lower right hand corner of the N matrix consists of 3*3 submartrices along the principal diagonal with each submatrix corresponding to ground coordinates of each point, all the other elements outside of these submatrices being zero.
- The observation equations for ground control lead to the inclusion of $W_{2i}$ in the N matrix and $W_{2i}C_{2i}$ in the T matrix.
- The satellite position equations lead to the inclusion of $W_3$ and $W_3C_3$ in the normal equation.

## 4.9. The reduced normal equations

The normal equations 4.41 can be written in the form of two matrix equations as follows:

$$\overset{oo}{N}\overset{\bullet\bullet}{\Delta}+\bar{N}^{t}\overset{\bullet}{\Delta}=\overset{oo}{T} \tag{4.43}$$

$$\bar{N}\overset{\bullet\bullet}{\Delta}+\overset{\bar{o}}{N}\overset{\bullet}{\Delta}=\overset{o}{T} \tag{4.44}$$

where $\overset{\bar{o}}{N}=\overset{o}{N}+W_2$

Solving for $\overset{\bullet}{\Delta}$ in equation 4.43 results

$$\overset{\bullet}{\Delta}=\overset{\bar{o}}{N}^{-1}(\overset{o}{T}-\bar{N}\overset{\bullet\bullet}{\Delta}) \tag{4.45}$$

Substituting equation 4.45 into 4.44

$$\overset{oo}{N}\overset{\bullet\bullet}{\Delta}+\bar{N}^{t}[\overset{\bar{o}}{N}^{-1}(\overset{o}{T}-\bar{N}\overset{\bullet\bullet}{\Delta})]=\overset{oo}{T} \tag{4.46}$$

i.e.

$$(\overset{oo}{N}-\bar{N}^{t}\overset{\bar{o}}{N}^{-1}\bar{N})\overset{\bullet\bullet}{\Delta}=\overset{oo}{T}-\bar{N}^{t}\overset{\bar{o}}{N}^{-1}\overset{o}{T} \tag{4.47}$$

Which is referred to as the reduced normal equation (RNE) and may be expressed by

$$S\ddot{\Delta} = E \tag{4.48}$$

In which

$$S = \ddot{N} - \bar{N}^{t}\,\mathring{N}^{-1}\,\bar{N} \tag{4.49}$$

and

$$E = \ddot{T} - \bar{N}^{t}\,\bar{N}^{-1}\,\mathring{T} \tag{4.50}$$

Equations 4.49 and 4.50 can be decomposed into independent equations for each ground point:

$$S = \sum_{i=1}^{n} S_i + W_3 \tag{4.51}$$

$$E = \sum_{i=1}^{n} E_i - W_3 C_3 \tag{4.52}$$

In which

$$S_i = \ddot{N}_i - \bar{N}_i^{t}\,(\mathring{N}_i + W_{2i})^{-1}\,\bar{N}_i \tag{4.53}$$

$$E_i = \ddot{T}_i - \bar{N}_i^{t}\,(\mathring{N}_i + W_{2i})^{-1}\,\mathring{T}_i \tag{4.54}$$

And similarly equation 4.45 can be expressed as independent equations as follows.

$$\dot{\Delta}_i = (\mathring{N}_i + W_{2i})^{-1}(\dot{B}_i^{t}\,W_{1i}C_{1i} - W_{2i}C_{2i} - \bar{N}_i\,\ddot{\Delta}) \tag{4.55}$$

for i = 1, n

After having solved for $\ddot{\Delta}$ using equation 4.48, the corrections to the ground coordinates of ground control points can be computed point by point from equation 4.55. It can be observed from equations 4.48 and 4.55 that the largest set of

simultaneous equations to be solved is 18, which is the number of parameters of the polynomials of the satellite positions.

Figure 4.2 shows a general flow chart of the computation process. After data input, observation equations are computed one by one and their contributions are accumulated into the S and E matrices of the normal equations.

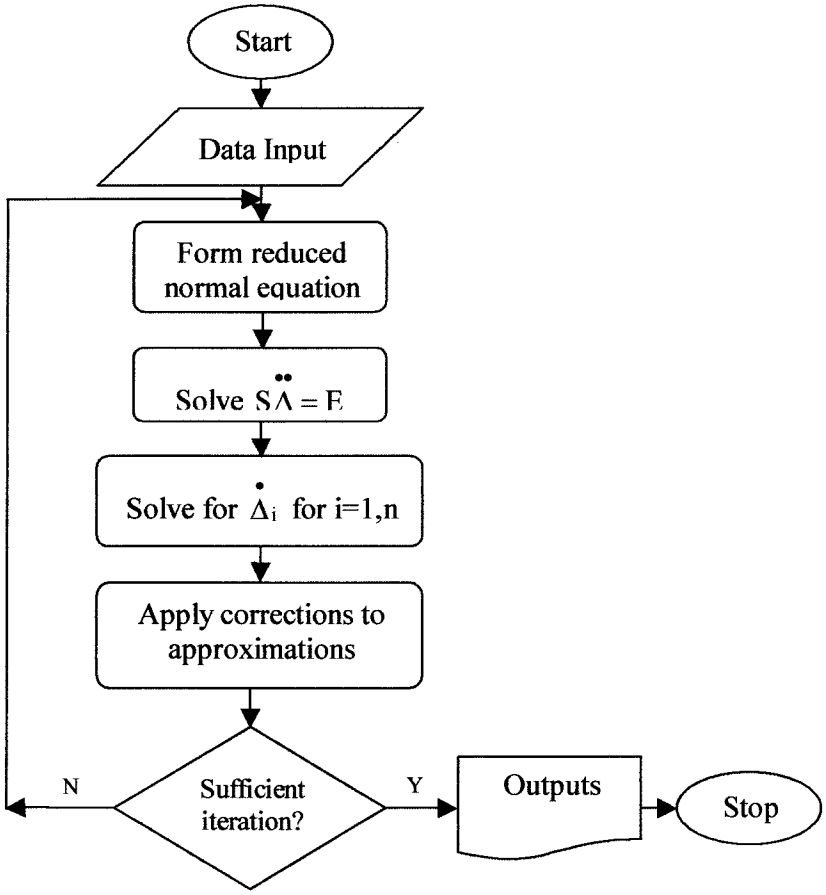


**Figure 4.2 General flow chart of solution of RNE.**

The solution to the reduced normal equations gives an estimated correction ($\ddot{\Delta}$) to the coefficients polynomials of satellite position. The corrections to the ground coordinates

$(\Delta X_i, \Delta Y_i, \Delta Z_i)$ are next computed using equation 4.55. The computed corrections are then applied to the approximate values of the unknown parameters:

$$\begin{aligned}
\overset{\circ}{a}_{1x} &= \overset{\circ}{a}_{1x} + \Delta a_{1x} \\
\overset{\circ}{b}_{1x} &= \overset{\circ}{b}_{1x} + \Delta b_{1x} \\
&\cdots\cdots\cdots\cdots \\
\overset{\circ}{c}_{2z} &= \overset{\circ}{c}_{2z} + \Delta c_{2z}
\end{aligned} \tag{4.56}$$

and

$$\begin{aligned}
\overset{\circ}{X}_i &= \overset{\circ}{X}_i + \Delta X_i \\
\overset{\circ}{Y}_i &= \overset{\circ}{Y}_i + \Delta Y_i \\
\overset{\circ}{Z}_i &= \overset{\circ}{Z}_i + \Delta Z_i
\end{aligned} \tag{4.57}$$

These newly corrected approximations are used as new approximations and the complete solution is repeated in a second iteration. The iteration procedure is repeated until the prescribed criteria for iteration termination is satisfied.

## 4.10. Summary

For elevations derived using InSAR, accurate orbit data should be known. The current accuracy of orbit determination is not sufficient to obtain absolute heights of ground points and thus ground control data is necessary to reduce errors to an acceptable level. The model developed allows calculation of absolute terrain elevation by incorporating ground control points. The computation procedure is based on stereo radargrammetric mapping of overlapping SAR images, incorporating an expression for elevation based on the fringe information. The model used polynomials for orbital satellites' positions. The results of the computation will be given in the next chapter.

# *Chapter Five*

# Experiments and Results

## 5.1 Introduction

In the previous chapter a model has been developed to obtain terrain elevations, which incorporates ground control and orbital data. To test of the model, a pair of ERS tandem mission data over west of Sydney, Australia was used. The data was prepared and processed in Australian Centre for Remote Sensing (ACRES). This chapter will discuss the research procedure and results of this study. The procedure consisted of following steps:

- Selecting the study area.
- Selecting the image data.
- Geometric registration of data and production of an interferogram.
- Phase unwrapping.
- Ground control points identification.
- Orbit determination.
- Conversion of the coordinates of the whole data into a unique coordinate system.
- Simultaneous solution of the orbital coefficients, positions and heights of GCPs, and range and phase measurements of the points.

## 5.2 Study area

The selected test site is at Prospect about 30 Km west of Sydney and includes urban areas, Prospect Reservoir, and also the Great Western Freeway. The selected area is undulating with terrain elevations varying from 10 to 100 m. This range of elevations avoided fringe discontinuities occurring due to layover. However, it was also necessary to include the area to the west of Prospect, comprising mainly the forested Blue

Mountains and the Nepean River. This was necessary because the original selected study area was too small for the Vexcel software, which was used to process the data, since it fails in the image coregistration step when the images are too small. This area was chosen for two reason: firstly, the high possibility of availability of data, and secondly, the availibity of orthophoto maps (scale 1:10000) of the region with a contour distance of 4m. The figure 5.1 shows a map of Prospect area.

## 5.3 ERS SAR Tandem data

Although the orbit maintenance and measurement strategy of ERS platforms enable them to be exploited for generation of interferometric SAR data sets, the ERS orbit configuration was designed before interferometry was considered as an operational technique. Hence it is not ideally suited to the production of interferometric data sets, particularly because of the 35 days repeat cycle of ERS-1. This causes insufficient coherence between successive SAR acquisitions, which in many cases, disallows the generation of interferograms. The launch of ERS2, however, changed the situation significantly. The operation of two platforms simultaneously in tandem, can reduce the time between data acquisitions of the two passes, thus ensuring adequate correlation between successive SAR scenes, while maintaining each platform in an orbit configuration that ensures a maximum possible coverage of the Earth's surface. In April 1995, the ESA Council approved the ERS Tandem Mission for an operation over a period of 9 months following the ERS-2 Commissioning Phase. Pairs of ERS-1 and ERS-2 SAR images with an offset of one day have been acquired over large parts of the global land surfaces, enabling scientists to derive medium to high resolution DEMs for various applications.

The two satellites have been maintained approximately in the same orbital plane, ERS-2 following ERS-1. Thus the same swath on the ground is acquired by ERS-2 one day after ERS-1. By coordination of the global network of receiving stations, a background acquisition plan was set up within the constraints of satellite resources and the period of availability of the station for specific orbit maintenance procedures (ESA Web, 1998).

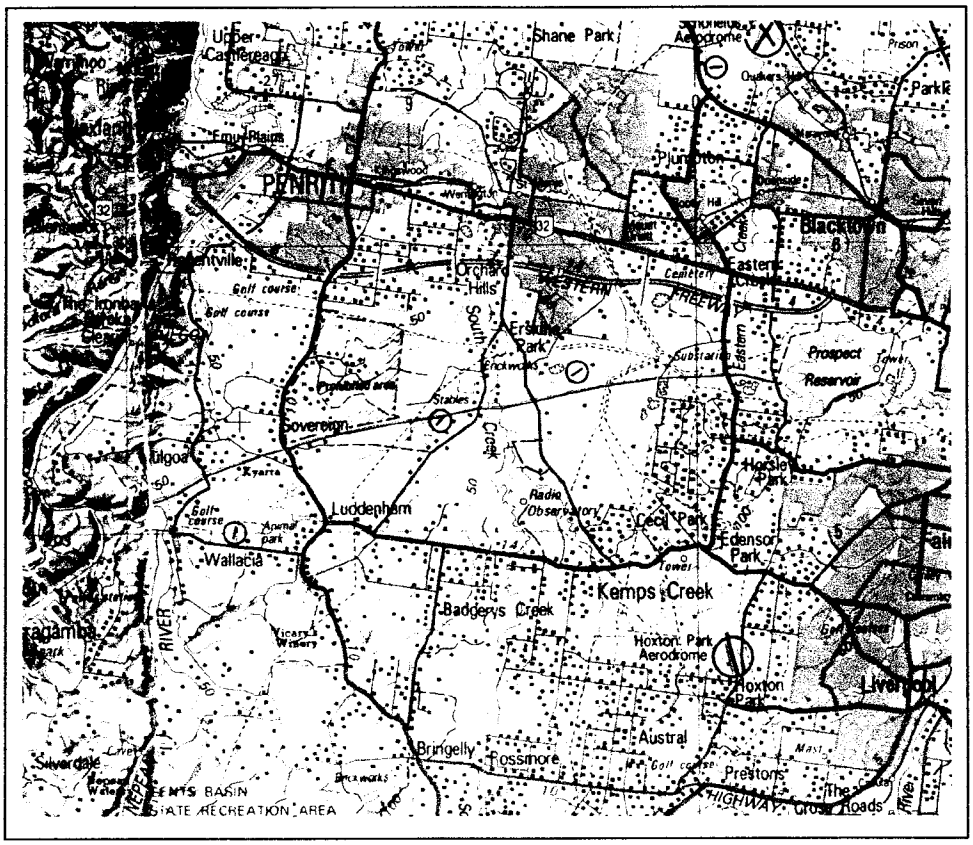


**Figure 5.1: Prospect study area (1:250000). Prospect Reservoir, Great Western Freeway and Nepean River in the west are observed.**

For example in period 15-January to 25-March (Polar Campaign) the orbit was maintained to meet baseline requirements (cross- track separation of 70 –170m) at latitudes above 60 degrees, while orbit cross over points were at equatorial latitudes. During this period maximum acquisition was scheduled over the stations of O'Higgins, McMurdo, Syowa, Alaska, Prince Albert and Kiruna. In contrast, while the orbit maintenance was focused on meeting a 50 –200 meters cross track separation at the equator, full coverage of South America has been acquired in April / May.

The current Tandem acquisition status of ERS-1/ERS-2 is shown in tables 5.1 and 5.2. They show the acquisitions with perpendicular baseline component of between 50m and 300 m, which are of particular interest for InSAR applications (ESA Web Site, 1998).

| **Baseline range** | **Number of frames pairs** | **% of total** |
|---|---|---|
| $B_{perp} < 50$ m | 22181 | 20 |
| 50 m$< B_{perp} <$ 300 m | 81619 | 73 |
| 300 m $< B_{perp} <$ 600 m | 6221 | 6 |
| 600 m$< B_{perp}$ | 1028 | 1 |

**Table 5.1: Tandem acquisition statistics**

| **Baseline range** | **Number of frames pairs** | **% of total** |
|---|---|---|
| 50 m$< B_{perp} <$ 130 m | 45681 | 41 |
| 130 m $< B_{perp} <$ 215 m | 26637 | 24 |
| 215 m $< B_{perp} <$ 300 m | 9301 | 8 |

**Table 5.2: Tandem acquisition with baseline values between 50m and 300m**

## 5.4 Study data

Using ESA web site, the data over the selected area has been investigated. Tables 5.3 and 5.4 and figure 5.2 show the characteristics and the coverage area of these data. With regard to values of the baseline component perpendicular to the line of sight of the data ($B_{perp}$), two sets of data over area number 5 have been chosen for experiments. Unfortunately the data set ERS1 orbit No. 23436 and ERS2 orbit No. 3763 were not available in Australian Centre for Remote Sensing (ACRES). Hence it was decided to continue with the only one available set of data ERS1 orbit No. 22935 and ERS2 orbit No. 3262, acquired on 3rd and 4$^{th}$ December 1995, respectively. Figure 5.3 shows ERS-1 image of the study area..

The data is an image pair with a relatively small baseline (147 m) and one day interval between data acquisitions. Under these conditions high interferometric correlation values are expected. However, Figure 5.17 shows that water surfaces resulted in low interferometric correlation due to both temporal change and low signal to noise ratio.

| AREA | ORBIT | TRACK | FRAME | DATE | TIME | $B_{PAR}$ | $B_{PERP}$ |
|---|---|---|---|---|---|---|---|
| 1 | 22642 | 109 | 6507 | 13/11/95 | 13:04 | -541 | -1042 |
| 2 | 22706 | 173 | 4275 | 17/11/95 | 23:52 | 223 | 484 |
| 3 | 22706 | 173 | 4293 | 17/11/95 | 23:52 | 221 | 479 |
| 4 | 22935 | 402 | 4275 | 03/12/95 | 23:49 | 58 | 147 |
| 5 | 22935 | 402 | 4293 | 03/12/95 | 23:49 | 58 | 146 |
| 2 | 23207 | 173 | 4275 | 22/12/65 | 23:52 | 148 | 371 |
| 3 | 23207 | 173 | 4293 | 22/12/95 | 23:52 | 147 | 369 |
| 4 | 23436 | 402 | 4275 | 07/01/96 | 23:49 | 94 | 216 |
| 5 | 23436 | 402 | 4293 | 07/01/96 | 23:49 | 94 | 215 |

**Table 5.3: ERS1 mission over Sydney**

| AREA | ORBIT | TRACK | FRAME | DATE | TIME |
|---|---|---|---|---|---|
| 1 | 2969 | 109 | 6507 | 14/11/95 | 13:04 |
| 2 | 3033 | 173 | 4275 | 18/11/95 | 23:52 |
| 3 | 3033 | 173 | 4293 | 18/11/95 | 23:52 |
| 4 | 3262 | 402 | 4275 | 04/12/95 | 23:49 |
| 5 | 3262 | 402 | 4293 | 04/12/95 | 23:49 |
| 2 | 3534 | 173 | 4275 | 23/12/95 | 23:52 |
| 3 | 3534 | 173 | 4293 | 23/12/95 | 23:52 |
| 4 | 3763 | 402 | 4275 | 08/01/96 | 23:49 |
| 5 | 3763 | 402 | 4293 | 08/01/96 | 23:49 |

**Table 5.4: ERS2 mission over Sydney**

Hence, except for windy conditions, the backscatter intensities over the water remain very low. Forest stands show low correlation due to volume scattering combined with temporal decorrelation. Intermediate to high interferometric correlation can be observed over urban and industry areas where there are buildings which contribute to a high interferometric correlation.

## 5.5 InSAR Processing

To process the data the Vexcel 3D SAR Processing Software (SARPS) installed in Australian Centre for Remote Sensing (ACRES) has been used. The software includes level zero processing, SAR processing, SAR orthorectification, interferometric SAR processing and differential interferometry processing.

The data was ingested on the workstation disk, where each set of image data includes two data files, the image data and the header file. The header file which is 20 Kb in size includes information about the image data. The processing started with a subset of a

quadrant consisting of 13744 single-look azimuth pixels by 4912 single-look slant range pixels. Figure 5.4 and 5.5 show the header files for the subsets of the data.

Registration is done in the software by using a 2D correlation technique in two steps. The first finds rough offsets of the two images (delta range and delta azimuth), and the second finds local offsets on a user defined grid throughout the image. These offset are used to fit a first order affine transform data relating the two images. The next step of the processing is the phase unwrapping, which uses the same algorithms described by Goldstein et al. (1988) (section 2.9.3) based on a path following algorithm, that uses branch cuts to guide the unwrapping.

## 5.6 Ground Control Points (GCPs)

Selecting the collect GCPs mode in Vexcel software displays the interferogram intensities. Clicking the points indicates line and pixel numbers of GCPs, which are points in the image that can be identified on the maps. Identifying such points was quite difficult, due to the poor condition of displaying interferogram intensity. However, 41 GCPs were selected as far as possible to cover the extent of the image portions under study and in high correlation areas.

The ground coordinates of the control points were derived from the orthophoto maps. Assuming standard map accuracy, a well-defined points in these maps will have a planimetric accuracy standard deviation of 0.5 mm at publication scale and a height accuracy of half the contour interval (4 m). The standard deviations of the coordinates of these points can thus be estimated to be 5m in planimetry and 1.3m in height.

The coordinates of the maps and orthophotos are based on the Australian Map Grid (AMG) (E, N) and Australian Height Datum (AHD) coordinates, which is based on the Australian Geodetic Datum (AGD). For consistency the whole data (ERS data and GCPs) and to simplify of computation, the data has been transformed to a local plane coordinate system, which is a local tangent plane to the spheroid at a particular point. In

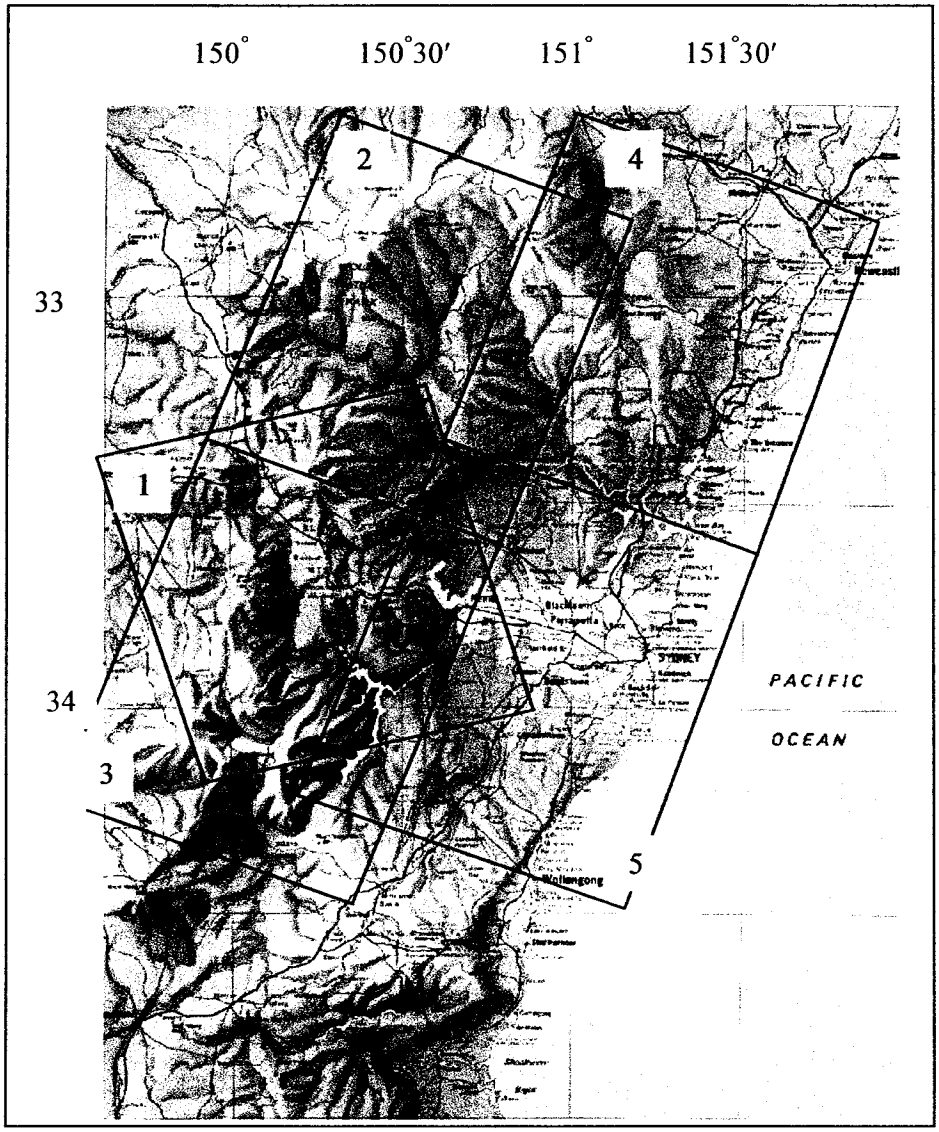


**Figure 5.2: Coverage of ERS-1 and ERS-2 data.**

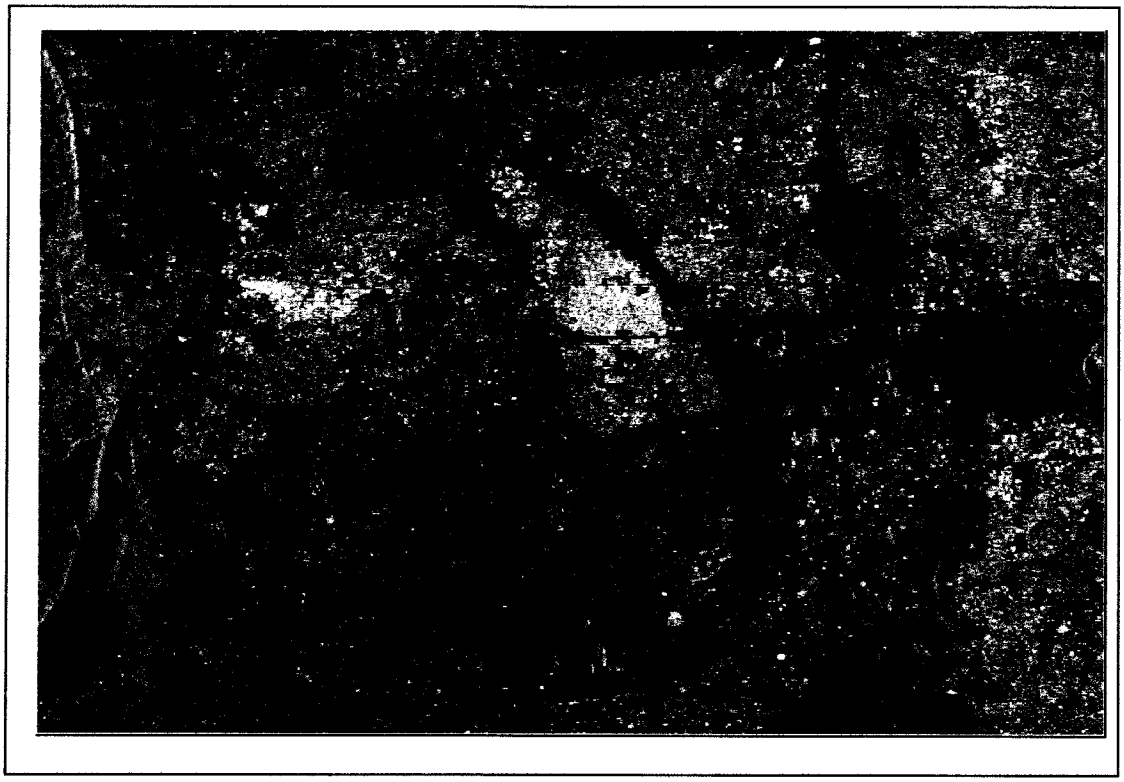

**Figure 5.3: ERS-1 image of the study area. Urban areas are bright, Prospect Reservoir and Nepean River are dark, the Great Western Freeway is visible in the middle of the image.**

```
title:                  SAR
date:                   19951203234
raw_data_start_time:    23 49 35.8033
polarization:           VV
scene_center_latitude:          -33.7810   decimal degrees
scene_center_longitude:         150.7064   decimal degrees
track_angle:                    -164.9527   degrees
platform_altitude:              797318.2254   m
terrain_height:                 0.0000   m
sensor_position_vector:         0.000000      0.000000 797318.225396   m     m     m
sensor_velocity_vector:         7150.780376     0.000000      0.000000   m/s   m/s   m/s
sensor_acceleration_vector:     0.000000      0.000000      0.000000   m/s^2 m/s^2 m/s^2
pulse_repetition_frequency:     1659.663940   Hz
doppler_polynomial:             -9.26719e+02  1.06989e-03 -1.80042e-09  5.90800e-15   Hz Hz/m
Hz/m^2 Hz/m^3
echo_time_delay:                5.615017e-03   s
near_range_raw:                 841669.8741   m
center_range_raw:               863865.7424   m
far_range_raw:                  886061.6107   m
range_pixel_spacing:            7.90591925   m
range_looks:                    1
azimuth_looks:                  1
azimuth_offset:                 6.95141   s
azimuth_pixel_spacing:          4.05706   m
range_pixels:                   4912
azimuth_pixels:                 13744

number_of_state_vectors:        5
time_of_first_state_vector:     85680.00000   s
state_vector_interval:          60.00000   s
state_vector_position_1: -5763438.4470   2577719.4330   -3394518.9900   m   m   m
state_vector_velocity_1:    3874.0038     150.1682     -6474.2446   m/s m/s m/s
state_vector_position_2: -5519962.3430   2580681.4510   -3776095.7480   m   m   m
state_vector_velocity_2:    4238.9218     -51.9853     -6240.8604   m/s m/s m/s
state_vector_position_3: -5255135.2720   2571424.5330   -4142937.4580   m   m   m
state_vector_velocity_3:    4585.4707     -256.9710     -5983.2403   m/s m/s m/s
state_vector_position_4: -4970100.2640   2549807.4890   -4493620.4080   m   m   m
state_vector_velocity_4:    4912.3023     -463.8278     -5702.4145   m/s m/s m/s
state_vector_position_5: -4666078.5900   2515747.3080   -4826785.3750   m   m   m
state_vector_velocity_5:    5218.1574     -671.5783     -5399.5006   m/s m/s m/s
sensor_name: ERS1

********** END OF PROCESSING PARAMETERS **********
```

**Figure 5.4:ERS-1 header data file.**

```
title:                  SAR
date:                   19951204234
raw_data_start_time:    23 49 38.1170
polarization:           VV
scene_center_latitude:          -33.7694   decimal degrees
scene_center_longitude:         150.7462   decimal degrees
track_angle:                    -164.9779  degrees
platform_altitude:              797558.5171  m
terrain_height:                 0.0000  m
sensor_position_vector:         0.000000      0.000000  797558.517139  m    m    m
sensor_velocity_vector:         7117.951363   0.000000      0.000000  m/s  m/s  m/s
sensor_acceleration_vector:     0.000000      0.000000      0.000000  m/s^2 m/s^2 m/s^2
pulse_repetition_frequency:     1659.903556  Hz
doppler_polynomial:     -1.19353e+03  6.12979e-04  1.34055e-09 -1.91067e-14  Hz Hz/m
Hz/m^2 Hz/m^3
echo_time_delay:                5.606270e-03  s
near_range_raw:                 840358.7318  m
center_range_raw:               862554.6001  m
far_range_raw:                  884750.4683  m
range_pixel_spacing:            7.90591925  m
range_looks:                    1
azimuth_looks:                  1
azimuth_offset:                 6.95040  s
azimuth_pixel_spacing:          4.05628  m
range_pixels:                   4912
azimuth_pixels:                 13744

number_of_state_vectors:        5
time_of_first_state_vector:     85680.00000  s
state_vector_interval:          60.00000  s
state_vector_position_1: -5773201.8990   2577181.5110  -3378278.1560  m  m  m
state_vector_velocity_1:    3858.3562     158.5911     -6483.4551  m/s m/s m/s
state_vector_position_2: -5530642.7070   2580653.5680  -3760438.7620  m  m  m
state_vector_velocity_2:    4224.0157     -43.4134     -6251.1049  m/s m/s m/s
state_vector_position_3: -5266686.2900   2571914.4330  -4127925.1420  m  m  m
state_vector_velocity_3:    4571.3645     -248.2902    -5994.4777  m/s m/s m/s
state_vector_position_4: -4982472.2810   2550820.4860  -4479311.0120  m  m  m
state_vector_velocity_4:    4899.0507     -455.0789    -5714.5999  m/s m/s m/s
state_vector_position_5: -4679218.7790   2517286.2470  -4813234.3450  m  m  m
state_vector_velocity_5:    5205.8115     -662.8028    -5412.5857  m/s m/s m/s
sensor_name: ERS2

********** END OF PROCESSING PARAMETERS **********
```

**Figure 5.5: ERS-2 header data file.**

this case the point is approximately coincident with geographic centre of the study area. The different terrain coordinate systems have been discussed briefly in appendix 1.

Transformation of GCPs from AMG (E, N) to AGD ($\varphi,\lambda$) is accomplished using Redfern's formula (1968). Then AGD (x, y, z) geocentric coordinate were computed from AGD latitude and longitude and rescaled heights as an estimate of AGD ellipsoidal height. Setting up the transformation parameters for geocentric to local plane was the next step. Finally the AGD (x, y, z) was transformed to a local plane coordinates. Figure 5.6 illustrated the diagram of conversion of data from AMG to a local coordinate and table 5.5 shows the GCPs in both geographic and local system coordinates.

## 5.7 Ephemeris data

The header data files, which include ephemeris data for 5 points at intervals of one minute, consist of the geocentric X, Y, and Z satellite coordinates in kilometres (statevectors), based on the Earth Centred Earth Fixed (ECEF) WGS84 reference and the corresponding time. Figures 5.7-8 (a-c) show graphically the ephemeris data for the pair of ERS-1 and ERS-2 images. These figures relate to whole frame data and only a very small distance (about 3 seconds) of the data is used in this study, which is shown as thick lines on the figures.

Therefore the interpolation of the actual ephemeris data for each pixel will be approximately only and hence simple polynomials will be adequate for this purpose.The ephemeris data can be used to compute the approximate orbital positions of the sensor platforms. Two problems must be considered. Firstly, an expression must be found to relate the satellite's position to the image distance (time of acquisition of each pixel). Secondly, the satellite's coordinates are given in WGS84 geocentric coordinate system; therefore, as described before, they have to be converted to the local coordinate system that is used in solution.

As described in section 4.2 the image distance (line number) can be related to time of acquisition of that line by equation 4.5

$$T_P = T_0 + T_{off} + i / PRF \qquad (4.5)$$

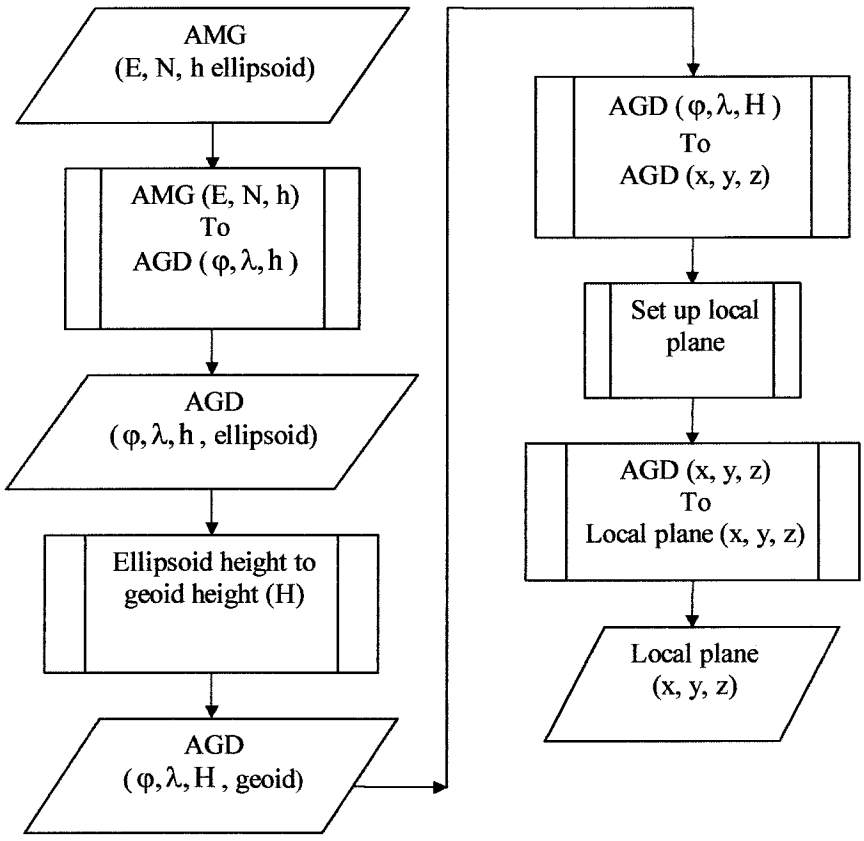


**Figure 5.6: The process AMG (E, N, h) to local (x, y, z)**

| GCP NO | E (M) | N (M) | H (M) | XLOC (M) | YLOC (M) | ZLOC (M) |
|---|---|---|---|---|---|---|
| 1 | 307000 | 6257625 | 80 | 19317.86 | -2567.08 | 65.76 |
| 2 | 296937.5 | 6258625 | 50 | 9280.80 | -1343.29 | 58.61 |
| 3 | 309100 | 6256325 | 63 | 21388.23 | -3913.47 | 41.47 |
| 4 | 294175 | 6252125 | 40 | 6374.42 | -7779.42 | 47.56 |
| 5 | 307400 | 6250975 | 57 | 19569.43 | -9224.02 | 35.82 |
| 6 | 308350 | 6259162 | 50 | 20701.60 | -1060.58 | 31.85 |
| 7 | 308737.5 | 6249338 | 10 | 20869.85 | -10890.29 | -17.94 |
| 8 | 287462.5 | 6259250 | 60 | -176.77 | -507.55 | 75.48 |
| 9 | 288812.5 | 6262125 | 50 | 1236.69 | 2336.28 | 64.95 |
| 10 | 285262.5 | 6263350 | 20 | -2284.65 | 3639.75 | 34.05 |
| 11 | 289187.5 | 6266788 | 50 | 1715.23 | 6989.14 | 61.43 |
| 12 | 309787.5 | 6255850 | 60 | 22064.93 | -4403.65 | 35.85 |
| 13 | 307250 | 6258862 | 68 | 19595.30 | -1336 | 53.29 |
| 14 | 305275 | 6262212 | 40 | 17695.39 | 2056.95 | 30.65 |
| 15 | 308500 | 6262938 | 76 | 20935.68 | 2711 | 56.60 |
| 16 | 310825 | 6261775 | 44 | 23234.02 | 1496.58 | 17.05 |
| 17 | 310500 | 6262538 | 84 | 22926.23 | 2266.61 | 57.93 |
| 18 | 304687.5 | 6247525 | 48 | 16780.74 | -12612.43 | 28.93 |
| 19 | 303950 | 6248025 | 44 | 16054.62 | -12096.12 | 27.80 |
| 20 | 295250 | 6259025 | 52 | 7602.80 | -905.85 | 62.91 |
| 21 | 294950 | 6260612 | 50 | 7338.24 | 687.26 | 61.25 |
| 22 | 294387.5 | 6261725 | 47 | 6800.70 | 1812.38 | 58.62 |
| 23 | 297537.5 | 6259975 | 45 | 9910.64 | -7.11 | 52.81 |
| 24 | 298262.5 | 6260375 | 52 | 10644.31 | 376.61 | 58.62 |
| 25 | 297712.5 | 6261150 | 50 | 10111.74 | 1163.59 | 57.39 |
| 26 | 297575 | 6262838 | 52 | 10011.85 | 2854.07 | 59.01 |
| 27 | 299687.5 | 6261688 | 64 | 12098.07 | 1657.46 | 67.82 |
| 28 | 299800 | 6262238 | 55 | 12222.76 | 2204.77 | 58.42 |
| 29 | 286337.5 | 6260875 | 44 | -1265.15 | 1141.85 | 59.27 |
| 30 | 286875 | 6261462 | 40 | -714.8 | 1716.65 | 55.23 |
| 31 | 287487.5 | 6260250 | 52 | -129.52 | 491.5 | 67.48 |
| 32 | 282537.5 | 6262438 | 32 | -5028.8 | 2788.75 | 44.91 |
| 33 | 288775 | 6263312 | 54 | 1225.61 | 3523.66 | 68.41 |
| 34 | 290125 | 6263750 | 40 | 2584.83 | 3931.45 | 53.76 |
| 35 | 294635 | 6266275 | 28 | 7149.28 | 6355.23 | 36.32 |
| 36 | 294730 | 6264265 | 28 | 7199.56 | 4343.84 | 37.96 |
| 37 | 295885 | 6263020 | 28 | 8326.46 | 3073.6 | 37.33 |
| 38 | 294987.5 | 6261900 | 40 | 7404.37 | 1973.97 | 50.90 |
| 39 | 308487.5 | 6251688 | 40 | 20672.46 | -8535.46 | 16.30 |
| 40 | 306775 | 6252738 | 37 | 18983.88 | -7447.58 | 19.91 |
| 41 | 307875 | 6248625 | 30 | 19991.76 | -11583.87 | 3.64 |

**Table 5.5: Ground control points in geographic and local plane coordinate systems.**

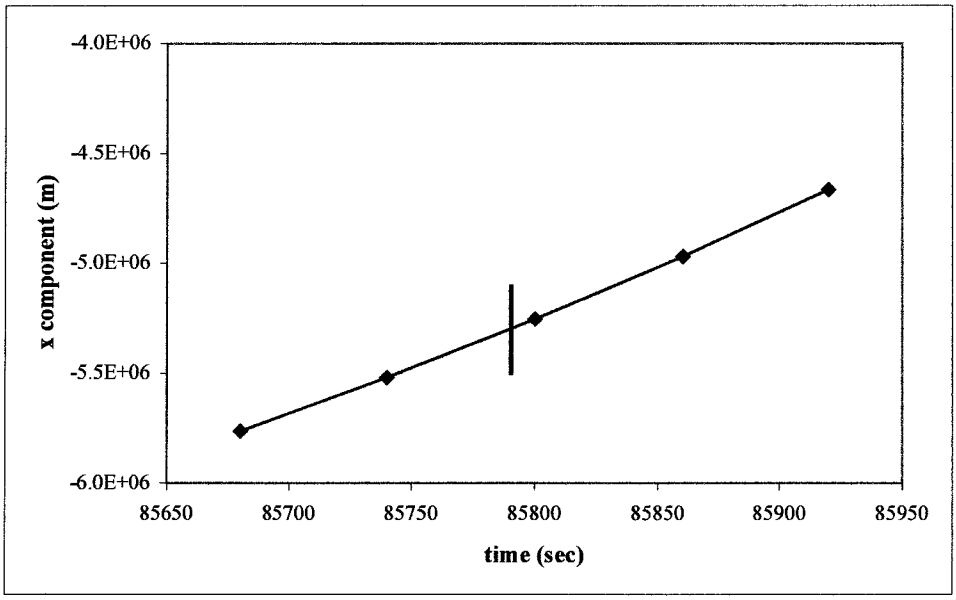


**Figure 5.7(a): Ephemeris ERS-1 Data – Geocentric X coordinates**

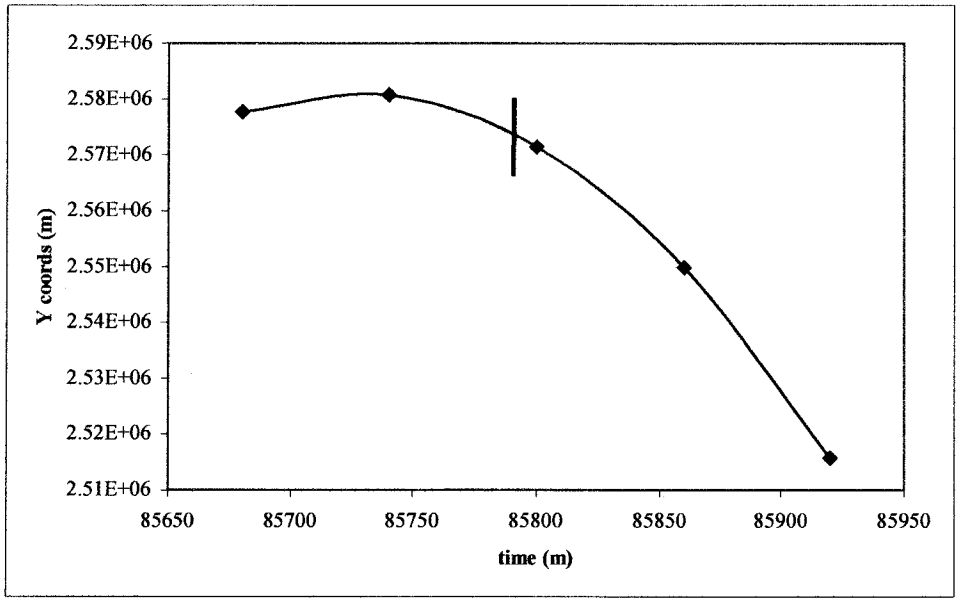


**Figure 5.7(b): Ephemeris ERS-1 Data – Geocentric Y coordinates**

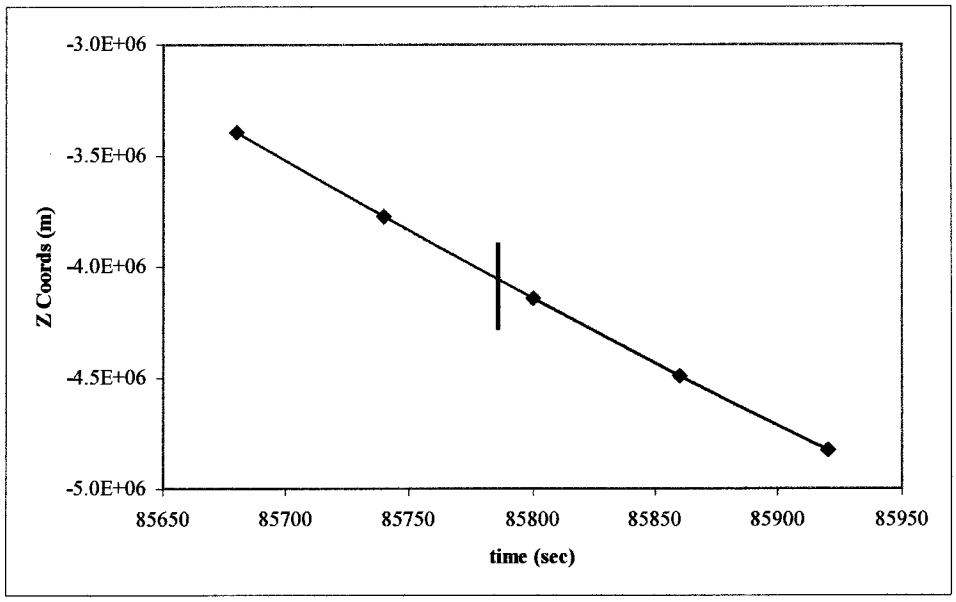


**Figure 5.7(c): Ephemeris ERS-1 Data – Geocentric Z coordinates**

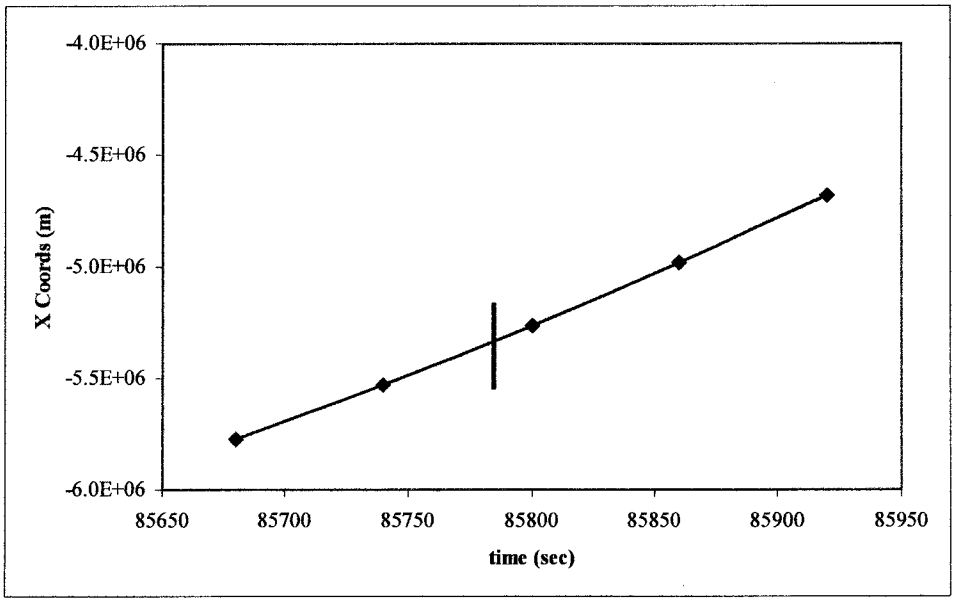


**Figure 5.8(a): Ephemeris ERS-2 Data – Geocentric X coordinates**

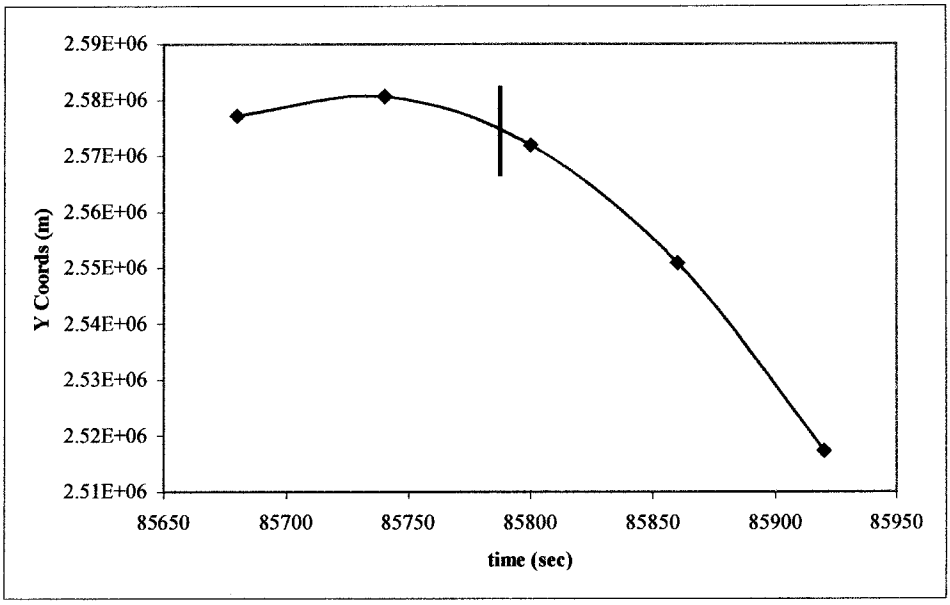


**Figure 5.8(b): Ephemeris ERS-2 Data – Geocentric Y coordinates**

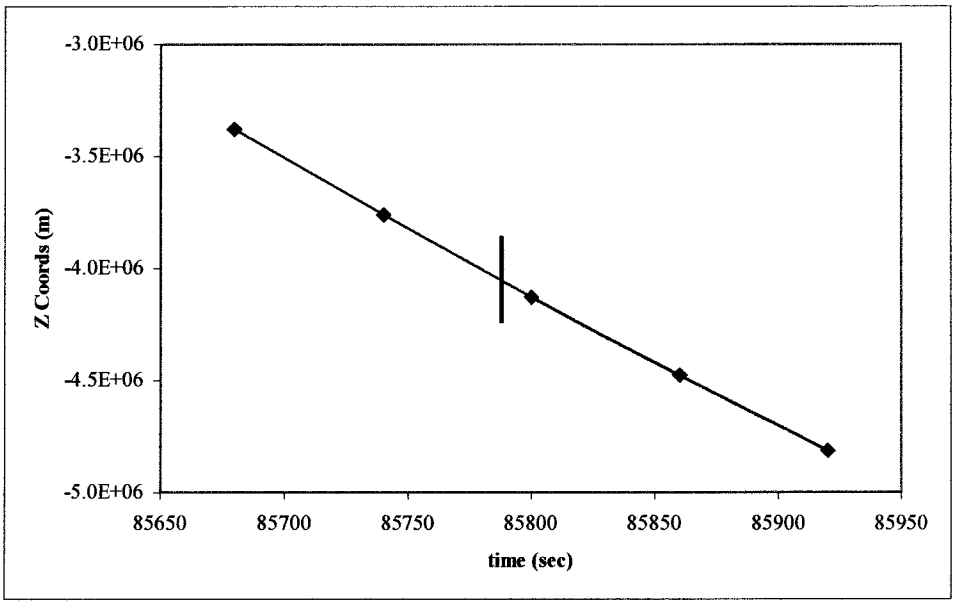


**Figure 5.8(c): Ephemeris ERS-2 Data – Geocentric Z coordinates**

The propagation of the satellite statevectors can be carried out by interpolation of the five ephemeris data parameters provided, using low order polynomials. Then for each image position (line number) the time of acquisition can be used to calculate the satellite's position from the polynomials.

Transformation from geocentric coordinates to the local space rectangular coordinates is as follows:

$$\begin{bmatrix} x_l \\ y_l \\ z_l \end{bmatrix} = R_{\varphi\lambda} \begin{bmatrix} x_G - x_0 \\ y_G - y_0 \\ z_G - z_0 \end{bmatrix} \tag{5.11}$$

Where $(x_l, y_l, z_l)$ and $(x_G, y_G, z_G)$ are the local rectangular and the geocentric coordinates of a given point, respectively, and $(x_0, y_0, z_0)$ are the geocentric coordinates of the origin of the local rectangular coordinate system. $R_{\varphi\lambda}$ is a rotation matrix, whose elements are a function of the latitude and longitude of the local origin $(\varphi_0, \lambda_0)$.

## 5.8 Least squares solution for the polynomials of x, y, z

For each set of converted ephemeris data consisting of the local coordinates of satellite's position x, y, and z in metres, three observation equations can be formed as it has been shown by equation 4.6:

$$\begin{aligned} x &= a_x T_p^2 + b_x T_p + c_x \\ y &= a_y T_p^2 + b_y T_p + c_y \\ z &= a_z T_p^2 + b_z T_p + c_z \end{aligned} \tag{5.12}$$

Where, $T_p$ is time of acquisition of point from the beginning of the frame and $a_x$, $b_x$, ..., $c_z$ are the polynomials' coefficients which are to be determined.

For five ephemeris records, there will be five sets of these observation equations, whose solution by a least squares program will determine the polynomial coefficients. Tables

5.6 and 5.7 give the coefficients of polynomials and their standard deviations for the two satellites. The computed standard deviations of the coefficients can be used as the 'a priori' standard deviation for the corresponding parameters in the adjustment program. The accuracy of the coefficients clearly depends on several factors including the accuracy of the satellite tracking.

| | a ($ms^{-2}$) | Std a ($ms^{-2}$) | b ($ms^{-1}$) | Std b ($ms^{-1}$) | Cc (m) | Std c (m) |
|---|---|---|---|---|---|---|
| X | -4.37E-02 | 2.12E-10 | 5.47E+03 | 1.82E-05 | -1.47E+08 | 1.56 |
| Y | 4.89E-02 | 2.12E-10 | -1.57E+04 | 1.82E-05 | 9.83E+08 | 1.56 |
| Z | 5.82E-04 | 2.12E-10 | -6.72E+06 | 1.82E-05 | 3.76E+01 | 1.56 |

**Table 5.6: Coefficients of polynomials and standard deviations (ERS 1)**

| | a ($ms^{-2}$) | Std a ($ms^{-2}$) | b ($ms^{-1}$) | Std b ($ms^{-1}$) | c (m) | Std c (m) |
|---|---|---|---|---|---|---|
| X | -4.14E-02 | 2.12E-10 | 5.08E+03 | 1.82E-05 | -1.31E+08 | 1.56 |
| Y | -2.26E-03 | 2.12E-10 | -6.88E+03 | 1.82E-05 | 6.06E+08 | 1.56 |
| Z | 5.06E-04 | 2.12E-10 | 7.05E+01 | 1.82E-05 | -8.99E+06 | 1.56 |

**Table 5.7: Coefficients of polynomials and standard deviations (ERS 2)**

## 5.9 Description of program

Figure 5.9 shows the flowchart of the main program to solve for the coordinates of the ground control by the formulas shown in Chapter 4. The ground coordinates of the points and polynomial coefficients derived in previous sections, are assumed as initial approximations of the unknowns. Observation data includes measured range to the observed points and the phase difference obtained from the phase unwrapping process. In the next step, time of acquisition of each point by using equation 4.5 is calculated for both images. Then the next step is to compute the satellite positions at the acquisition time of each line using equation 4.6 and the approximate values for polynomial coefficients, for the first iteration, and for later iterationsubsequently the newly derived approximations from the previous iteration.

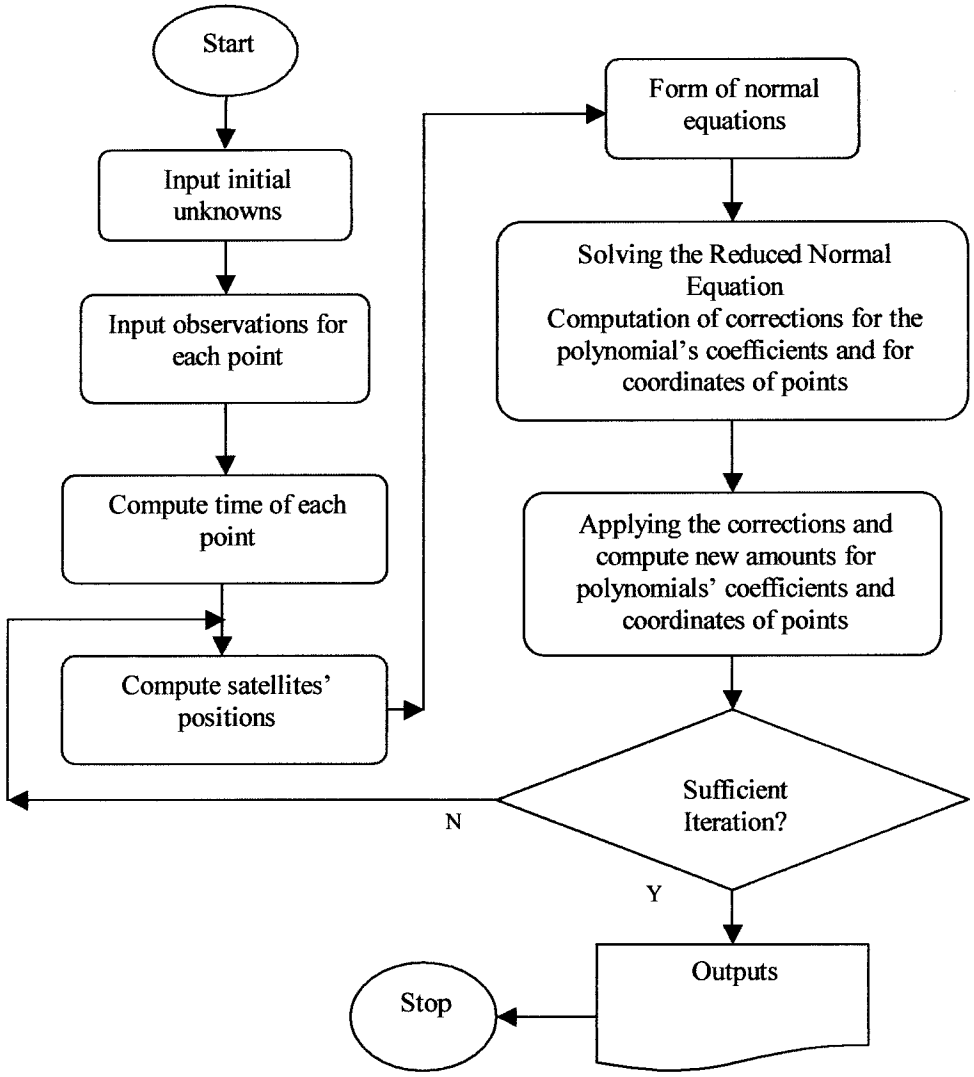


**Figure 5.9: General flowchart of the solution.**

For each observed point the elements of the matrices of Reduced Normal Equation (RNE) are computed. These elements are given by equations 4.4, 4.13 and 4.15. Then the reduced normal equations are formed according to the equations 4.53 and 4.54, from which the correction values for polynomial coefficients are computed according to equation 4.48. Then, the corrections to the ground points are computed using equation 4.50. After computing these corrections and apply them to the unknowns, the new

values of the unknowns are computed. The residuals of observations $v_{r1}, v_{r2}, v_{\varphi}$ are then computed. The RMS of the residuals are next computed. These values are then compared with previous RMS value in the test for convergency. The iteration process is terminated if the difference between the current RMS of the residuals and the previous RMS value is less than a prescribed value.

## 5.10 Results

Table 5.8 shows the residuals at the control points after the adjustment. The results show an overall RMS error of 6.3 m, 3m and 1.5m in planimetry components and height, respectively. The radargrammetry equations primarily affect the planimetry coordinates, and the InSAR equation influences the height accuracy of the points. The planimetry results are very satisfactory compared with the pixel size of the images given by header data files shown in figure 5.4 and 5.5 (range pixel spacing of 7.9 m and azimuth pixel spacing of 4 m). However, this estimated accuracy is only based on residuals on control points. It is higher for checkpoints as shown in table 5.11 when fewer than all points are used as control. Appendix 2 shows the results of the tests using a varying number of GCPs for the remaining checkpoints. Table 5.10 shows the RMS of the GCPs for these tests, and table 5.11 shows the RMS of residuals for the remaining checkpoints. The accuracy of the planimetry components and height tend to deteriorate as the number of GCPs reduces. However, it can be concluded from tables 5.10-11 that 12 to 15 GCPs are the recommended minimum number of points, resulting in a 5m to 6m accuracy in height. The results of planimetry components are still very satisfactory with 12 GCPs.

Table 5.8 and tables in appendix 2 show that the $\Delta X$ error component is often the largest followed by $\Delta Y$ error component. The sizes of the errors in each component are usually correlated ie. if the $\Delta X$ component is relatively large, then the two other components will also be relatively large. Figure 5.10 shows this correlation. GCP No. 7 has the worst error in $\Delta X$ and $\Delta Z$, and point No. 19 has the worst error in $\Delta Y$. Figures 5.11-16 show the different error components versus azimuth and range positions of each

point. There is no correlation between the position of the point and these errors ie. the errors are not affected by increasing or decreasing the range or azimuth of the points. However, because the look angle of ERS is about $23^0$, for an individual point $\Delta X$ tends to be larger than $\Delta Z$.

Table 5.9 shows the residuals in the observation (satellite ranges and interferogram phase) and the phase coherence coefficients for each control points. The RMS residuals on satellite ranges are 3.3 m and 3.7 m, and RMS of phase residuals is 31.8 degree. Figure 5.17 shows the coherence map for the area. There are large decorrelated forest areas in the west of the image, which is expected considering the issues raised in section 3.3 regarding the causes of decorrelation. Furthermore decorrelated area over Prospect reservoir can be easily identified. Satisfactory coherence coefficients are obtained over urban areas.

The errors in the control coordinates are highly affected by phase coherence of the points as shown in figures 5.18-20. The figures generally show that the higher coherence level, the better estimation of point location. It can be observed that the errors of points with coherence levels of more than 0.65 are low compared with the points with poorer coherency. Figure 5.21, which shows the residuals of phase measurements versus coherence degree, also emphasises that these residuals are smaller for points with a high degree of coherency. Hence, it can be concluded that coherence is a very significant factor in interferometry SAR. Previously, the effect of coherence on the interferogram quality and phase measurement has been studied by Zebker et al (1992) and Small et al. (1995). Their results also showed that the accuracy of phase measurement and therefore height accuracy depends strongly on level of coherency.

Although, the results shown by this study are very satisfactory on this set of data, it is believed that the test of the algorithms requires additional data sets to confirm them. The geometry of the system used in this study is only suitable for InSAR techniques and is far from ideal for the radargrammetry techniques, which requires longer baseline

| Point No. | ΔX (m) | ΔY (m) | ΔZ (m) |
|---|---|---|---|
| 1 | -3.93 | -3.66 | -0.52 |
| 2 | -13.97 | 4.75 | -3.22 |
| 3 | 1.65 | -3.66 | 0.67 |
| 4 | 1.33 | 1.25 | 0.14 |
| 5 | -4.05 | 3.36 | -1.17 |
| 6 | -0.33 | 1.21 | -0.19 |
| 7 | -16.13 | 5.87 | -3.90 |
| 8 | 2.45 | 0.39 | 0.43 |
| 9 | 11.13 | -2.96 | 2.42 |
| 10 | -1.65 | -4.76 | 0.04 |
| 11 | 4.93 | 1.67 | 0.76 |
| 12 | 0.40 | -1.11 | 0.19 |
| 13 | -0.93 | 1.17 | -0.31 |
| 14 | 2.10 | 0.29 | 0.39 |
| 15 | 2.03 | -4.43 | 0.81 |
| 16 | 7.14 | -4.18 | 1.86 |
| 17 | 3.61 | -5.13 | 1.21 |
| 18 | -1.68 | 4.23 | -0.80 |
| 19 | -11.01 | 6.26 | -2.86 |
| 20 | -13.30 | 4.48 | -3.04 |
| 21 | 8.69 | -2.03 | 1.89 |
| 22 | -1.34 | 1.43 | -0.40 |
| 23 | 7.74 | -1.68 | 1.68 |
| 24 | 2.52 | -4.08 | 0.86 |
| 25 | -1.65 | 1.53 | -0.47 |
| 26 | 4.81 | -3.11 | 1.24 |
| 27 | 4.81 | -0.66 | 1.01 |
| 28 | 5.18 | -3.27 | 1.34 |
| 29 | -8.24 | 4.80 | -2.03 |
| 30 | -0.17 | -0.80 | 0.04 |
| 31 | -4.67 | 3.05 | -1.19 |
| 32 | 0.85 | -0.38 | 0.20 |
| 33 | -1.69 | 1.58 | -0.47 |
| 34 | -1.52 | 1.38 | -0.43 |
| 35 | 11.86 | -3.94 | 2.68 |
| 36 | 3.97 | -0.80 | 0.85 |
| 37 | -4.82 | 3.27 | -1.26 |
| 38 | -1.05 | 1.27 | -0.33 |
| 39 | -9.10 | 1.17 | -2.00 |
| 40 | -6.76 | 1.02 | -1.41 |
| 41 | -0.32 | 1.83 | -0.25 |
| RMS | 6.34 | 3.11 | 1.50 |

**Table 5.8: Residuals of the coordinates of control points**

| Point No. | Residuals on range 1 (m) | Residuals on range 2 (m) | Residuals on phase (deg.) | Phase correlation |
|---|---|---|---|---|
| 1 | -5.9 | 4.8 | 20.2 | 0.62 |
| 2 | -2.7 | -4.2 | 61.7 | 0.48 |
| 3 | -1.1 | 2.5 | 20.2 | 0.62 |
| 4 | 1.0 | -0.7 | 18.5 | 0.69 |
| 5 | 1.9 | -4.4 | 24.5 | 0.57 |
| 6 | 0.7 | -1.1 | 18.0 | 0.70 |
| 7 | -1.2 | -7.1 | 65.4 | 0.46 |
| 8 | 7.1 | -6.2 | 19.3 | 0.68 |
| 9 | 3.8 | 1.4 | 49.8 | 0.52 |
| 10 | -5.2 | 5.3 | 17.0 | 0.64 |
| 11 | 2.6 | -1.0 | 21.1 | 0.62 |
| 12 | 3.3 | -2.9 | 15.9 | 0.68 |
| 13 | 0.3 | -1.0 | 18.1 | 0.66 |
| 14 | 1.3 | -0.5 | 16.6 | 0.65 |
| 15 | -3.9 | 5.7 | 22.5 | 0.59 |
| 16 | -0.1 | 4.1 | 35.5 | 0.54 |
| 17 | -3.5 | 6.1 | 25.9 | 0.57 |
| 18 | 5.2 | -6.8 | 21.4 | 0.59 |
| 19 | -1.8 | -4.3 | 57.1 | 0.48 |
| 20 | -2.4 | -4.1 | 61.3 | 0.48 |
| 21 | 3.2 | 0.9 | 39.1 | 0.53 |
| 22 | 0.7 | -1.5 | 16.6 | 0.65 |
| 23 | 2.8 | 0.8 | 31.3 | 0.54 |
| 24 | -1.2 | 3.0 | 24.1 | 0.58 |
| 25 | 0.3 | -1.4 | 17.9 | 0.63 |
| 26 | -0.8 | 3.5 | 26.7 | 0.57 |
| 27 | 5.1 | -2.9 | 25.0 | 0.58 |
| 28 | -0.7 | 3.6 | 29.1 | 0.55 |
| 29 | -4.4 | 0.1 | 43.7 | 0.52 |
| 30 | 3.6 | -3.5 | 15.1 | 0.71 |
| 31 | 5.0 | -7.5 | 25.7 | 0.57 |
| 32 | 3.8 | -3.4 | 17.1 | 0.68 |
| 33 | 0.4 | -1.5 | 19.1 | 0.63 |
| 34 | 0.5 | -1.4 | 18.4 | 0.64 |
| 35 | 9.7 | -3.9 | 52.8 | 0.49 |
| 36 | 1.5 | 0.4 | 23.6 | 0.58 |
| 37 | 2.7 | -5.4 | 28.3 | 0.56 |
| 38 | 0.5 | -1.3 | 18.8 | 0.66 |
| 39 | -1.4 | -2.9 | 39.2 | 0.52 |
| 40 | -0.8 | -2.3 | 29.6 | 0.54 |
| 41 | 0.3 | -0.8 | 16.3 | 0.67 |
| RMS | 3.3 | 3.7 | 31.8 | 0.60 |

**Table 5.9: Residuals in the observation and phase coherence coefficients of control points.**

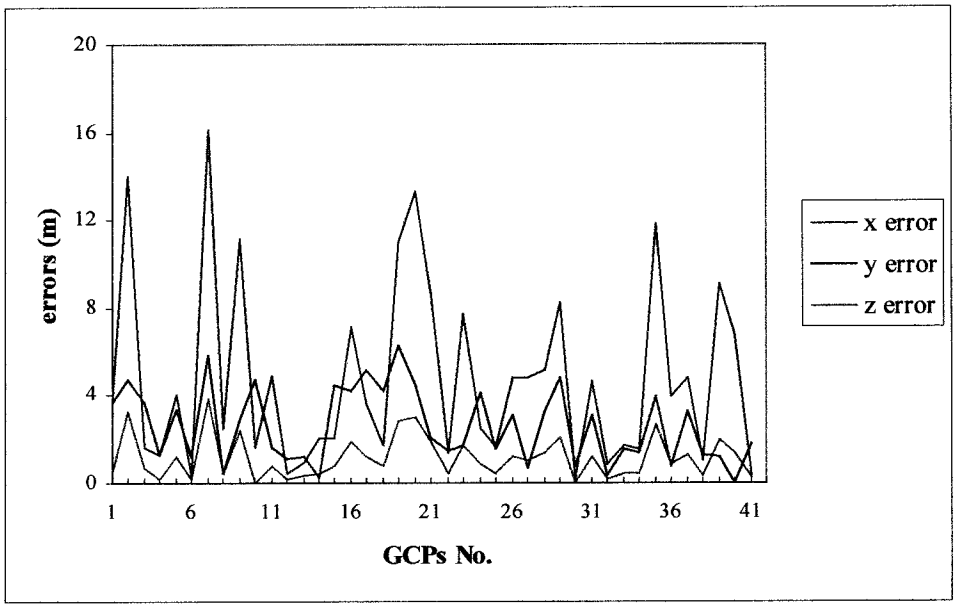


**Figure 5.10: The coordinates error of control points**

| NO. GCPS | ΔX (m) | ΔY (m) | ΔZ (m) |
|---|---|---|---|
| 30 | 4.21 | 3.15 | 1.16 |
| 20 | 4.72 | 3.02 | 1.17 |
| 15 | 4.45 | 3.22 | 1.43 |
| 12 | 5.14 | 3.86 | 1.62 |

**Table 5.10: Residuals of the coordinates of control points.**

| NO. CHECKPOINTS | ΔX (m) | ΔY (m) | ΔZ (m) |
|---|---|---|---|
| 11 | 8.65 | 4.30 | 4.39 |
| 21 | 8.96 | 3.92 | 5.67 |
| 26 | 7.11 | 4.37 | 6.24 |
| 29 | 7.79 | 4.85 | 6.38 |

**Table 5.11: Residuals of the coordinates of checkpoints.**

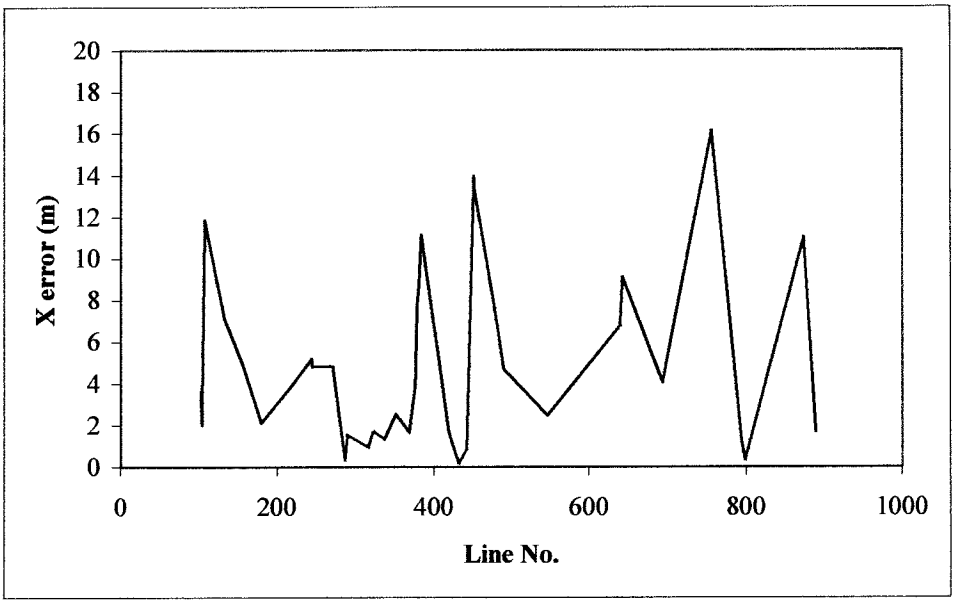


**Figure 5. 11: Error in X component versus line number of each GCPs**

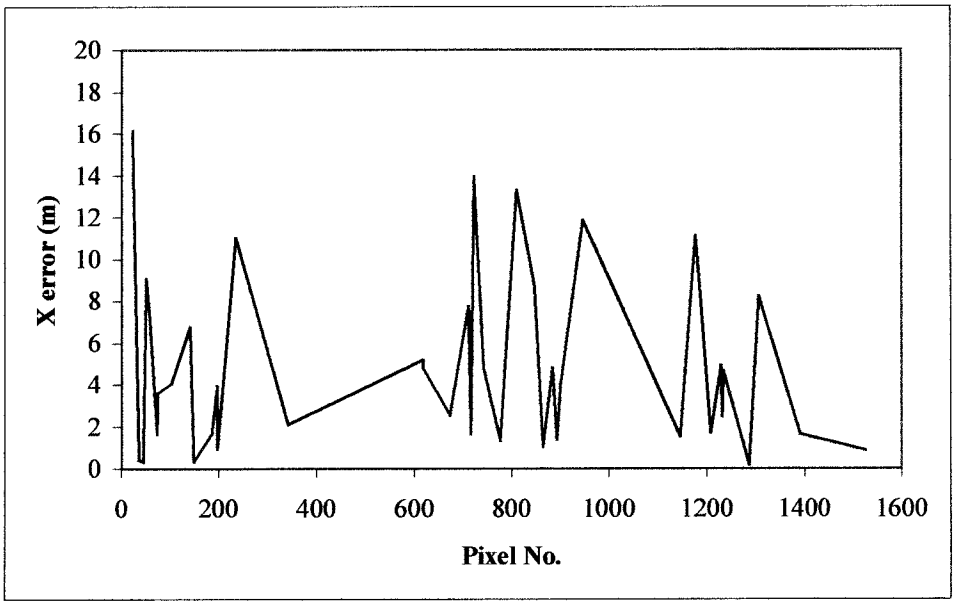


**Figure 5. 12: Error in X component versus pixel number of each GCPs**

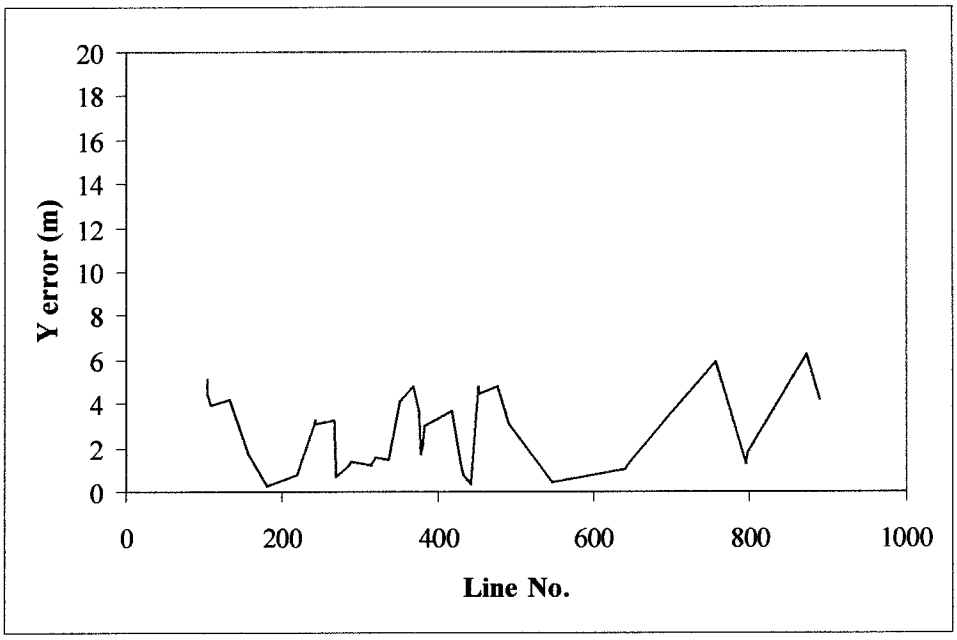


**Figure 5.13: Error in Y component versus line number of each GCPs**

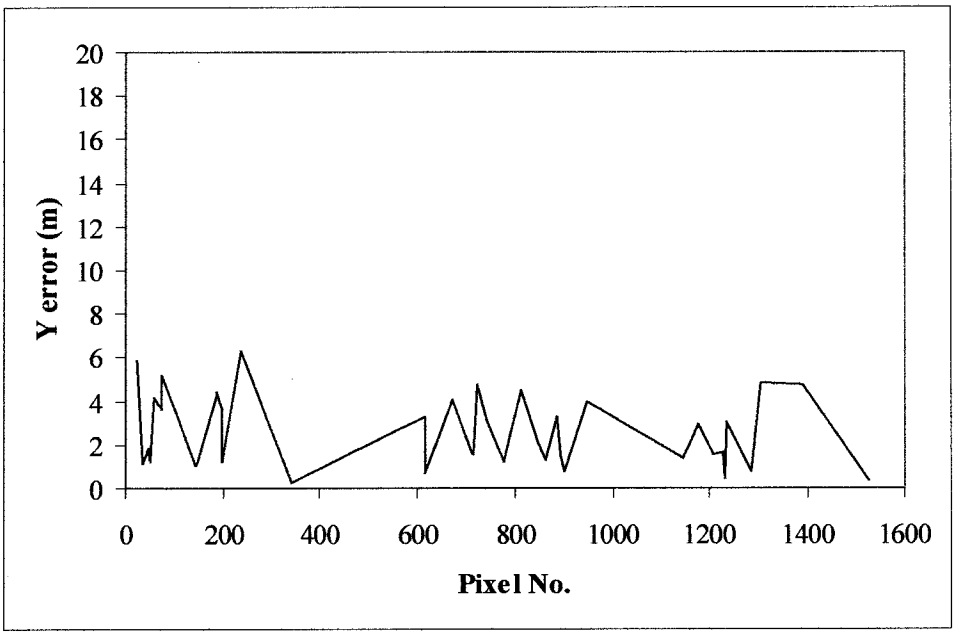


**Figure 5. 14: Error in Y component versus pixel number of each GCPs.**

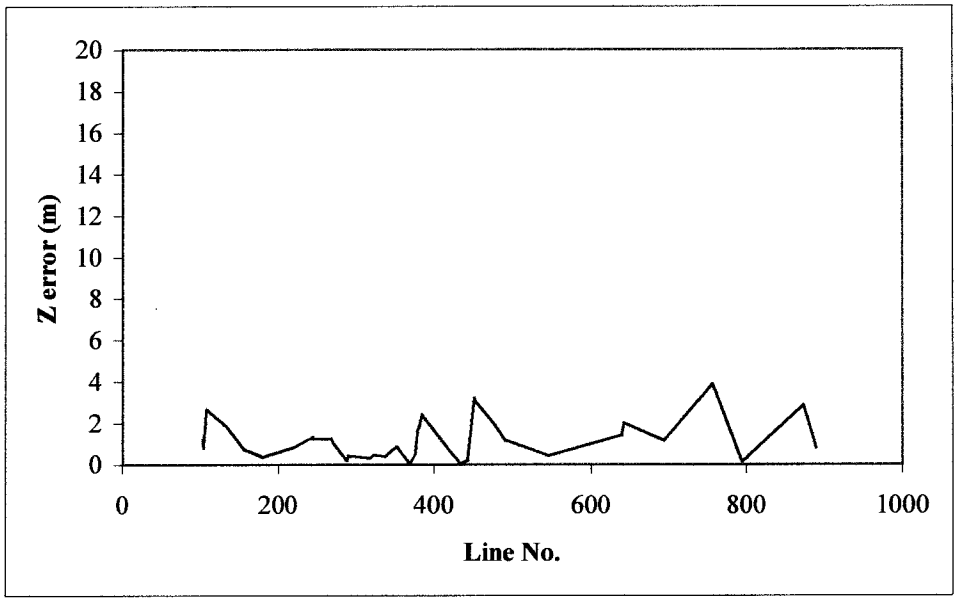


**Figure 5. 15: Error in Z component versus Pixel number of each GCPs.**

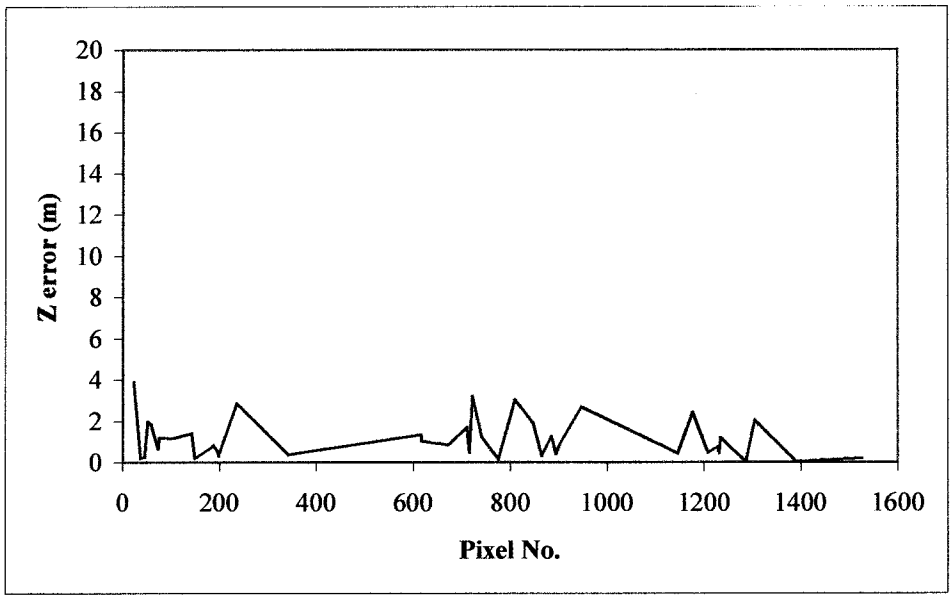


**Figure 5.16: Error in Z component versus line number of each GCPs**

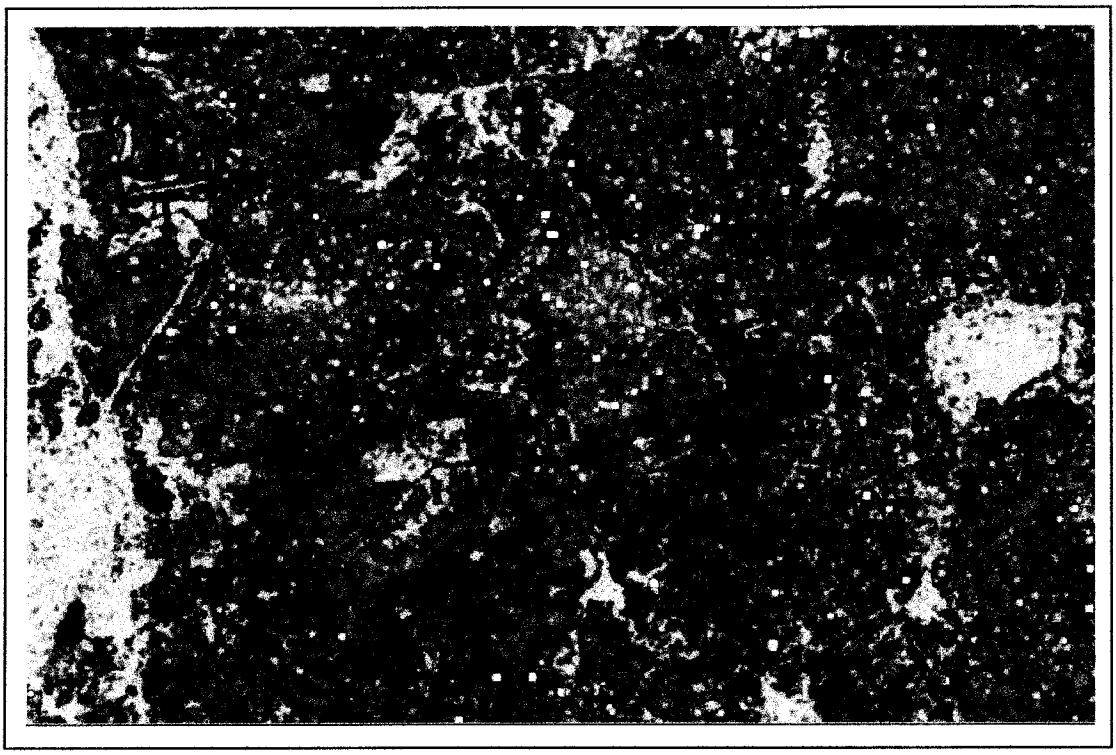


**Figure 5.17: Correlation map. The yellow colour shows the area with high correlation followed by orange and magenta area with medium correlation, and finally cyan colour shows decorrelated areas, including Prospect Reservoir in the east, and Nepean River and Blue Mountains in the west of the map.**

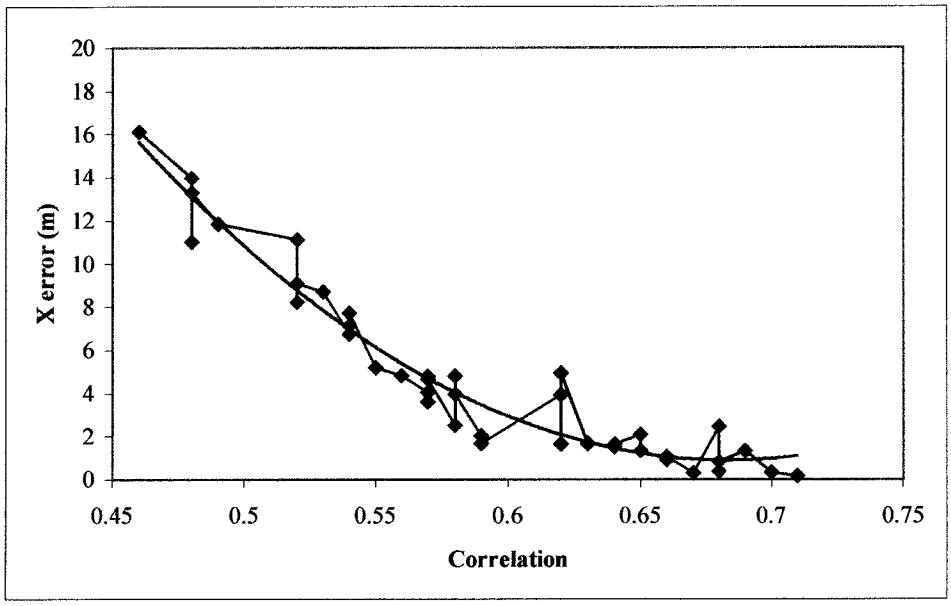


**Figure 5.18: Error in X component versus phase coherence of control points.**

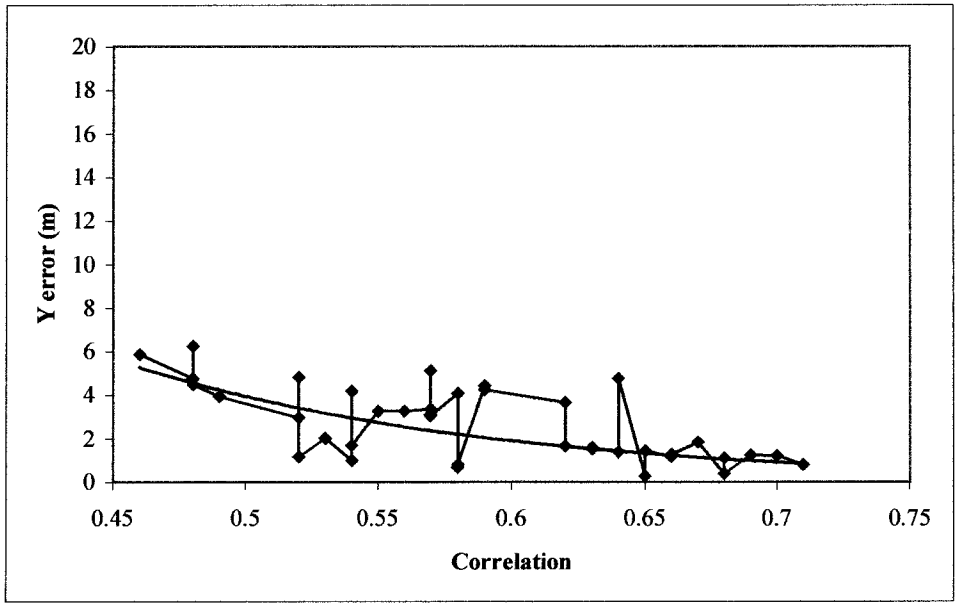


**Figure 5.19: Error in Y component versus phase coherence of control points.**

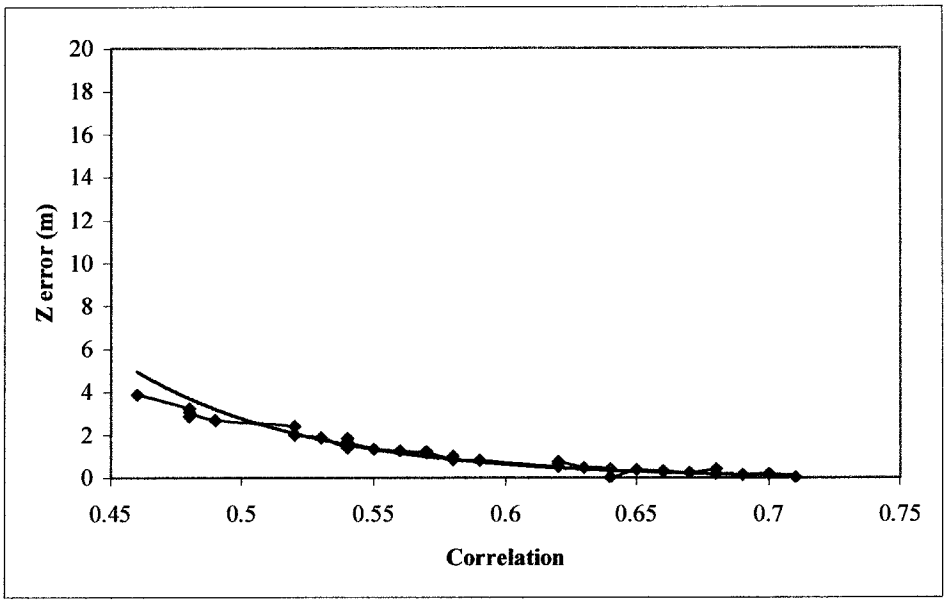


**Figure 5.20: Error in Z component versus phase coherence of control points.**

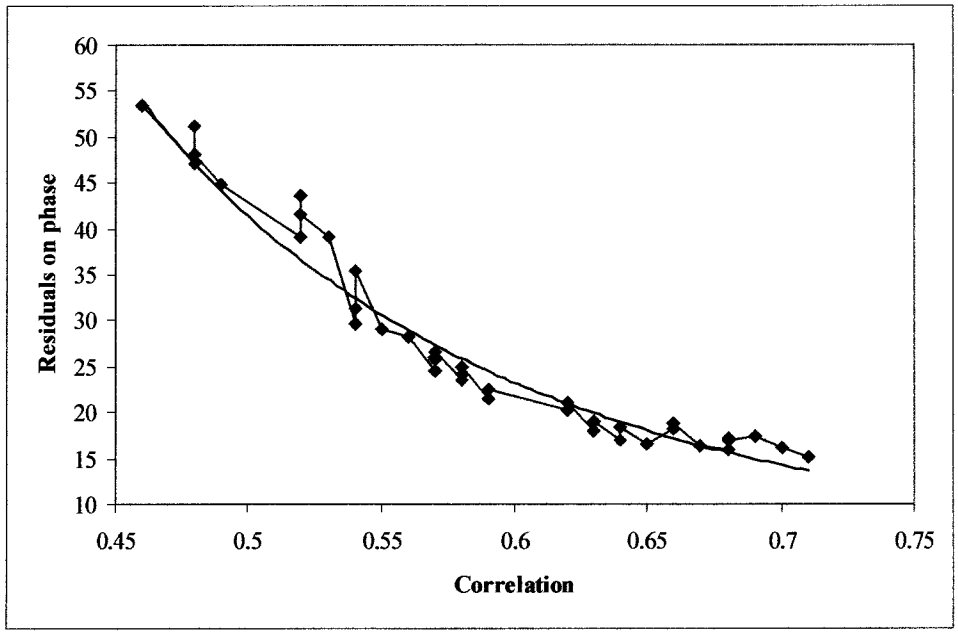


**Figure 5.21: Residuals on phase versus phase coherence of control points.**

between two antennas. While the short baseline in InSAR technique, in many cases is an advantage, it is not recommended in a radargrammetry system. Hence, the ideal form for this study was to use a pair of images obtained by radargrammetry technique to derive range measurements, and data obtained by InSAR technique to derive the phase information. However, only one data set was available and costs of data prohibited the use of more images. In spite of these shortcoming in the configuration of the images satisfactory results have been obtained with them.

### 5.11 Conclusions

This chapter has presented procedures for derivation of heights using ERS-1/ERS-2 tandem data and the solution developed in previous chapters, on a test area in west of Sydney, where 41 GCPs were selected. A point height measurement accuracy of less than 2 m was obtained on GCPs, expressed as RMS errors, which is very satisfactory. Moreover, the model simultaneously, determined planimetry positions of the points. The worst value for accuracy in X component was 16 m, which is high compared with the standard deviation of map accuracy of 5 m. However, the RMS error in X component for 41 point was 6.3 m. For Y component the results were better. The worst value was 6.2 m and the RMS error was 3.1 m, which was comparable with standard deviation of map accuracy. The results of test on the suitable number of GCPs have been shown in appendix 2. They show that the accuracy of planimetry components and height tends to deteriorate as the number of GCPs reduces. The results show that 12 to 15 GCPs are the minimum number of points that result in a 5m to 6m accuracy in heights of checkpoints and 7 m for X coordinate and 4 m-5 m for the Y coordinate.

There is a very high correlation between the accuracy of coordinates and the level of the phase coherency. The points with coherency of more than 0.65 demonstrate outstanding results. On the other hand, over areas with decorrelated data, there was no phase information to obtain the heights. It seems that it is unlikely that accurate DEMs over the dense forest by means of repeat-pass interferometry is possible.

However, this study is a combination of InSAR and radargrammetry. The ideal geometry of InSAR is far from ideal for the radargrammetry techniques. The most obvious difference is the distance between two antennas. While the short baseline in InSAR technique, in many cases is an advantage, it is not ideally suited for a radargrammetry system. Hence, the ideal form is to use a pair of images obtained by radargrammetry technique to derive range measurements, and data obtained by InSAR technique to derive the phase information.

# *Chapter Six*

# Conclusions

## 6.1 Summary of the study

This thesis has presented a number of important issues on the estimation of terrain elevations using InSAR. The procedure uses the difference of phase measurements of the received radar signals at two antennas to determine the elevations more accurately than stereo SAR mapping, which uses SAR intensity images. The SAR phases are more sensitive to terrain elevation variations than SAR intensities. In InSAR the observable terrain shift is of the order of the radar wavelength rather than the resolution cell size. Therefore, InSAR is potentially more accurate than stereo mapping in obtaining elevations.

The parameters which affect the accuracy of elevations determined by InSAR have been discussed. The correlation of corresponding pixels on the two images, which refer to the same area on the terrain, are fundamental to height determination by InSAR. This study explored the effects of various parameters on the image correlation, and investigated how the error sources affect the height accuracy derived by InSAR.

Geophysical properties of surfaces, which affect the level of decorrelation observed in repeat-pass implementation, have been explained. It was found that smaller wavelengths are more sensitive to temporal changes of these properties and cause a greater level of decorrelation. The effects of the type of surface cover on correlation of the images was another subject discussed. The interactions of radar signals with vegetation are very complicated. Volume scattering occurs in the propagation of signals through forest canopy. C- band scatterers are dominant in these areas, the; i.e. small branches in the top of the trees may be affected by temporal effects, such as wind conditions. Therefore

over forest areas, C-band interferometry results in low correlation. Since, for both HV and VV polarisation, the scattering is dominated by returns from branches, which are highly influenced by temporal effects, these polarised signals show less correlation. However for P band, a HH polarised image may show more correlation due to dominant trunk/ground scattering, which is less sensitive to temporal conditions.

It was also found that the inaccuracy in height estimation decreases as the look angle increases. The larger look angles will also minimise layover and foreshortening. However, the look angle must not be so large as to cause significant shadowing or loss in SNR due to angular variation of target cross-section, which results in decorrelation. An important factor in InSAR techniques, is the distance between two antennas. A longer baseline results in higher mapping accuracy, but it must be small enough to preserve correlation.

It has been showed that uncertainties in orbit determination cause an absolute error in elevations of the order of several hundred metres. They are systematic errors which affect every point in the image, and can be removed using heights of a few control points in a given image scene. Therefore orbit determination in InSAR techniques is critical. A model was developed to calculate absolute terrain elevations incorporating ground control data. It also is based on the sensor orbits and estimates the planimetric positions of the each point in the image. The computation procedure is based on stereo radargrammetric mapping of overlapping SAR images, incorporating expressions for elevation based on the fringe information in InSAR. The model develops a simultaneous least squares adjustment of all the measurements by radargrammetry and interferometric SAR together with ground control, using condition and observation equations. In this case the basic measurements include range, unwrapped phase, and the ground coordinates of control points. The purpose of the least squares adjustment is to determine the most probable solution for the ground coordinates of points, and orbital parameters, represented by polynomials.

The algorithm has been tested with a pair of ERS-1 and ERS-2 images in tandem mode over Sydney. The algorithm shows good performance in achieving SAR elevation

mapping, as compared with contours on an orthophoto map. The errors are highly affected by quality of the phase correlation of the points. However, there is no correlation between the position of the point and magnitude of errors in planimetry and height.

The accuracy of ground point heights determined by this solution was validated on the GCPs, for which RMS errors of less than 2 m were obtained. Moreover, the model simultaneously, determined planimetry positions of the points. The RMS errors in X and Y components over GCPs were 6.3 m and 3.1 m, respectively. However, this estimated accuracy is only based on residuals on control points. It is higher for checkpoints when fewer than all points are used as control. The accuracy of the planimetry components and height tend to deteriorate as number of GCPs reduces. It can be concluded from the tests that 12 to 15 GCPs are the recommended minimum number of points, resulting in 5m to 6m accuracy in height. The results of planimetry components are still very satisfactory with 12 GCPs.

It was observed that there is a very high correlation between the accuracy and the level of the phase coherency. The results show that the higher phase coherence level, the better estimation of point location. The points with coherency degree of more than 0.65 demonstrated outstanding results, whereas over the decorrelated area, there was no phase information to obtain height. It seems that it is unlikely to obtain high accuracy DEMs over dense forest by means of repeat- track interferometry.

## 6.2 Suggestions for future research

Since this study is a combination of InSAR and radargrammetry, the ideal situation is the combination data obtained from both techniques. The geometry of images suitable for InSAR is far from ideal for the radargrammetry techniques. The most obvious difference is the distance between two antennas. While the short baseline in InSAR technique, in many cases is an advantage, it is not recommended in a radargrammetry system. Hence, the ideal form is to use a pair of images obtained by radargrammetry

technique to derive range measurements, and data obtained by InSAR technique to derive the phase information.

Selecting ground control points was one of the critical stages of this study. In an ideal case man-made features like roads or crossing of such linear features should be typically detected. However, such features may either not always be available, or may not be clearly visible in SAR images due to noise. Moreover, other specific SAR features like layover and foreshortening hindered the task of locating of the desired ground control points on the image. Hence, an approach to overcome this is using corner reflectors (CRs), particularly when the image lacks sufficient man-made features. Since the ground control points must be chosen in a high correlation area, it is necessary to maintain the CRs in these areas.

Alternatively, ground control points can be automatically selected. Bauer et al. (1996) explained how candidate points in a reference scene may be automatically detected and the corresponding points in the areas of the other images overlapping the reference image may also be found automatically using proper image matching techniques. Therefore, an algorithm can be developed by using the first part of this method i.e. detection of candidate control points automatically on InSAR image, and finding the corresponding points on the reference map. The condition of high correlation must still be considered.

In some areas the phases in the interferometric SAR images may be extremely noisy, such as over lakes and forest areas. This leads to decorrelated because of surface change. If the area is a lake, the edges of the area can be identified using an edge detection algorithm. Then, since the lake shore should have the same elevation, the mapping process for these areas can be performed.

With the launch of the Shuttle Radar Topography Mission (SRTM) scheduled for September 1999, more exciting research can be expected in using SAR, and particularly InSAR, for better understanding of global geophysical phenomena and the determination of global changes. SRTM is a cooperative 11-day shuttle mission (STS-

99, Atlantis) of NASA, the U.S. Department of Defence's National Imagery and Mapping Agency, German Aerospace Research Centre (DLR), and the Italian Space Agency (ASI). The system will use two independent instruments; one SIR-C instrument with the C- and L- band radars, the other is X-SAR with the X- band developed by Germany by DLR and built under the industrial management of Dornier in cooperation with Alenia Spazio in Italy. SRTM is the first single-pass spaceborne InSAR technology with wide-swath scanning SAR and dual frequency (C- and X- band). It is expected that the SRTM will be a strong solution for the problem of temporal decorrelation of phase observed in repeat-pass InSAR.

# *Appendix One*

# Coordinate Systems

Three coordinates are needed to define the position of the point of interest relative to a set of reference axes defined by to the earth. The locations of points on the earth's surface are usually given in Cartesian, Ellipsoidal (Geodetic), or Natural (Geographic) coordinates.

## A.1 Cartesian Coordinates

The position of a point P in a Cartesian coordinate system (Figure A.1) is determined by its position vector

$$\mathbf{X_p} = (x_p, y_p, z_p) \tag{A.1}$$

The transformation to a second Cartesian coordinate system X', Y', Z' with identical origin, by relate about the z-axis by the angle $\gamma$, can be described by the matrix operation.

$$X'_p = R(\gamma)X_p \tag{A.2}$$

Where

$$R(\gamma) = \begin{bmatrix} \cos\gamma & \sin\gamma & 0 \\ -\sin\gamma & \cos\gamma & 0 \\ 0 & 0 & 1 \end{bmatrix} \tag{A.3}$$

A complete transformation involving rotations around z, y, x by angles $\gamma, \beta, \alpha$, respectively, is:

$$X_p''' = R(\alpha)R(\beta)R(\gamma)X_p \qquad (A.4)$$

Where

$$R(\alpha) = \begin{bmatrix} \cos\alpha & \sin\alpha & 0 \\ -\sin\alpha & \cos\alpha & 0 \\ 0 & 0 & 1 \end{bmatrix} \qquad (A.5)$$

$$R(\beta) = \begin{bmatrix} \cos\beta & \sin\beta & 0 \\ -\sin\beta & \cos\beta & 0 \\ 0 & 0 & 1 \end{bmatrix} \qquad (A.6)$$

## A.2 Ellipsoidal or Geodetic Coordinates

A point P can be located by a set Ellipsoidal coordinates $(\varphi, \lambda, h)$, which closely approximate the Earth's surface (figure A.2). A reference ellipsoid is used to approximate the shape of the Earth over the globe or a particular region of interest. The meridians of this ellipsoid are ellipses. The ellipsoid is created by rotating the meridian ellipse about its minor axis. The geometric parameters of the ellipsoid are:

Semi- major axis: a

Semi- minor axis: b

Flattening: $f = \dfrac{a-b}{a}$

The first numerical eccentricity: $e^2 = \dfrac{a^2 - b^2}{a^2}$

The geodetic ellipsoidal coordinates are: ellipsoidal height (h), the geographic longitude, the angle from the XZ plane to the plane through P and Z-axis ($\lambda$), the geodetic latitude, the angle measured up or down from the XY plane to the normal to the ellipsoid passing through P ($\varphi$). The locus h = constant is an ellipsoid which is

concentric with the reference ellipsoid. The locus of points $\varphi$ = constant is a cone with vertex on the axis OZ, and generating angle $90^0$ - $\varphi$.

A concentric Cartesian system X, Y, Z can be defined within the ellipsoid with the origin at the centre O of the ellipsoid

Z-axis is directed to the northern ellipsoidal pole (along the minor axis)

X axis is directed to the ellipsoidal zero meridian

Y-axis completes a right handed system

The transformation equation between the ellipsoidal coordinate $\varphi, \lambda, h$ and Cartesian X, Y, Z is (Seeber, 1993):

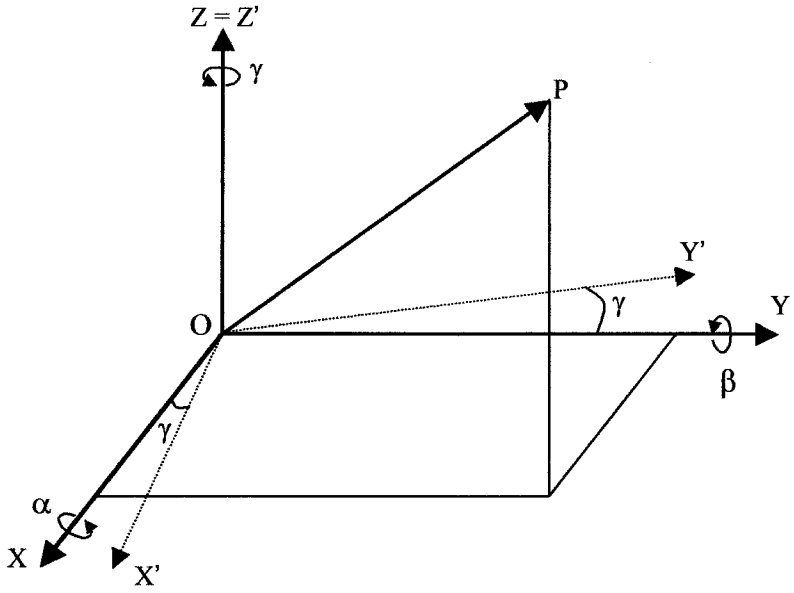


**Figure A.1: Cartesian Coordinate**

$$\begin{bmatrix} X \\ Y \\ Z \end{bmatrix} = \begin{bmatrix} (n+h)\cos\varphi\cos\lambda \\ (n+h)\cos\varphi\sin\lambda \\ ((1-e^2)n+h)\sin\varphi \end{bmatrix} \qquad (A.7)$$

Where n is the prime vertical residue of curvature

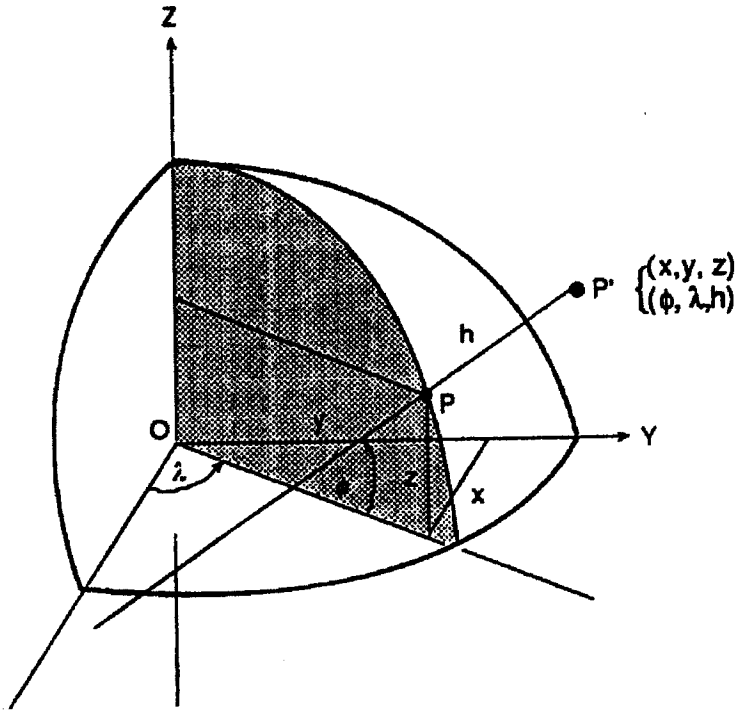


**Figure A.2: Geodetic or Ellipsoidal Coordinates (adapted from Stolz, 1994).**

$$n = \frac{a}{\sqrt{1 - e^2 \sin^2 \varphi}} \tag{A.8}$$

One solution of the inverse transformation problem is (Torge 1991, Ehlert 1991)

$$h = \frac{\sqrt{X^2 + Y^2}}{\cos \varphi} - N$$

$$\varphi = \arctan \frac{Z}{\sqrt{X^2 + Y^2}} \left(1 - e^2 \frac{n}{n + h}\right)^{-1} \tag{A.9}$$

$$\lambda = \arctan \frac{Y}{X}$$

These equations give $\lambda$ directly while, to obtain $\varphi$ and h, it is necessary to iterate between the expressions for $\varphi$ and h, since h is a function of $\varphi$ and vice versa.

## A.3 Natural or geographic coordinates

The geographic system may be used as a three dimensional coordinate system. The direction of the earth's spin axis and the position of the equatorial plane are well defined astronomically. The geographical or astronomical latitude $\Phi$ of a point is the angle between the meridianal component of the direction of gravity or vertical at that point and the equatorial plane of the earth. The plane containing the vertical at a point P and parallel to the rotation axis of the earth is the astronomic meridian plane of P. The angle between this meridian plane and the meridian plane of Greenwich is the geographical or astronomical longitude $\Lambda$ of P, and it is positive towards the east. The orthometric height, H is the third coordinate. It is the distance between the geoid and point P (figure A.3).

## A.4 Ellipsoid, Geoid and Geodetic Datum

Since the physical shape of the real Earth is closely approximated by mathematical surface of the rotational ellipsoid, and the ellipsoidal surface is smooth and convenient for mathematical operations, the ellipsoid is widely used as the reference surface for horizontal coordinates in geodetic networks.

However, the ellipsoid is much less suitable as a reference surface for heights, and instead the geoid is used. The geoid is considered as the surface of mean sea level extending inside the solid body of the Earth. Figure A.4 shows the relationship between geoid and reference ellipsoid. The vertical separation between the geoid and a particular reference ellipsoid is called geoid undulation N. The geometrical relation between the geoid undulation, the ellipsoidal height (h) and the orthometric height or height above geoid (H) is approximately:

$$h = N + H \qquad (A.10)$$

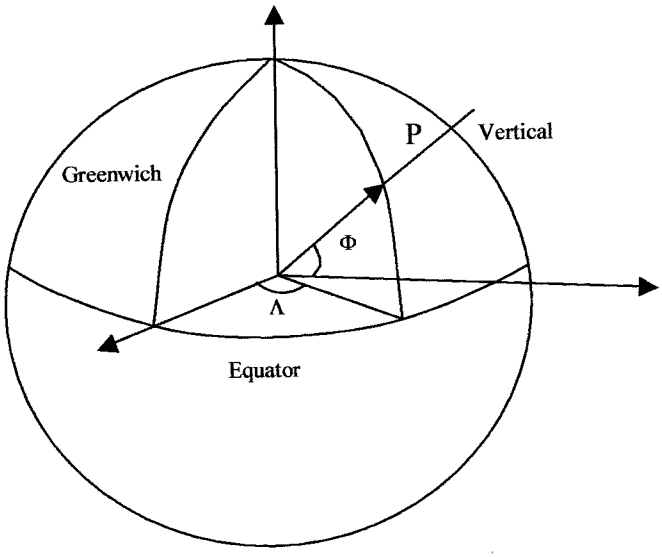


**Figure A.3: Geographic Coordinates**

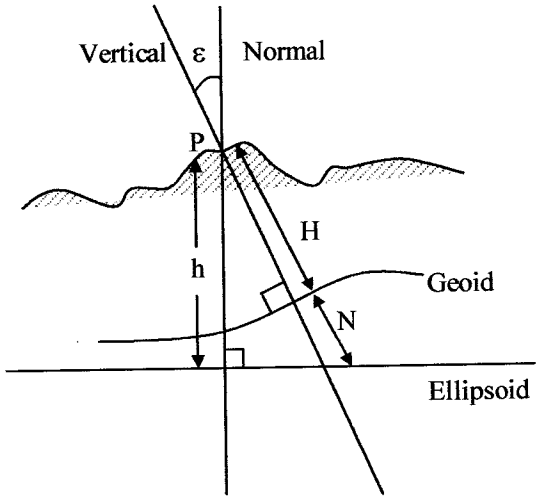


**Figure A.4: Relationship between Geoid and Ellipsoid.**

## A.5 Local and Global Ellipsoids

Local models are selected to fit the geoid over the region being mapped. Thus for Australia an ellipsoid of suitable size and shape was selected to best fit the geoid over the continent, by minimising the magnitude of the tilt or deflection of the geoid with respect to the ellipsoid. This approach led to the development of the Australian National Spheroid (ANS) which was used for computation to produce the set of geodetic coordinates known as the Australian Geodetic Datum 1966 (AGD66).

However, a model to best fit the geoid over the whole surface area of the Earth was required. Hence, the Earth centred reference system has been adopted for the whole Earth, based on the latest information. The reference system adopted in 1980, known as the Geodetic Reference System 1980 (GRS80) was used by the United States Defense Mapping Agency as the basis for the World Geodetic System 1984 (WGS84), which is currently used for the GPS satellite navigation system. The WGS84 ellipsoid parameters are:

Semi major axis a = 6378137 m  Inverse flattening 1/f = 298.257223563

## A.6 Reference Coordinate Systems

Appropriate reference coordinate systems are essential in satellite geodesy. These are global and geocentric, because satellite motion refers to the centre of mass of the Earth. In satellite geodesy usually two systems are applied: a space-fixed inertial reference system, Conventional Inertial System (CIS), for description of satellite motion, and an Earth fixed terrestrial reference system, Conventional Terrestrial System (CTS), for position of the observation stations and for description of results from satellite geodesy.

The origin of the CIS is supposed to coincide with the geocentre M in figure A.5. The XY plane can be either the equatorial plane or the ecliptic (Earth's mean orbital plane about the Sun). The Z-axis which is positive oriented towards the North Pole, is perpendicular to the XY plane. The XZ plane contains the vernal equinox (the intersection of the ecliptic and the earth's equator with the positive sense being from the

earth to the sun as the sun crosses the equator from south to north) and the Z-axis. The Y-axis is selected to form the right-handed system. This system, which is tied to fundamental stars, is also called Stellar CIS to distinguish it from other inertial systems (Seeber, 1993)

CTS can be realized through a set of Cartesian coordinates (figure A.5). Its origin is at the earth's centre of mass. CTS has a conventional direction to the mean orientation of the polar axis (conventional terrestrial pole, CTP). The mean equatorial plane perpendicular to the Z-axis generates the XY-plane. The mean meridian, which contains the Z-axis and the Greenwich mean observatory (GMO) form the XZ, plane. The intersection of the XY- and XZ planes forms the X-axis, with the positive direction being through the GMO. The Y-axis is selected to complete a right-handed system. This system is also called Earth Centred Earth Fixed system (ECEF).

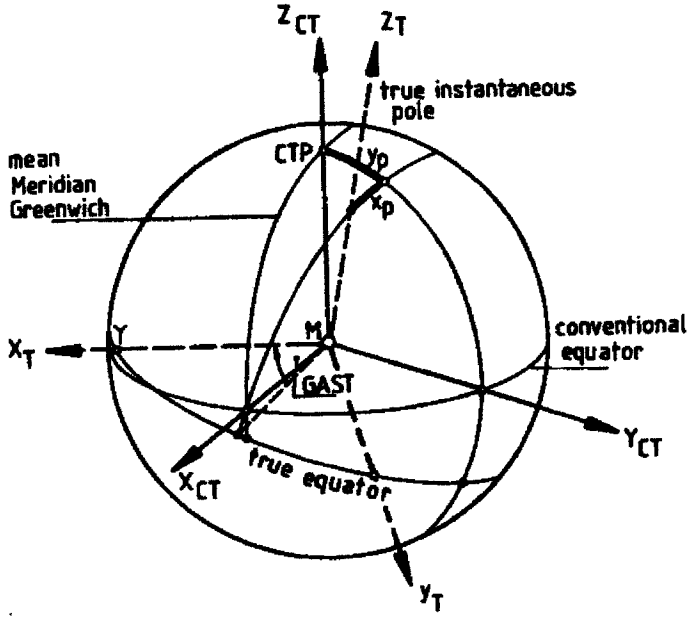


**Figure A.5: CTS Coordinate System (adapted from Seeber, 1993)**

# *Appendix Two*

# Tests on the suitable number of GCPs

**30 GCPs:**

| POINT NO. | ΔX (m) | ΔY (m) | ΔZ (m) |
|---|---|---|---|
| 1 | -6.31 | -4.21 | 1.41 |
| 3 | 3.24 | 4.65 | 1.12 |
| 4 | 2.34 | 2.31 | 0.95 |
| 5 | -9.23 | 4.31 | -1.95 |
| 6 | 1.96 | 2.12 | 0.79 |
| 8 | 2.45 | 1.53 | 0.67 |
| 10 | 2.51 | 4.35 | 0.35 |
| 11 | 2.11 | -2.76 | 1.24 |
| 12 | 1.84 | 1.89 | 0.35 |
| 13 | 2.41 | -2.37 | 1.34 |
| 14 | -1.75 | 0.64 | 1.56 |
| 15 | -5.23 | 4.51 | 1.24 |
| 17 | 4.57 | -4.23 | 1.34 |
| 18 | 6.32 | 5.32 | -1.41 |
| 21 | -7.99 | 3.14 | 1.63 |
| 22 | 2.39 | 1.54 | 1.45 |
| 24 | -5.03 | 4.53 | 0.89 |
| 25 | -2.85 | 1.89 | -0.78 |
| 27 | 5.63 | 0.96 | 1.31 |
| 28 | 4.36 | 4.21 | 1.41 |
| 30 | 1.23 | -0.89 | 0.45 |
| 31 | 6.23 | 3.69 | -1.32 |
| 32 | 2.34 | -1.26 | 0.65 |
| 33 | 1.73 | 1.97 | 0.94 |
| 34 | -1.95 | 2.11 | 0.51 |
| 36 | 4.21 | 2.65 | 1.14 |
| 37 | 4.56 | 4.56 | -1.56 |
| 38 | -2.18 | 1.51 | -0.99 |
| 40 | 4.08 | 3.21 | 1.22 |
| 41 | -1.68 | 2.31 | -0.66 |
| RMS | 4.21 | 3.15 | 1.16 |

**Table A2.1: Residuals of the coordinates of control points (30 GCPs)**

| POINT NO. | ΔX (m) | ΔY (m) | ΔZ (m) |
|---|---|---|---|
| 2 | -11.31 | 5.53 | -6.31 |
| 7 | -10.32 | 4.41 | -9.14 |
| 9 | 9.61 | -1.89 | 4.12 |
| 16 | 6.51 | -4.31 | 2.13 |
| 19 | -8.23 | 5.43 | 2.53 |
| 20 | 9.32 | 4.15 | 4.18 |
| 23 | 7.31 | -3.11 | 2.55 |
| 26 | 5.76 | -3.92 | -2.15 |
| 29 | -7.33 | 5.43 | 3.96 |
| 35 | 7.32 | -4.96 | 2.93 |
| 39 | -10.24 | 2.25 | 2.87 |
| RMS | 8.65 | 4.30 | 4.39 |

**Table A2.2: Residuals of the coordinates of check points (11 checkpoints)**

**20 GCPs:**

| POINT NO. | ΔX(m) | ΔY(m) | ΔZ(m) |
|---|---|---|---|
| 1 | -7.66 | -4.52 | -1.12 |
| 3 | 2.34 | 2.55 | 1.15 |
| 4 | 2.13 | 2.43 | 0.57 |
| 5 | 7.05 | 4.32 | -2.60 |
| 6 | 2.74 | -1.35 | 0.76 |
| 8 | 1.29 | 4.12 | 0.67 |
| 10 | -9.72 | -3.79 | 0.53 |
| 12 | -1.84 | -0.11 | 0.84 |
| 13 | 2.70 | -2.18 | -0.71 |
| 14 | 0.95 | 3.08 | 1.52 |
| 15 | -8.52 | 3.73 | 1.52 |
| 18 | 8.27 | -3.54 | -1.60 |
| 22 | 3.28 | -3.40 | -2.01 |
| 25 | 3.42 | -3.58 | -1.04 |
| 30 | -1.14 | -1.17 | 0.29 |
| 32 | -0.23 | 0.92 | 0.43 |
| 33 | 3.54 | -3.62 | -1.03 |
| 34 | 3.19 | -3.27 | -0.93 |
| 38 | 2.95 | -2.42 | -0.76 |
| 41 | 3.97 | -0.86 | -0.58 |
| RMS | 4.72 | 3.02 | 1.17 |

**Table A2.3: Residuals of the coordinates of control points (20 GCPs)**

| POINT NO. | ΔX(m) | ΔY(m) | ΔZ(m) |
|---|---|---|---|
| 2 | -12.55 | 5.78 | -5.72 |
| 7 | -14.01 | 4.98 | -11.90 |
| 9 | 13.00 | -2.00 | 7.63 |
| 11 | 5.03 | 2.00 | 2.23 |
| 16 | 6.99 | -4.00 | 6.65 |
| 17 | 3.00 | -2.99 | 3.93 |
| 19 | -10.91 | 5.96 | 2.48 |
| 20 | -12.99 | 6.00 | -9.91 |
| 21 | 7.94 | -1.99 | 1.45 |
| 23 | 7.99 | -2.01 | 5.78 |
| 24 | 3.00 | -4.00 | 2.89 |
| 26 | 6.01 | -5.00 | 3.34 |
| 27 | 4.94 | -0.97 | 4.12 |
| 28 | 4.99 | -4.00 | 4.23 |
| 29 | 6.01 | -5.00 | -7.33 |
| 31 | -4.98 | 3.00 | -4.22 |
| 35 | 13.98 | -5.10 | 9.21 |
| 36 | 5.03 | -1.00 | 2.10 |
| 37 | 3.87 | -3.49 | 1.36 |
| 39 | -12.94 | 3.65 | 3.27 |
| 40 | -10.38 | 2.78 | -3.04 |
| RMS | 8.96 | 3.92 | 5.67 |

**Table A2.4: Residuals of the coordinates of check points (21 check points)**

**15 GCPs:**

| POINT NO. | ΔX (m) | ΔY (m) | ΔZ (m) |
|---|---|---|---|
| 1 | -5.78 | -5.23 | 1.23 |
| 4 | 3.89 | 3.34 | -0.96 |
| 6 | 4.12 | 3.17 | 1.2 |
| 8 | -4.81 | 2.96 | 1.41 |
| 10 | -4.19 | -4.15 | 0.89 |
| 12 | -4.23 | 2.31 | -1.53 |
| 13 | 4.61 | -2.87 | 1.54 |
| 14 | -4.11 | -1.94 | 2.17 |
| 22 | -4.76 | 1.87 | 1.2 |
| 25 | -5.11 | 4.21 | -1.34 |
| 30 | 3.65 | 3.85 | 0.51 |
| 32 | -4.65 | -2.37 | 0.56 |
| 34 | 3.65 | 2.11 | -1.29 |
| 38 | 4.53 | -3.01 | -2.39 |
| 41 | 4.08 | 2.89 | 1.86 |
| RMS | 4.45 | 3.22 | 1.43 |

**Table A2.5: Residuals of the coordinates of control points (15 GCPs)**

| POINT NO. | ΔX (m) | ΔY (m) | ΔZ (m) |
|---|---|---|---|
| 2 | -13.00 | 5.99 | -11.42 |
| 3 | 2.00 | -3.99 | 1.52 |
| 5 | -4.02 | 3.31 | -4.67 |
| 7 | -16.02 | 5.81 | -13.33 |
| 9 | 10.95 | -2.99 | 8.53 |
| 11 | 3.64 | -5.01 | 1.33 |
| 15 | 1.97 | -4.49 | 1.88 |
| 16 | 3.58 | -5.10 | 3.74 |
| 17 | 2.02 | -4.01 | 4.14 |
| 18 | -3.96 | 3.29 | -1.58 |
| 19 | -3.99 | 3.31 | -12.74 |
| 20 | -13.05 | 8.29 | -7.42 |
| 21 | 6.98 | -4.19 | 6.95 |
| 23 | 7.79 | -1.69 | 6.05 |
| 24 | 3.61 | -5.10 | 2.01 |
| 26 | 3.58 | -5.10 | 4.58 |
| 27 | 4.77 | -3.12 | 3.21 |
| 28 | 6.98 | -4.20 | 3.26 |
| 29 | -7.99 | 4.79 | -6.13 |
| 31 | -4.69 | 2.99 | -4.85 |
| 33 | -1.75 | 4.38 | -1.13 |
| 35 | 7.64 | -4.18 | 8.87 |
| 36 | 5.18 | -3.29 | 1.39 |
| 37 | -4.71 | 3.03 | -4.11 |
| 39 | -8.01 | 4.79 | -5.65 |
| 40 | -6.78 | 0.99 | -5.31 |
| RMS | 7.11 | 4.37 | 6.24 |

**Table A2.6: Residuals of the coordinates of check points (26 checkpoints)**

**12 GCPs:**

| POINT NO. | ΔX(m) | ΔY(m) | ΔZ(m) |
|---|---|---|---|
| 1 | 6.31 | -4.89 | 1.59 |
| 4 | 5.23 | 4.87 | 2.1 |
| 8 | -7.56 | -3.76 | -1.11 |
| 10 | 4.13 | 4.65 | 1.37 |
| 14 | 4.87 | -3.65 | 1.67 |
| 22 | -6.37 | -2.67 | 2.75 |
| 25 | 9.63 | 5.49 | 1.85 |
| 30 | 3.21 | 5.61 | 2.31 |
| 32 | 3.92 | 2.98 | -1.67 |
| 34 | 4.13 | -4.12 | 1.12 |
| 38 | 5.12 | 4.35 | 2.34 |
| 41 | 5.43 | 3.67 | -0.89 |
| RMS | 5.14 | 3.86 | 1.62 |

**Table A2.7: Residuals of the coordinates of control points (12 GCPs)**

| POINT NO. | ΔX(m) | ΔY(m) | ΔZ(m) |
|---|---|---|---|
| 2 | -14.1 | 6.23 | -10.65 |
| 3 | 2 | -3.99 | 2.5 |
| 5 | -4.92 | 4.32 | -4.98 |
| 6 | -2.09 | 3.45 | -2.21 |
| 7 | -15.21 | 6.33 | -10.96 |
| 9 | 14.07 | -3.51 | 9.44 |
| 11 | 6.12 | 2.47 | 2.78 |
| 12 | 1.51 | -3.51 | 3.52 |
| 13 | -2.96 | 3.13 | 4.1 |
| 15 | 3.71 | -5.62 | 4.12 |
| 16 | 8.13 | -4.87 | 5.85 |
| 17 | 4.31 | -6.51 | 6.19 |
| 18 | -6.53 | 7.23 | 5.43 |
| 19 | -8.76 | 9.69 | -11.57 |
| 20 | -11.88 | 5.49 | -7.15 |
| 21 | 9.2 | -3.17 | 5.32 |
| 23 | 8.31 | -2.09 | 5.5 |
| 24 | 3.45 | -5.3 | 2.73 |
| 26 | 4.32 | -3.74 | 5.17 |
| 27 | 5.58 | -2.16 | 4.84 |
| 28 | 7.3 | -3.95 | 5.13 |
| 29 | -9 | 5.36 | -7.5 |
| 31 | -5.71 | 4.41 | -6.03 |
| 33 | -2.1 | 3.39 | -2.18 |
| 35 | 10.81 | -7.61 | 10.53 |
| 36 | 5.7 | -2.29 | 3.04 |
| 37 | -4.6 | 3.83 | -6.29 |
| 39 | -9.35 | 5.17 | -4.85 |
| 40 | -7.13 | 1.98 | -7.62 |
| RMS | 7.79 | 4.85 | 6.38 |

**Table A2.8: Residuals of the coordinates of check points (29 checkpoints)**

# *References*


Askne J. & Hagberg J. O., *"Potential of interferometric SAR for classification of land surfaces"*, International Geosience and Remote Sensing Symp., pp. 985-7, 1993.

Adragna F., *"Production de MNT interferometriques sans deroulement de franges (resume)"* Bulletin de la Societe Francaise de Photogrammetrie et Teledetection, Vol. 138, No 39, 1995.

Avery T., & Berlin G., *"Fundamentals of remote sensing and airphoto interpretation"*, 5th ed. Macmillan, New York, 1992.

Bauer A., Raggam H., & Bruner W., *"Automatic tie-pointing in overlapping SAR images"*, International Archives of Photogrammetry and Remote Sensing, Vienna, Vol. 31-B2, pp. 315-320, 1996.

Born M. & Wolf E., *"Principles of optics"*, 6th ed. New York, Pergamon, 1980.

Chen P., and Dowman I., *"Space intersection from ERS-1 synthetic aperture radar"*, Photogrammetric Record, Vol. 15 No. 88, pp. 561-573, 1996.

Colteli M., Fornaro G., Franceschtti G., Lanari R., Miglliacio M., Moreira J, Papathanassion K., Puglisi G, Ricco D, & Schwaebisch M., *"SIR-C/X-SAR multifrequency multipass interferometry: A new tool for geological interpretation"*, Journal of Geophysical Research Vol. 101-E10, pp.23127-148, 1996.

Cumming I., Hawkins D., Macdonald Dettwiler, & Associates Ltd. *"All-Weather mapping with interferometric radar"*, Proc. Of the 23rd International Symp. On Remote Sensing of Environ., Bangkok, pp. 1249- 62, 1990.

Dowman I., *"The geometry of SAR images for geocoding and stereo applications"*, International Journal of Remote Sensing, Vol. 13, No. 9, pp. 1609- 1617, 1992.

Dowman I., Chen P., & Saundercock G., *"Heighting from stereoscopic ERS-1 data"*, Space at the Service of our Environment ESA SP-361, No. 1, pp. 609-614, 1993.

Durden S., Zebker H., & VanZyl J., *"Modeling and observations of forest radar polarisation signature"*, IEEE Trans. Geoscience and Remote Sensing Vol. 27, No.3 pp. 290-301,1989

Ehlert D., *"Differentiele Verschiebungen und Drehungen in dreidimensionalen Koordina-tensystemen"*, DGK B 295, Muenchen, 1991.

Elachi C., *"Spaceborne radar remote sensing: applications and techniques"*, IEEE Press, New York, 1988.

ESA WWW., *"Initial testing of ERS tandem data quality for InSAR applications"*, http://earth1.esrin.esa.it:81, 1998.

Fitch J., *"Synthetic Aperture Radar"*, Springer-Verlag Inc, New York, NY, 1988.

Fornaro G. & Franceschetti, *"Image registration in interferometric SAR processing"*, IEE Proc. Radar, Sonar Navig., Vol. 142, No. 6, pp. 313-320, 1995.

Gabriel A., Goldstein R., & Zebker H., *"Mapping small elevation changes over large areas: Differential radar interferometry"*, Journal of Geophysical Research Vol. 94, pp. 9183-9191, 1989.

Gabriel A. K. & Goldstein R. M., *"Crossed orbit interferometry: theory and experimental results from SIR-B"*, International Journal of Remote Sensing, Vol. 9, No. 5, pp. 857- 872, 1988.

Gallagher N., Sweeny D., & Christensen C., *"Median filtering of speckle noise"*, Technical Report RR-82-6, US Army Missile Lab., Albama, 1974.

Ghiglia D., Mastin G., & Romero L., *"Cellular-automata method for phase unwrapping"*, Journal of the Optic Society of America, No. 4, pp. 267-280, 1987.

Goldstein R., & Zebker A., *"Interferometric radar measurement of ocean surface currents"*, Nature, Vol. 328, pp. 707-709, 1987.

Goldstein R. M., Zebker H. A., and Werner C. L., *"Satellite radar interferometry: two-dimensional phase unwrapping"*, Radio Science Vol. 23, No. 4, pp. 713- 720, 1988.

Goldstein R., Barnett T., & Zebker A., *"Remote sensing of ocean currents"*, Science, Vol. 246, pp. 1282-85, 1989.

Goodman J., *"Introduction to Fourier Optics"*, New York: McGraw-Hill, 1968.

Graham L. C., *"Synthetic interferometer radar for topographic mapping"*, Proc. of the IEEE, Vol. 62, No. 6, pp. 763- 68, 1974.

Gray A. L.& Farris-Manning P. J., *"Repeat-Pass interferometry with airborne synthetic aperture radar"*, IEEE Trans. on Geoscience and Remote Sensing Vol. 31, No. 1, pp. 180- 191, 1993.

Hagberg J. O., Ulander L. M. H., and Askne J., *"Repeat-Pass SAR interferometry over forested terrain"*, IEEE Trans. Geoscience and Remote Sensing Vol. 33, pp.331-340, 1995.

Halliday D., Resnick R., & Walker J., *"Fundamentals of Physics, extended with modern Physics"*, 5th ed., Wiley, New York, 1997.

Hartl P. and Wu X., *"SAR interferometry: Experiences with various phase unwrapping methods"*, Proc. Second ERS-1 Symp., Space at the Service of Our Environment, Hamburg, Germany, pp. 727- 32, 1993a.

Hartl P. H., Thiel K. H., Wu X., and Xia Y. *"Practical application of SAR-interferometry; Experiences made by the institute of navigation"*, Proc. Second ERS-1 Symp. Space at the Service of Our Environment, Hamburg, Germany, pp. 717- 22", 1993b.

Hoekstra P. & Denaly A., *"Dielectric properties of soil at UHF and microwave frequencies"*, Journal of Geophysical Research, Vol. 79, pp. 1699-1708, 1974.

JPL WWW, *"Operational use of civil space-based synthetic aperture radar"*, prepared by the interagency Ad Hoc working group on SAR, http:/southport.jpl.nasa.gov/reports, 1996.

Just D., & Bamler R., *"Phase statisticsof interferograms with application to synthetic aperture radar"*, Appl. Optics., Vol. 33, pp.950-959, 1994.

Kimura H., *"A method to estimate baseline and platform altitude for SAR interferometry"*, International Geosience and Remote Sensing Symp., pp. 199- 201, 1995.

Kino G., *"Acoustic waves: devices, imaging, and analog signal processing"*, Prentice-Hall, Englewood Cliffs, N.J., 1987.

Kozma A., Leith E., and Massey N., *"Tilted plane optical processor"*, Applied Optics, Vol. 11, pp.1766-1777, 1972.

Kwok R., & Fahnestock M., *"Ice sheet motion and topography from radar interferometry"*, IEEE Trans. Geoscience and Remote Sensing Vol. 34, No. 1, pp.189-200, 1996.

Leberl F., *"Radargrammetric image processing"*, Artech House Inc., Norwood., 1990.

Leberl F. W., Domic G., Raggam J., and Kobrick M. *"Radar stereomapping techniques and application to SIR-B images of Mt. Shasta"*, IEEE Trans. on Geoscience and Remote Sensing Vol. Ge-24, No. 4, pp. 473-81, 1986a.

Leberl F., Domik G., Raggam J., Cimino J., & Kobrick M. *"Multiple incidence angle SIR-B experiment over Argentina: stereo-radargrammetric analysis"*, IEEE Trans. on Geoscience and Remote Sensing Vol. Ge-24, No. 4, pp. 482- 91, 1986b.

Li F., and Goldstein R. M., *"Studies of multi-baseline spaceborne interferometric synthetic aperture radars"* ", IEEE Trans. on Geoscience and Remote Sensing Vol. 28, No. 1, pp. 88-971, 1990.

Lin Q., Veseckly J. F., and Zebker H. A. *"New approaches in interferometric SAR data"*, IEEE Trans. on Geoscience and Remote Sensing Vol. 30, No. 3, pp. 560- 67, 1992a.

Lin Q., Veseckly J. F., and Zebker H. A., *"Registration of interferometric SAR images"*, International Geoscience and Remote Sensing Symp., Vol. 2 pp. 1579- 81, 1992b.

Lin Q.,Vesecky J., & Zebker A., *"Comparison of elevation derived from InSAR data with DEM over large relief terrain"*, International Journal of Remote Sensing, Vol. 15, pp. 1775-1790, 1994.

Madsen S. N., Zebker H. A. and Martin J. *"Topographic mapping using radar interferometry: Processing techniques"*, IEEE Trans. on Geoscience and Remote Sensing Vol. 31, No. 1, pp. 246- 256, 1993.

Massonnet D. and Rabaute T., *"Radar interferometry: Limits and potential"*, IEEE Trans. On Geoscience and Remote Sensing Vol. 31, No. 2, pp. 455- 463, 1993.

Massonnet D., Feigl K., Rossi M., & Adragna F., *"Radar interferometric mapping of deformation in the year after the Landers earthquake"*, Nature, No. 369, pp. 227-230, 1994.

Mikhail E., "Observations and least squares", IEP, New York, 1976.

Prati C., Rocca F., & Monti Guarnieri A., 1989, *"Effects of speckle and additive noise on the altimetric resolution of interferometric SAR (InSAR) surveys"* International Geoscience and Remote Sensing Symp., Vancover, Canada, pp. 2469-2472.

Prati c., Rocca F., 1990, *"Limits to the resolution of elevation maps from stereo SAR images"*, International Journal of Remote Sensing, Vol. 11, pp. 2215-2235.

Prati C., Rocca F., & Monti Guarnieri A., 1992, *"SAR interferometry experiments with ERS-1"*, Proc. First ERS-1 Symp. - Space at the Service of our Environment, Cannes, France, pp. 211-88.

Pratt W., *"Correlation techniques of image registration"*, IEEE Trans. Aerospace and Electronic Systems, AES-10 (3), pp. 353-358, 1974.

Redfern's formula 1968 section 5.6

Richards J., Forster B., & Milne A., *"Short course on remote sensing with synthetic aperture radar, introductory and advance"* The University of New South Wales, Centre for Remote Sensing, 1987.

Rodriguez and Martin J. M., *"Theory and design of interferometric synthetic aperture radars"*, IEE Proc.- f, Vol. 139, No. 2 pp. 147- 159, 1992.

Rogers A., & Ingalls R., *"Venus: Mapping the surface reflectivity by radar interferometry"*, Science, No. 165, pp.797-799, 1969.

Seeber G., *"Satellite geodesy: foundations, methods, and applications"*, Walter de Gruyter, Berlin - New York, 1993.

Skolnik M., *"Introduction to radar systems"*, 2nd ed., McGraw-Hill, New York, NY, 1981.

Slama, C. C. (Ed.), *"Manual of Photogrammetry, Chap. 10"*, American Society of Photogrammetry, Falls Church, Va. 1980.

Small D., Werner C. & Nueesch D., *"Baseline modelling for ERS-1 interferometry"*, Proc. Of International Geoscience and Remote Sensing Symp., Tokyo, Japan, pp.1204-6, 1993.

Sveldow M., McGillem C., & Anuta P., *"image registration: similarity measure and processing method comparisons"*, IEEE Trans. Aerospace and Electronic Systems, AES-14 (1), pp. 141-149, 1978.

Stolz A., *"An introduction to geodesy"*, School of Geomatic Engineering, The University of New South Wales, Monograph 16, 1993.

Torge W., *"Geodesy"* 2nd ed., Walter de Gruyter, Berlin - New York, 1991.

Ulaby F. T., Moore R. K., & Fung A. K., *"Microwave remote sensing active and passive"* Vol. 2, pp. 630- 77, 1982.

Van Zyl J. J., *"The effect of topography on radar scattering from vegetated areas"*, IEEE Trans. on Geoscience and Remote Sensing, Vol. 31, No. 1, pp. 153- 160, 1993.

Wegmuller U., Werner C. L., & Rosen P. A. *"Derivation of terrain slope from SAR interferometric phase gradient"* Proc. Second ERS-1 Symp. Space at the Service of Our Environment, Hamburg, Germany, pp. 711- 715, 1993.

Wegmuller, and Werner C. L. *"SAR interferometric signatures of forest"*, IEEE Trans. Geoscience and Remote Sensing Vol. 33, No. 5, pp.1153-61, 1995.

Werner C. L., Hensley S., Goldstein R., Rosen P., & Zebker H., *"Techniques and applications of SAR interferometry for ERS-1: topographic mapping, change detection and slope measurement"*, Proc. Of the First ERS-1 Symp. Cannes, France, pp. 205-210, 1992.

Werner C. L., Wegmuller U., Small D. L., & Rosen P. A. *"Applications of interferometrically derived terrain slopes: Normalization of SAR backscatter and the interferometric correlation coefficient"* Proc. First ERS-1 Symp. Space at the Service of Our Environment, Hamburg, Germany. pp. 723- 26, 1993.

Zebker H. A. & Goldstein R. M., *"Topographic mapping from interferometric synthetic aperture radar observations"*, Journal Geophysics Research, Vol. 91 B5, pp. 4993-4999, 1986.

Zebker H. A. & Villasenor J., *"Decorrelation in interferometric radar echoes"*, IEEE Trans. on Geoscience and Remote Sensing, Vol. 30, No. 5, pp. 950- 959, 1992.

Zebker H. A., Werner C. L., Rosen P. A. & Hensley S. *"Accuracy of topographic maps derived from ERS-1 interferometric radar"*, IEEE Trans. on Geoscience and Remote Sensing Vol. 32, No. 4, pp. 823- 836", 1994

Zebker H. A., Rosen P. A., Goldstein R., Gabriel A., & Werner C. L., *"On the derivation of cosaismic displacement fields using differential radar interferometry: The landers earthquake"*, Journal of Geophysical Research, Vol. 99, pp. 19617-634, 1994a.

Publications from the

SCHOOL OF SURVEYING AND SPATIAL INFORMATION SYSTEMS
(formerly: SCHOOL OF GEOMATIC ENGINEERING)

THE UNIVERSITY OF NEW SOUTH WALES
ABN 57 195 873 179

To order, write to:
Publications Officer, School of Surveying and Spatial Information Systems
The University of New South Wales, UNSW SYDNEY NSW 2052, AUSTRALIA

NOTE: ALL ORDERS MUST BE PREPAID. CREDIT CARDS ARE ACCEPTED.
SEE BACK PAGE FOR OUR CREDIT CARD ORDER FORM.

## MONOGRAPHS

Australian prices include postage by surface mail and GST.
Overseas prices include delivery by UNSW's air-lifted mail service (~2-4 weeks to Europe and North America).
Rates for air mail through Australia Post on application.

(Prices effective October 2001)

| | | **Price** Australia (incl. GST) | **Price** Overseas |
|---|---|---|---|
| M1. | R. S. Mather, "The Theory and Geodetic Use of some Common Projections", (2nd edition), 125 pp, 1978. | $ 16.50 | $ 15.00 |
| M2. | R. S. Mather, "The Analysis of the Earth's Gravity Field", 172 pp, 1971. | $ 8.80 | $ 8.00 |
| M3. | G. G. Bennett, "Tables for Prediction of Daylight Stars", 24 pp, 1974. | $ 5.50 | $ 5.00 |
| M4. | G. G. Bennett, J. G. Freislich & M. Maughan, "Star Prediction Tables for the Fixing of Position", 200 pp, 1974. | $ 8.80 | $ 8.00 |
| M8. | A. H. W. Kearsley, "Geodetic Surveying", 96 pp, 1988. | $ 13.20 | $ 12.00 |
| M11. | W. F. Caspary, "Concepts of Network and Deformation Analysis", 183 pp, 2000. | $ 27.50 | $ 25.00 |
| M12. | F. K. Brunner, "Atmospheric Effects on Geodetic Space Measurements", 110 pp, 1988. | $ 17.60 | $ 16.00 |
| M13. | B. R. Harvey, "Practical Least Squares and Statistics for Surveyors", (2nd edition, reprinted with corrections), 319 pp, 1998. | $ 33.00 | $ 30.00 |
| M14. | E. G. Masters and J. R. Pollard (Eds.), "Land Information Management", 269 pp, 1991. (Proceedings LIM Conference, July 1991). | $ 22.00 | $ 20.00 |
| M15/1 | E. G. Masters and J. R. Pollard (Eds.), "Land Information Management - Geographic Information Systems - Advance Remote Sensing Vol. 1", 295 pp, 1993 (Proceedings of LIM & GIS Conference, July 1993). | $ 33.00 | $ 30.00 |
| M15/2 | E. G. Masters and J. R. Pollard (Eds.), "Land Information Management - Geographic Information Systems - Advance Remote Sensing Vol. 2", 376 pp, 1993 (Proceedings of Advanced Remote Sensing Conference, July 1993). | $ 33.00 | $ 30.00 |
| M16. | A. Stolz, "An Introduction to Geodesy", 2nd extended edition, 148 pp, 2000. | $ 24.20 | $ 22.00 |
| M17. | C. Rizos, "Principles and Practice of GPS Surveying", 565 pp, 1997. | $ 46.20 | $ 42.00 |

## UNISURV REPORTS - S SERIES

(Prices effective October 2001)

| | | | |
|---|---|---|---|
| Australian Prices *: | S8 - S20 | | $11.00 |
| | S29 onwards | Individuals | $27.50 |
| | | Institutions | $33.00 |
| Overseas Prices **: | S8 - S20 | | $10.00 |
| | S29 onwards | Individuals | $25.00 |
| | | Institutions | $30.00 |

* Australian prices include postage by surface mail and GST.
** Overseas prices include delivery by UNSW's air-lifted mail service (~2-4 weeks to Europe and North America). Rates for air mail through Australia Post on application.

S8. A. Stolz, "Three-D Cartesian Co-ordinates of Part of the Australian Geodetic Network by the Use of Local Astronomic Vector Systems", Unisurv Rep. S8, 182 pp, 1972.

S14. E. G. Anderson, "The Effect of Topography on Solutions of Stokes` Problem", Unisurv Rep. S14, 252 pp, 1976.

S16. K. Bretreger, "Earth Tide Effects on Geodetic Observations", Unisurv S16, 173 pp, 1978.

S17. C. Rizos, "The Role of the Gravity Field in Sea Surface Topography Studies", Unisurv S17, 299 pp, 1980.

S18. B. C. Forster, "Some Measures of Urban Residential Quality from LANDSAT Multi-Spectral Data", Unisurv S18, 223 pp, 1981.

S19. R. Coleman, "A Geodetic Basis for Recovering Ocean Dynamic Information from Satellite Altimetry", Unisurv S19, 332 pp, 1981.

S29. G. S. Chisholm, "Integration of GPS into Hydrographic Survey Operations", Unisurv S29, 190 pp, 1987.

S30. G. A. Jeffress, "An Investigation of Doppler Satellite Positioning Multi-Station Software", Unisurv S30, 118 pp, 1987.

S31. J. Soetandi, "A Model for a Cadastral Land Information System for Indonesia", Unisurv S31, 168 pp, 1988.

S33. R. D. Holloway, "The Integration of GPS Heights into the Australian Height Datum", Unisurv S33, 151 pp, 1988.

S34. R. C. Mullin, "Data Update in a Land Information Network", Unisurv S34, 168 pp, 1988.

S35. B. Merminod, "The Use of Kalman Filters in GPS Navigation", Unisurv S35, 203 pp, 1989.

S36. A. R. Marshall, "Network Design and Optimisation in Close Range Photogrammetry", Unisurv S36, 249 pp, 1989.

S37. W. Jaroondhampinij, "A Model of Computerised Parcel-Based Land Information System for the Department of Lands, Thailand", Unisurv S37, 281 pp, 1989.

S38. C. Rizos (Ed.), D. B. Grant, A. Stolz, B. Merminod, C. C. Mazur, "Contributions to GPS Studies", Unisurv S38, 204 pp, 1990.

S39. C. Bosloper, "Multipath and GPS Short Periodic Components of the Time Variation of the Differential Dispersive Delay", Unisurv S39, 214 pp, 1990.

S40. J. M. Nolan, "Development of a Navigational System Utilizing the Global Positioning System in a Real Time, Differential Mode", Unisurv S40, 163 pp, 1990.

S41. R. T. Macleod, "The Resolution of Mean Sea Level Anomalies along the NSW Coastline Using the Global Positioning System", Unisurv S41, 278 pp, 1990.

S42. D. A. Kinlyside, "Densification Surveys in New South Wales - Coping with Distortions", Unisurv S42, 209 pp, 1992.

S43. A. H. W. Kearsley (ed.), Z. Ahmad, B. R. Harvey and A. Kasenda, "Contributions to Geoid Evaluations and GPS Heighting", Unisurv S43, 209 pp, 1993.

S44. P. Tregoning, "GPS Measurements in the Australian and Indonesian Regions (1989-1993)", Unisurv S44, 134 + xiii pp, 1996.

S45. W.-X. Fu, "A Study of GPS and Other Navigation Systems for High Precision Navigation and Attitude Determinations", Unisurv S45, 332 pp, 1996.

S46. P. Morgan et al, "A Zero Order GPS Network for the Australia Region", Unisurv S46, 187 + xii pp, 1996.

S47. Y. Huang, "A Digital Photogrammetry System for Industrial Monitoring", Unisurv S47, 145 + xiv pp, 1997.

S48. K. Mobbs, "Tectonic Interpretation of the Papua New Guinea Region from Repeat Satellite Measurements", Unisurv S48, 256 + xv pp, 1997.

S49. S. Han, "Carrier Phase-Based Long-Range GPS Kinematic Positioning", Unisurv S49, 185 + xi pp, 1997.

S50. M. D. Subari, "Low-cost GPS Systems for Intermediate Surveying and Mapping Accuracy Applications", Unisurv S50, 179 + xiii pp, 1997.

S51. L.-S. Lin, "Real-Time Estimation of Ionospheric Delay Using GPS Measurements", Unisurv S51, 199 + xix pp, 1997.

S53. D. B. Lemon, "The Nature and Management of Positional Relationships within a Local Government Geographic Information System", Unisurv S53, 273 + xvi pp, 1997.

S54. C. Ticehurst, "Development of Models for Monitoring the Urban Environment Using Radar Remote Sensing", Unisurv S54, 282 + xix pp, 1998.

S55. S. S. Boey, "A Model for Establishing the Legal Traceability of GPS Measurements for Cadastral Surveying in Australia", Unisurv S55, 186 + xi pp, 1999.

S56. P. Morgan and M. Pearse, "A First-Order Network for New Zealand", Unisurv S56, 134 + x pp, 1999.

S57. P. N. Tiangco, "A Multi-Parameter Radar Approach to Stand Structure and Forest Biomass Estimation", Unisurv S57, 319 + xxii pp, 2000.

S58. M. A. Syafi'i, "Object–Relational Database Management Systems (ORDBMS) for Managing Marine Spatial Data: ADCP Data Case Study", Unisurv S58, 123 + ix pp, 2000.

S59. X.-Q. Lu, "Strategies for Improving the Determination of Displacements of Sea Surface Temperature Patterns Using Consecutive AVHRR Thermal Images", Unisurv S59, 209 + xiii pp, 2000.

S60. G. Dickson, "GPS-Controlled Photography: The Design, Development and Evaluation of an Operational System Utilising Long-Range Kinematic GPS", Unisurv S60, 417 + x pp, 2000.

S61. J. Wang, "Modelling and Quality Control for Precise GPS and GLONASS Satellite Positioning", Unisurv S61, 171 + x pp, 2001.

S62. Y. Wang, "Knowledge-Based Road Extraction from Aerial Images", Unisurv S62, 178 + xi pp, 2001.

S63. L. Ge, "Development and Testing of Augmentations of Continuously-Operating GPS Networks to Improve their Spatial and Temporal Resolution", Unisurv S63, 230 + xvi pp, 2001.

S64. H.-Y. Chen, "A Study on Real-Time Medium-Range Carrier-Phase-Based GPS Multiple Reference Stations", Unisurv S64, 182 + xxiv pp, 2001.

S65. G. Y. K. Shea, "A Web-Based Approach to the Integration of Diverse Data Sources for GIS", Unisurv S65, 233 + xv pp, 2001.

S66. M. Mirbagheri, "Analysis of Interferometric SAR for Topographic Mapping", Unisurv S66, 135 + xvii pp, 2001.

## Credit Card Orders / Payment

## from / to

## School of Surveying and Spatial Information Systems

## The University of New South Wales

Name and postal address of ordering person/organisation:

_____

_____

_____

_____

_____

Date : _____

Day time phone number : _____

Credit Card debit for:

_____ $ _____

_____ $ _____

_____ $ _____

_____ $ _____

Total $ _____

Please debit my credit card: ☐ Mastercard ☐ Visa ☐ Bankcard

Card Name: _____ Signature: _____

Card No: | | | | | | | | | | | | | | | | |

Expiry Date : _____

Note: UNSW requires that you attach a photocopy of your credit card to this order.